Dissertation for the Ph.D. degree

Fabrication of High Aspect Ratio SU-8 Structures for Integrated Spectrometers

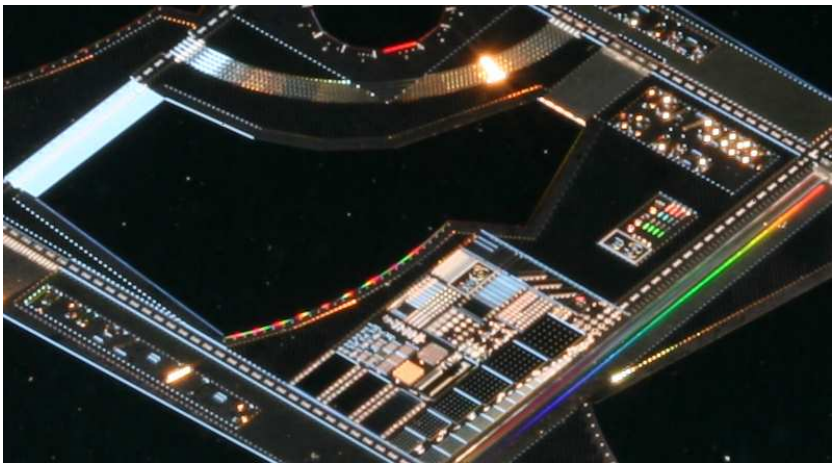

Thomas Aarøe Anhøj, M.Sc.Eng

MIC - Department of Micro and Nanotechnology
Technical University of Denmark
February 2007

Abstract

This dissertation deals with the fabrication of integrated spectrometers for use in miniaturized chemical analysis systems, also called 'lab-on-a-chip'-systems. The spectrometers are based on concave reflection gratings, and are fabricated in the epoxy-based material SU-8 by means of photolithography.

Successful fabrication of reflection gratings requires a high degree of precision in the photolithographic process. The fabrication process has thus been optimized by optimizing the photolithographic process for fabrication of high aspect ratio structures, i.e. structures with details that are small compared to the height of the structure. A decisive factor is the ability of the process to separate closely-spaced structures. The primary measure of quality is thus the aspect ratio of the narrowest trench which it is possible to resolve in the lithographic process.

The optimization of the photolithographic SU-8 fabrication process has caused the aspect ratio of the narrowest resolvable trench to rise from approximately 6 to 11.4. Simultaneously, the optimized process eliminates all problems regarding cracks in the fabricated structures.

If the fabrication of the reflection grating is not perfect, this will primarily be reflected in the spectrometer as an increased transmission loss. The improved precision of the photolithographic process has caused the transmission loss of the fabricated spectrometers to decrease by a factor of six. This means that the spectrometer loss at this point only is two times higher than the predicted loss of a perfectly fabricated spectrometer.

Resumé

Denne afhandling omhandler fabrikation af integrerede spektrometre til brug i miniaturiserede kemiske analyse systemer, populært kaldet 'lab-on-a-chip'-systemer. Spektrometrene er baseret på konkave reflektionsgitre, og fremstilles i det epoxy-baserede materiale SU-8 ved hjælp af fotolitografi.

Succesfuld fabrikation af reflektionsgitre kræver en høj grad af præcision i den fotolitografiske proces. Fremstillingsprocessen er derfor optimeret ved at optimere den fotolitografiske proces til fabrikation af strukturer med højt aspektforhold, det vil sige strukturer hvis detaljer er små i forhold til deres højde. Et afgørende forhold er processens evne til at adskille tætstående strukturer. Det primære kvalitetsmål er derfor aspektforholdet af den mindste rende i materialet, det er muligt at opløse i den litografiske proces.

Optimeringen af den fotolitografiske SU-8 fremstillings proces har afstedkommet at aspektforholdet af den smalleste opløselige rende er steget fra cirka 6 til 11,4. Den optimerede proces fjerner samtidigt samtlige problemer med revner i de fremstillede strukturer.

Hvis fremstillingen af reflektionsgitteret ikke er perfekt, vil det først og fremmest give sig til udtryk ved et forhøjet transmissions tab i spektrometeret. Den forøgede præcision i den fotolitografiske proces har afstedkommet at tabet i de fremstillede spektrometre er blevet seks gange mindre. Herved er spektrometertabet nu kun to gange større end det forventede tab i et perfekt fremstillet spektrometer.

Preface

This dissertation is submitted in partial fulfillment of the ph.d. degree at the Technical University of Denmark, DTU.

The work is entitled "Fabrication of High Aspect Ratio SU-8 Structures for Integrated Spectrometers" and was carried out at MIC - Department of Micro and Nanotechnology at DTU from the 1st of March 2004 to the 28th of February 2007. It forms part of the InSERS (Integrated Surface-Enhanced Raman Spectroscopy) research group at MIC, and is financed by the Danish Agency for Science, Technology and Innovation (former STVF, now FTP). The Ph.D. project was supervised by:

- Associate Professor Jörg Hübner, main supervisor
- Assistant Professor Anders Michael Jørgensen, co-supervisor, presently employed at PhotoSolar, Taastrup, Denmark

both in the InSERS group. With their different style of supervision, Jörg and Anders have both contributed greatly to my work, and to the development of my scientific toolbox. Progress in the InSERS project, however, was a team effort, and it is necessary to acknowledge all of the group. Foremost Assistant Professor Dan Anker Zauner, presently employed at Ignis Photonyx, Birkerød, Demnark, who designed and rendered the integrated spectrometers fabricated in the project. Two Master students, Peter Morten Moselund, and Anders Ebro Christensen, both assisted the progress of the project during their Master Thesis work in the group. The group has provided a pleasant and inspiring working environment, and has contributed greatly to this Ph.D. project.

My time as an employee at MIC has been a great experience, and I would recommend MIC to anyone. The atmosphere at the department is friendly and encouraging, on the scientific as well as the social level. The multidisciplinary nature of the field of research favors cooperation, and I have enjoyed dropping by fellow Ph.D. students or faculty members for a scientific discussion. Socially the whole staff both at MIC and at DANCHIP contribute. Among many others I would like to acknowledge SMK (de Skæggede Mænds Klub), the 2004/2005 executive board of the FridayBar, and the MagSys group who were a surrogate group for me after InSERS HQ became almost empty in August 2006.

I would like to thank Morten Gersborg-Hansen and Christian Danvad Damsgaard for accepting the task as proof-readers on such short notice, and for their constructive input.

My loving and beloved family has been a stable base trough the ups and downs of life as a Ph.D. student. Cecilie, Sarah, and Pia - Thank you!

Contents

1 Introduction **1**
1.1 Integrated Spectrometers . . . 2
1.1.1 The challenges of spectrometer fabrication . . . 4
1.2 SU-8 . . . 6
1.2.1 SU-8 processing in the literature . . . 7
1.2.2 The optical properties of SU-8 . . . 8
1.2.3 SU-8 formulations . . . 9
1.3 Objective . . . 10
1.4 Outline . . . 10

2 SU-8 Processing **13**
2.1 Preparation . . . 13
2.1.1 Substrate pre-treatment . . . 13
2.1.2 SU-8 preparation . . . 16
2.2 Spin Coating . . . 16
2.2.1 Investigation of the spin coating step . . . 17
2.3 Soft Bake . . . 20
2.4 Exposure . . . 20
2.5 Post-Exposure Bake . . . 21
2.6 Development . . . 22
2.6.1 Pre-development relaxation time . . . 23
2.6.2 Development time . . . 25
2.7 Process Monitors . . . 26
2.7.1 Lithographic resolution . . . 26
2.7.2 Structural height . . . 28
2.7.3 Cracking . . . 28
2.7.4 The process monitor chip . . . 29
2.8 Lithographic Performance . . . 29

3 Edge Bead Removal **33**
3.1 Design of Experiments (DOE) . . . 33
3.1.1 Designing experiments . . . 35
3.1.2 Modeling the result . . . 35
3.1.3 Optimizing the process . . . 36
3.2 The Edge Bead Removal Process . . . 36

3.3 The First Design of Experiments 38
3.4 The Result of the First DOE 39
3.5 Optimization 41

4 Parameter Investigation 43
4.1 The Second Design of Experiments 43
4.2 The Result of the Second DOE 46
4.3 Optimization 48
4.3.1 First optimization 48
4.3.2 Second optimization 49
4.3.3 Third optimization 50
4.4 The Models 51
4.4.1 Trench resolution 51
4.4.2 Delamination 53
4.4.3 Cracking 53
4.4.4 The effect of uncontrollable factors in the models . . . 53
4.5 The Optimal Process 54
4.6 Investigation of the Effect of the Soft Bake Temperature . . . 56
4.6.1 Polymerization temperature 58
4.6.2 Lithographic resolution 58
4.6.3 Cracking and hardness 61
4.6.4 Conclusion 63

5 Device Fabrication 65
5.1 SU-8 Processing 65
5.2 Back-end Processing 66
5.2.1 Fluidic vias 67
5.2.2 Bonding 68
5.2.3 Dicing 69
5.2.4 Optical and fluidic interconnections 70
5.3 Turnround and Yield 71

6 Device Performance 73
6.1 The Optical Characterization Set-up 73
6.2 Waveguides 75
6.2.1 The influence of processing conditions 76
6.3 Spectrometers 78
6.3.1 Contributions to the transmission loss 80
6.3.2 Spectrometer performance 83
6.3.3 The effect of the process optimization 83
6.4 Auto-fluorescence in SU-8 84

7 Summary 89
7.1 Conclusion 91
7.2 Outlook 91

A List of Publications **93**
A.1 Peer-reviewed Journal Papers 93
A.2 Conference Proceedings 93
A.3 Patents 94

Bibliography **95**

Chapter 1

Introduction

In 1990, Manz *et al.* proposed the concept of the miniaturized total chemical analysis system, or μTAS [1] (pronounced "micro-tas"). This concept combines the integration of all the steps in a chemical analysis in one single device with the benefits of down-scaling an analytical process. In order to include biological analysis systems, the equivalent term lab-on-a-chip has evolved, probably due to the fact that most of these systems are realized using fabrication methods adapted from the semiconductor industry. The concept has now involved into a world-wide research area, complete with a dedicated journal, appropriately entitled "Lab on a chip". Among the benefits of a μTAS/lab-on-a-chip are reduced analysis time, enhanced analytical performance, and decreased consumption of analyte and reagents [1]. The miniaturization also increases the portability of the system, which enables use in the field, or at the point of care.

The motivation for this Ph.D. project is intimately related to the work in the InSERS group at MIC, DTU. InSERS is an acronym for Integrated Surface-Enhanced Raman Spectroscopy. This small research group was formed in the fall of 2003 with the the aim of realizing Raman spectroscopy on a chip. Raman spectroscopy is a vibrational spectroscopic technique based on the weak inelastic scattering of electromagnetic radiation upon interaction with the vibrations of atomic bonds in molecules. The interaction has a very small scattering cross section, so traditional Raman spectroscopy requires a high intensity of the excitation light, a large interaction volume, and a sensitive detector. In 1974 unusually intense Raman scattering was observed from pyridine adsorbed on a rough silver surface, and the concept of surface-enhanced Raman scattering was soon born. An introduction to the subject is provided by Campion and Kambhampati [2]. Here it will suffice to state that the Raman signal may be enhanced by several orders of magnitude when the analyte is adsorbed on an appropriately structured metal surface. Enhancement factors up to 14 and 16 orders of magnitude have been reported in the literature. Substrates providing six orders of magnitude of enhancement are available commercially in the form of the product Klarite from Mesophotonics [3].

The realization of integrated surface-enhanced Raman spectroscopy, or SERS-on-a-chip, requires the development, and subsequent integration, of several components. The Raman effect must be enhanced at a SERS-active surface, preferably engineered to give a reproducible enhancement factor. In order to unlock the sample specific information contained in the Raman signal, it must be split into its wavelength components. A spectrometer must thus be developed. The sensitivity required to resolve a Raman signal, requires that the Rayleigh scattered excitation light is filtered from the signal. Finally, all the components must be integrated onto a common platform, along with a fluidic system for sample introduction, and optical waveguides for signal detection and introduction of excitation light.

The fabrication platform chosen in the InSERS group is that of structural as well as optical components defined in the photoresist SU-8 on an oxidized silicon substrate using near-UV photolithography. This platform has been used by other researchers at the institute to realize optical detection through integrated waveguides [4], and simultaneous integration of on-chip silicon photodiodes [5]. A glass lid bonded on top of the structures [6] seals the channels in the fluidic system, and protects the optical components. The thickness of the SU-8 layer is set at 40 μm. This thickness is a reasonable choice with regard to the integration of a fluidic system. Waveguides with a 40 μm by 40 μm cross section support a large number of propagation modes, which favors a high throughput, and facilitates the connection between the optical system and the outside world through optical fibers [7].

1.1 Integrated Spectrometers

The integrated spectrometers used in the InSERS project are based on a concave reflective grating. The grating is fabricated in a slab of SU-8 surrounded by air, and mounted so the angle between the grating normal and the input and output positions is 45°. The critical angle for total internal reflection at an interface between SU-8 and air is approximately 39° in the $500 - 1100$ nm wavelength range. Light from the input propagating in the spectrometer slab is thus reflected at the grating. The concave shape of the grating focusses the diffracted light at the output plane. Figure 1.1 shows a sketch of the principle.

In a spectrometer based on a reflection grating, the spectrographic effect is created by the constructive and destructive interference of the light reflected by the grating facets. If light of a wavelength λ is to experience constructive interference at the output, the field reflected by one grating facet must be in phase with the field reflected by the other facets. In other words, the difference in path length at the output between the light reflected by one facet and the light reflected by its neighboring facet must equal an integral multiple of wavelengths. Using the sketch in Figure 1.2, the difference in path length is $(l_1 + \Delta l_1 + l_2 + \Delta l_2) - (l_1 + l_2) = \Delta l_1 + \Delta l_2$. Assuming the spectrometer operates in free space, the phase matching condition can be

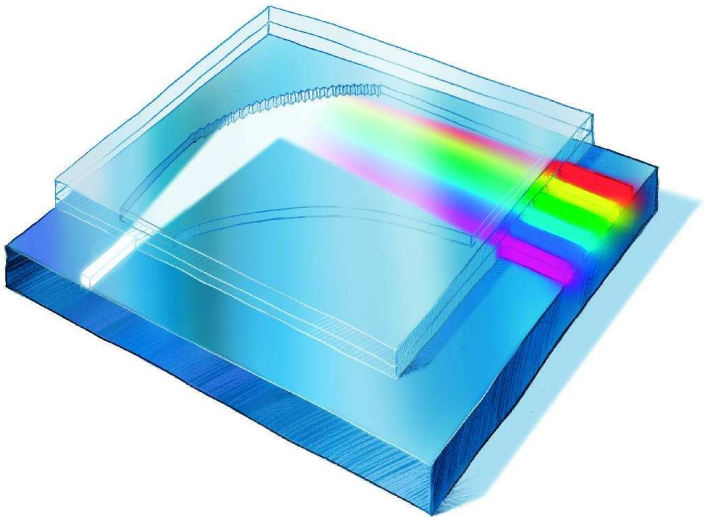

Figure 1.1: The artists impression of an integrated spectrometer based on a concave reflective grating fabricated in a slab of SU-8 sandwiched between an oxidized silicon substrate and a glass lid. Drawing by Claus Rye.

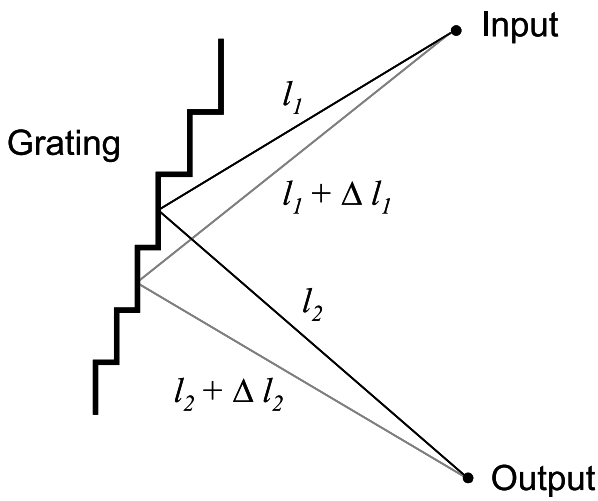

Figure 1.2: A sketch of a reflection grating. The optical path lengths used in the consideration of the phase matching condition given in equation (1.1) are indicated.

expressed as

$$m\lambda = \Delta l_1 + \Delta l_2 \tag{1.1}$$

The integer m is referred to as the order of the diffraction. Equation (1.1) implies that light of a different wavelength may experience constructive interference at the same output when diffracted in a different order. The wavelengths, λ_1 and λ_2, diffracted by two adjacent diffraction orders at the same output are related by

$$m\lambda_1 = (m-1)\lambda_2 \tag{1.2}$$

The difference in wavelength between adjacent orders is called the free spectral range, or FSR. The free spectral range represents the wavelength range in which the spectrometer is capable of distinguishing between the wavelength components in the signal. The free spectral range associated with diffraction order m is defined as

$$FSR_m = \lambda_2 - \lambda_1 \tag{1.3}$$

Equation (1.1) also implies that light of the same wavelength may diffract in several orders and be focussed onto different parts of the output plane. This means that the power in the input signal is distributed among several diffraction orders. Some grating designs use so-called blazing of the grating facets in order to favor diffraction of one wavelength in one order over the other orders and thus increase the transmission through the spectrometer at this wavelength.

The spectrometers were designed and rendered by Dan A. Zauner, using an algorithm employing recursive definition of the grating facet positions [8]. The process uses a diffraction order, a wavelength, a focal length (i.e. the distance from the input/output to the grating pole), and a linear dispersion as design variables. All of these variables influence the size as well as the individual position of the grating facets. The design order m_0 and the design wavelength λ_0 determine the free spectral range, which is given by equations (1.2) and (1.3) as

$$FSR = \frac{\lambda_0}{m_0 - 1} \tag{1.4}$$

The focal length determines the overall size of the spectrometer. The linear dispersion determines how far along the output focal plane an arbitrary wavelength is shifted with respect to the position of the design wavelength. Any given choice of design variables, however, may not result in a successful spectrometer. In particular, a large linear dispersion may render the grating so concave it would disrupt the path of the input light.

1.1.1 The challenges of spectrometer fabrication

Fabrication of the spectrometers using near-UV photolithography affects their performance due to the non-perfect replication of the designed grating. Apart from the free spectral range, which is set by the design parameters, the main characteristics of a spectrometer is the resolving power and

the transmission loss. The resolving power R is a wavelength independent measure of the resolution of the spectrometer, i.e. the ability to distinguish between two peaks in the signal. Resolving power may be defined from the full width at half maximum FWHM and the position λ of a transmission peak as $R = \frac{\lambda}{\text{FWHM}}$. The resolving power also depends on the detector used. Using a 40 μm wide output waveguide, resolving powers around 200 have been measured for the fabricated spectrometers [9]. In measurements where the output focal plane is projected onto a linear CCD array, resolving powers in excess of 400 have been observed, however at a severe loss penalty.

In the recursive grating facet definition procedure used, the size of an individual grating facet increases with increasing order, which favors higher order gratings in terms of the prospect of successful fabrication. A typical design order is thus $m_0 = 9$, which yields a facet width around 8 μm. However, third order spectrometers with 2.7 μm wide facets have been fabricated [9]. The performance of the photolithographic process affects the performance of the spectrometers, mostly by introducing excess transmission loss. Among the lithographic effects that affect the spectrometer performance are:

Line broadening. Limited resolution in the lithographic process causes the size of a structure to differ from the pattern on the mask. This effect displaces the grating from the design position, which causes defocusing of the field at the output plane. This leads to reduced resolving power due to peak broadening, and increases the transmission loss.

Sidewall angle. Diffraction of the exposure light at the edge of the mask pattern may cause the sidewall of a structure to be slanted rather than vertical. Facet non-verticality leads to phase errors in the phase matching condition which results in increased transmission loss.

Corner rounding. Diffraction of the exposure light at the edge of the mask pattern may cause the sharp corners of the grating facets to be rounded. Corner rounding reduces the effective facet area, which would increase the transmission loss, but simulations have shown that this effect is counteracted by the reduction in the shadowing effect between facets [9].

Sidewall roughness. Sidewall roughness reduces the reflectivity of the grating facets, and causes part of the light to be scattered out of the spectrometer. The result is increased transmission loss.

The effect of these loss mechanisms is not only to increase the transmission loss. Scattered light inside the spectrometer slab raises the noise floor, which decreases the signal-to-noise ratio.

Successful fabrication of the designed spectrometers thus requires near-perfect lithographic performance. The main concern in the pattern transfer process is line broadening and sidewall angle. In terms of photoresist properties, this translates to a demand for high contrast. The chosen thickness

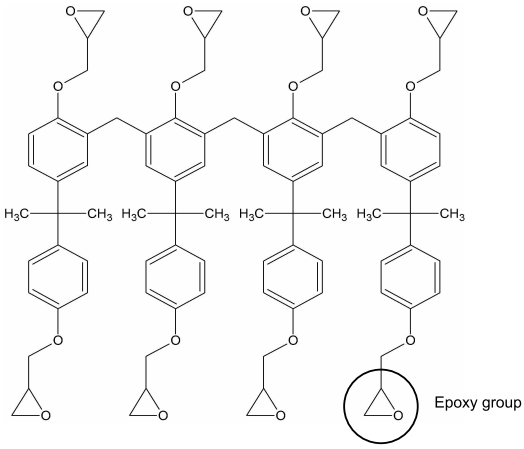

Figure 1.3: A schematic view of the structure of an SU-8 molecule. One of the eight epoxy groups is indicated.

of the resist layer represents a major challenge with respect to obtaining the required lithographic precision, and imposes a demand for high resist sensitivity.

In the case of SU-8, which is a negative tone resist, line broadening and non-zero sidewall angle affect the size of the smallest resolvable trench (or hole). Line broadening fills the gap between the walls on either side of the trench, while a non-zero sidewall angle will close the trench at the substrate. The main focus of the characterization of the lithographic performance is thus the trench resolution (defined as the width of the narrowest, fully resolved trench).

1.2 SU-8

The photoresist SU-8 was developed at IBM in the late 80'ies. It is a chemically amplified, negative tone photoresist, based on the EPON SU-8 epoxy resin [10]. The structure of the SU-8 molecule is sketched in Figure 1.3. The resin is made photosensitive by the addition of a triarylsulfonium salt [10], which acts as a photo-acid generator (PAG). When exposed to UV light, the onium salt decomposes and generates a strong acid [11], which initiates cationic polymerization by ring-opening and subsequent cross-linking of the epoxy groups [12]. The mixture is dissolved in an organic solvent in order to enable deposition by spin coating. The SU-8 molecule has a high functionality, as each SU-8 molecule has eight epoxy groups on average. This yields good sensitivity, while the low molecular weight provides high contrast and solubility [12]. These properties combined with a good UV transparency (46 % transparency at 365 nm for a 100 μm film [13]), makes SU-8 a popular choice for fabrication of high aspect ratio structures.

Typical SU-8 processing consists of resist coating, exposure, curing, and

development [14]. The SU-8 is spin coated onto a substrate and subsequently soft baked in order to evaporate the solvent. In the exposure step the SU-8 film is subjected to near-UV light through a photolithographic mask. Once initiated in the exposure, the polymerization process is assisted by thermal energy in the so-called post-exposure bake, or PEB. Finally the unexposed SU-8 is dissolved by an organic solvent, leaving only the cross-linked SU-8 structures on the substrate.

One of the first applications of the resist suggested was to replace the expensive X-ray lithography step in the LIGA (*Lithographie, Galvanoformung und Abformung*) process with SU-8 and near-UV contact printing lithography [10]. SU-8 is widely used as a structural material in itself, in order to realize microfluidic circuitry [15] or as the molding material for replication in polydimethylsiloxane (PDMS) [16]. Due to its high refractive index (1.60 at 633 nm), SU-8 can serve as the waveguiding material in integrated optics for lab-on-a-chip applications [4, 5]. The ease of patterning and the high aspect ratios obtainable means that advanced integrated optical components such as spectrometers may be realized in SU-8.

1.2.1 SU-8 processing in the literature

High aspect ratio SU-8 structures, such as aspect ratio 10 in 200 μm tall structures, have been reported since the first reports of SU-8 structures [10, 13]. As the coatings became thicker, this figure grew to 20 and above [17, 18]. Recently, aspect ratios of 40 have been reported [19]. Nanometer resolution has been obtained in thin films of SU-8 by employing exposure techniques such as electron-beam lithography [20] and two-photon lithography [21].

Although conceptually a simple process, the realization of SU-8 structures has proven very sensitive to processing conditions. Many have investigated the influence of processing parameters on the performance of SU-8 lithography systematically, with the purpose of process optimization in mind [22, 23, 24, 25, 26]. These investigations all have fixed baking temperature at 95 °C in both soft bake and post-exposure bake, except for one investigation, which shows less delamination at low baking temperature [26]. Two groups have investigated the effect of soft bake time, exposure dose, and post-exposure bake time on the lithographic resolution of $40 - 50$ μm thick SU-8 layers using orthogonal array techniques [22, 24]. The optimal parameter values returned by these optimizations vary greatly, and the two investigations reach opposing conclusions with respect to the most significant parameter. These investigations thus do not give a clear direction in which to go for an optimized process. As a consequence, it was decided to perform a parameter investigation over a broad range *including the baking temperature* in order to optimize the SU-8 process for fabrication of integrated spectrometers.

A significant problem in SU-8 processing is the formation of cracks. The cracks form due to tensile stress in the SU-8, which builds up during process-

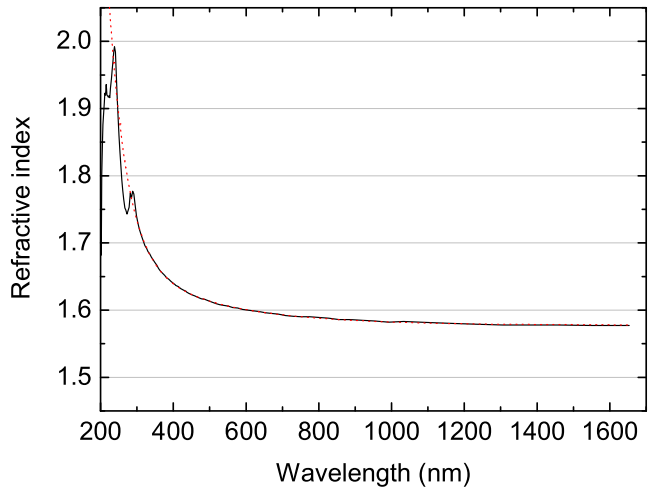

Figure 1.4: The refractive index of SU-8 as a function of wavelength [28]. The dotted line shows the fit according to equation 1.5.

ing, and are initiated during the development. Cracked structures may lead to leakage in microfluidic systems, and unwanted scattering and increased propagation loss in optical systems. Apart from optimization of the processing parameters, cracking problems can be solved through restricted design by reducing the area of exposed SU-8 [27], thus reducing the level of stress in the structures, and by avoiding sharp concave corners, which act as crack nucleation points.

1.2.2 The optical properties of SU-8

In order to design optical components in a material, it is necessary to know the chromatic dispersion of the material. The wavelength dependence of the refractive index of SU-8 is thus an important information in the spectrometer design algorithm. The refractive index of cross-linked SU-8 is presented in Figure 1.4. In the wavelength range of $300-1650$ nm the data are successfully fitted using a double exponential. The fit yields

$$n_{\mathrm{SU-8}}(\lambda) = 0.26 \cdot \exp(\frac{-\lambda}{247.13\ \mathrm{nm}}) + 38.77 \cdot \exp(\frac{-\lambda}{48.80\ \mathrm{nm}}) + 1.578 \quad (1.5)$$

where λ is the wavelength measured in nm. This equation is used in the spectrometer design, as well as in the analysis of the performance of the fabricated spectrometers.

Absorption of light is an important parameter in optical devices. How much a material absorbs will determine which applications it is suited for, and in which wavelength range the performance will be optimal. Figure 1.5 shows the propagation loss of a 100 μm high, 30 μm wide SU-8 waveguide

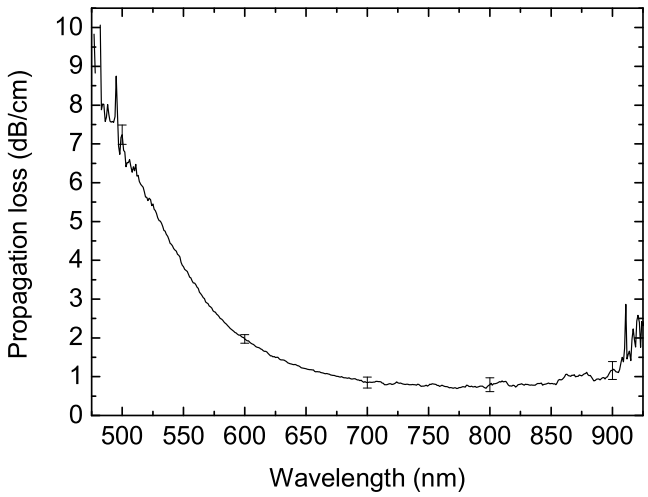

Figure 1.5: Propagation loss of a 100 μm high, 30 μm wide SU-8 waveguide with PDMS top cladding. The data are curtesy of Klaus Bo Mogensen [4].

with PDMS top cladding [4]. The propagation loss is observed to be below 1.5 dB/cm at red and near-infra red wavelengths. In this wavelength range SU-8 is a suitable material for integrated optics, but not a suitable material for e.g. fibers intended for long-haul transportation of optical signals.

Another important issue is that of auto-fluorescence. SU-8 has been reported to fluoresce when exposed to light of wavelengths used to excite fluorescent markers [29, 30, 31], but the auto-fluorescent response has not been characterized in much detail. The result of an investigation of SU-8 auto-fluorescence is presented in chapter 6.

1.2.3 SU-8 formulations

SU-8 is available in two series from the manufacturer MicroChem Corporation. The original series is formulated using γ-butyrolactone as the solvent. A new series, the 2000-series, was developed in order to reduce processing time, and improve the wettability and adhesion between substrate and resist [32]. The 2000-series is formulated using cyclopentanone as the solvent. Both series come in a variation of solid content, in order to enable spin coating of different film thicknesses. The formulations have names such as SU-8 5 for film thicknesses around 5 μm, and SU-8 2100 for film thicknesses around 100 μm. The first attempts at SU-8 processing in the InSERS group in the fall of 2003 used SU-8 2035. These attempts had problems in the coating procedure, and the lithographic resolution was discouraging. When the SU-8 was substituted for the original series, the performance improved. It has later been confirmed by the manufacturer that while the 2000-series provides better adhesion, the original series is superior in terms of resolution. Due to

concerns about material homogeneity, the SU-8 25 formulation was chosen as this formulation has a filtration level of 2.5 μm (compared to 4.5 μm for SU-8 2035).

1.3 Objective

Joining the InSERS group as a Ph.D. student in the spring of 2004, I was presented with the task of developing the fabrication platform in order to make fabrication of the designed spectrometers possible. As mentioned earlier, the fabrication platform is that of SU-8 on an oxidized silicon substrate. Apart from the material itself, the thickness of the SU-8 layer, and the specific SU-8 formulation, had been defined prior to the start of this Ph.D. project.

The main objective of this Ph.D. project is to optimize the performance of the SU-8 photolithographic process to a point where the designed spectrometers can be successfully fabricated. In order to define an optimized fabrication process, a series of goals were established in the summer of 2004:

- Inter-structural resolution down to 4 μm.
- Stable structures with aspect ratios exceeding 7.
- Reproducible, uniform SU-8 layer thickness. Standard deviation of the layer thickness in the quality area below 0.7 %. Edge bead below 10 % of the thickness, if possible down to 2 %.
- A yield of 95 % (including packaging and dicing).
- Spectrometer loss in the $785 - 885$ nm band of no more than 15 dB, preferably lower, with a channel-to-channel variation below 1 dB.
- Crosstalk suppression at $\Delta\lambda = 10$ nm in the $785 - 885$ nm band of at least 20 dB.

The first goals relate to the performance of the fabrication process, and reflect the groups perception of the performance needed to realize the integrated spectrometers. The two last goals, on the other hand, relate directly to the performance of the fabricated spectrometers, and may impose further constraints on the lithographic performance as well as on the spectrometer design.

1.4 Outline

The structure of this Ph.D. dissertation falls in two parts; processing and performance. The first part consists of chapters 2 through 5, and cover the development and optimization of the SU-8 photolithographic process, as well as the packaging of the fabricated structures. Chapter 2 should provide a thorough introduction to the aspects of SU-8 lithography, and would be

a good start for someone considering to use SU-8 for the first time. The parameter investigation presented in chapter 4 is probably mostly of interest to the experienced user. The chapter introductions include the main results of the presented subject. This should enable the reader to identify the chapters of interest.

The main focus of this Ph.D. project has been the optimization of SU-8 process, but the efforts are of no use if the increased lithographic precision does not translate into improved performance of the fabricated spectrometers. Chapter 6 presents the performance of the fabricated spectrometers, with the emphasis on the effect of the optimization on spectrometer transmission.

Chapter 7 summarizes the results of the dissertation, and evaluates the success of the process optimization on the basis of the goals defined in section 1.3.

Chapter 2

SU-8 Processing

Conceptually the fabrication of SU-8 structures is a simple photolithographic process. The actual realization of the process, however, requires the engineer to choose from a series of options, and to adjust a multitude of parameters accordingly. Figure 2.1 presents a flow chart of the SU-8 process based on the process recommendations provided by the manufacturer [14] along with sketches of the wafer at each step. The flow chart has been adapted to represent the laboratory procedure that had been established in the InSERS group during the first half year of this project. The following sections describe each step in detail, presenting the considerations behind the choice of procedures and parameter values, along with investigations of the influence of individual parameters where such have been conducted.

The process described in this chapter is capable of realizing open trenches with an aspect ratio of 6. Such a resolution is not sufficient to realize integrated spectrometers of the desired quality, and prompted the developments and optimizations presented in the subsequent chapters. The effect of the limited resolution on the fabrication of the spectrometer grating is seen in Figure 2.2. More details on the lithographic performance of the process are presented in section 2.8.

2.1 Preparation

Before the lithographic process can begin, certain preparations must be carried out. Foremost, the substrate must be clean and dry. Since the SU-8 is intended to be used as the waveguiding material in the devices, an optical buffer must be created between the SU-8 and the silicon which is used as the substrate. The resist itself must also be made ready to dispense before spin coating can be performed.

2.1.1 Substrate pre-treatment

Silicon wafers provide a cost effective, atomically flat substrate, which is directly compatible with all of the microfabrication tools available in a clean-

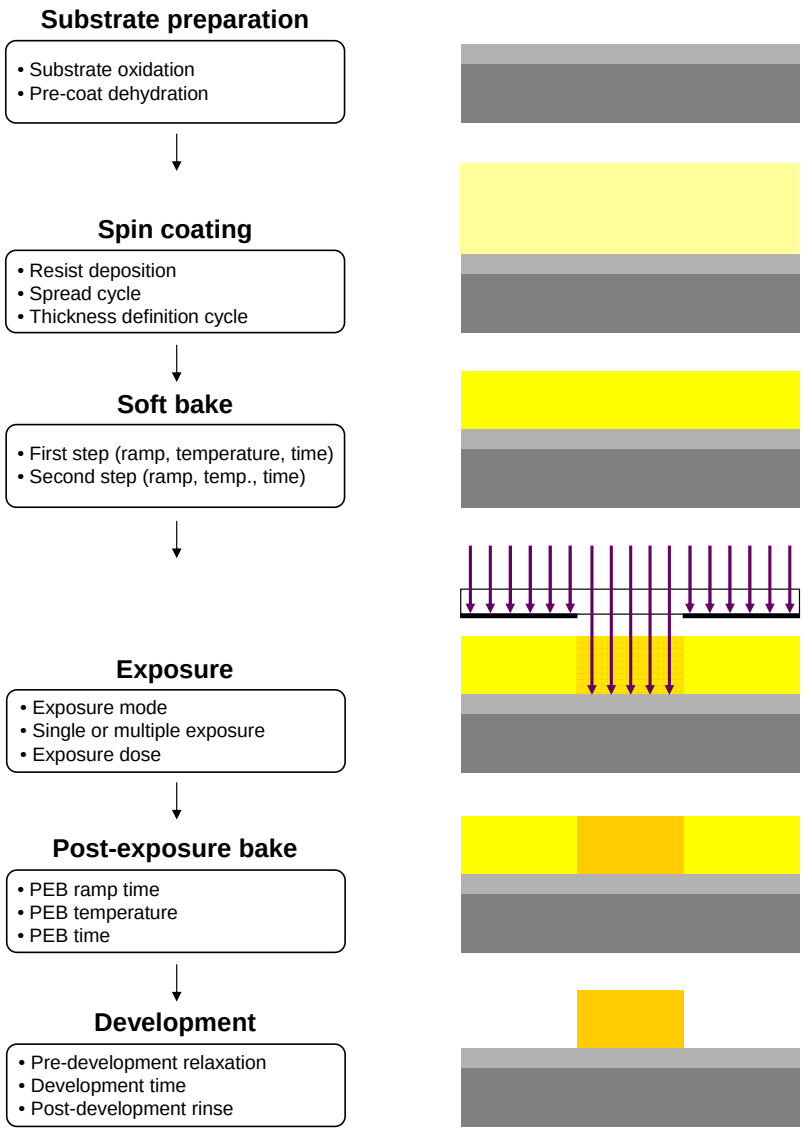

Figure 2.1: Process flow chart illustrating the different steps and parameters involved in the processing of SU-8. Cross-sectional views of the wafer are sketched at each step. The sketches are not to scale.

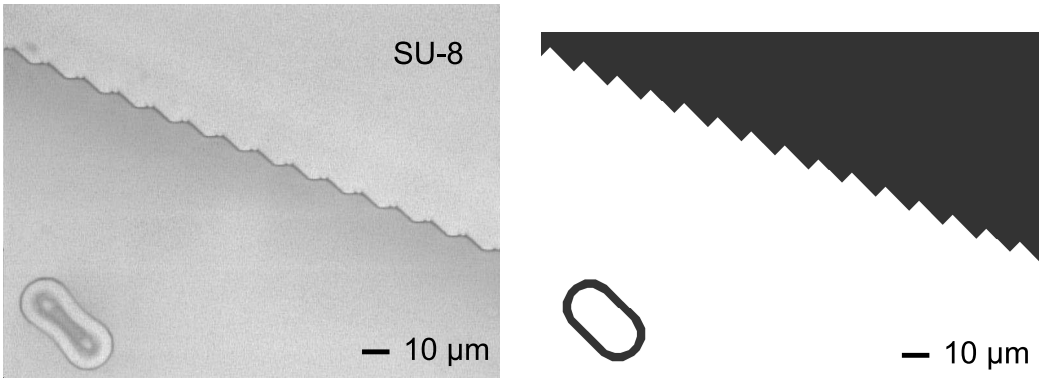

Figure 2.2: Optical micrograph of a 12th order grating fabricated using standard SU-8 processing. For comparison, the mask layout is replicated to the right. The grating facets are 10.8 μm wide and offset by 4.5 μm. The grating is seen to be affected by both line broadening and corner rounding.

room. In order to be able to coat a substrate with a uniform, continuous layer of resist, the substrate must be dry and free from particles. Particles present on the surface at spin coating disturb the process and tend to open holes in the resist coating. Water adsorbed on the substrate surface weakens the bond between resist and substrate, increasing the risk of delaminating structures. Thus, the silicon wafers must be cleaned and dehydrated before use.

The SU-8 is used primarily as a waveguiding material in the finished devices. In order to enable waveguiding, a barrier of low refractive index material must be placed between the SU-8 (1.60 at 633 nm) and the silicon (3.88 at 633 nm). Since the refractive index of SiO_2 (1.46 at 633 nm) is lower than both, this optical buffer is conveniently created through oxidation of the silicon substrate.

The substrates are oxidized in a steam environment at 1150 °C for 16 hours. This creates an approximately 2.7 μm thick SiO_2 layer on the entire wafer. At the end of the oxidation process the temperature is 700 °C, and the substrates are thus completely dry when they exit the oven. In the period between oxidation and spin coating, the substrates must be prevented from adsorbing water from the ambient. Initially, the wafers were stored in a nitrogen flow box, and transported to a convection oven for dehydration at 250 °C for a period of 10 to 18 hours prior to coating. An increase in coating problems was observed with increased storage time. This seemed to be due to particle contamination, possibly from a worn door seal on the flow box. As a consequence, the procedure was changed, and all of the wafers were stored in the convection oven at 250 °C between oxidation and coating. No coating problems have been observed with this procedure.

2.1.2 SU-8 preparation

The SU-8 used throughout this project is the NANO SU-8 25 formulation from MicroChem Corporation. Undiluted SU-8 is a solid, glassy material at room temperature, so the resist must be dissolved in a solvent in order to enable spin coating. The SU-8 25 formulation is 63 weight percent SU-8 resist dissolved in γ-butyrolactone (GBL). The resist is refrigerated between use in order to prolong shelf-life. In the spin coating process the resist is dispensed manually onto the substrate, so it must be prepared in advance. The resist container is removed from the refrigerator, and is allowed to acclimatize before the resist is poured into a 30 mL dispenser syringe. In order to prevent the SU-8 from absorbing moisture from the air, it is vital that the resist is allowed to warm up to room temperature before the container is opened. A one liter bottle will reach 22 °C from 5 °C in approximately one and a half hour.

Once filled, the dispenser syringe is left in an upright position to allow for bubbles to gather at the top of the syringe. Due to the relatively high viscosity of the resist bubbles rise slowly, and thus the syringe is filled the day before spin coating is scheduled, and allowed to settle over night.

2.2 Spin Coating

The flow chart in Figure 2.1 shows the three steps of the spin coating process: resist deposition, spread spin cycle, and thickness definition spin cycle. The substrate is transported directly from the dehydration oven to a robotic handler, which loads it onto the vacuum chuck of the spin coater. A volume of approximately 5 mL of resist is deposited manually in the center of the wafer using the dispenser syringe. In the spread cycle, the wafer is ramped slowly, at 100 rpm/s, to 500 rpm where it spins for 5 seconds, allowing for the deposited resist to cover the entire wafer. Subsequently, the thickness definition cycle ramps the wafer at 300 rpm/s to the thickness definition speed, where it is held for the duration of the thickness definition time. A thickness definition speed of 1250 rpm and a thickness definition time of 30 s produces an approximately 41 μm thick coating of SU-8 25 (after soft bake). Both spin cycles are performed in a closed spin, using a so-called gyrset. The gyrset is a chuck and lid configuration developed by Karl Süss for their spin coaters. The lid covers the wafer and rotates with the chuck, providing a more solvent rich and less turbulent spinning environment than a closed spin without the gyrset. Using the gyrset allegedly increases the coating homogeneity.

Figure 2.3 shows a profile scan across the surface of a soft baked SU-8 coating. The most pronounced feature is the protrusion at each edge, which protrudes approximately 30 μm above the surface of the central coating. This phenomenon is called an edge bead, and is a consequence of the spin coating process. The edge bead is seen to affect the coating more than 10 mm from the edge. Surface scans of three wafers with equal coating

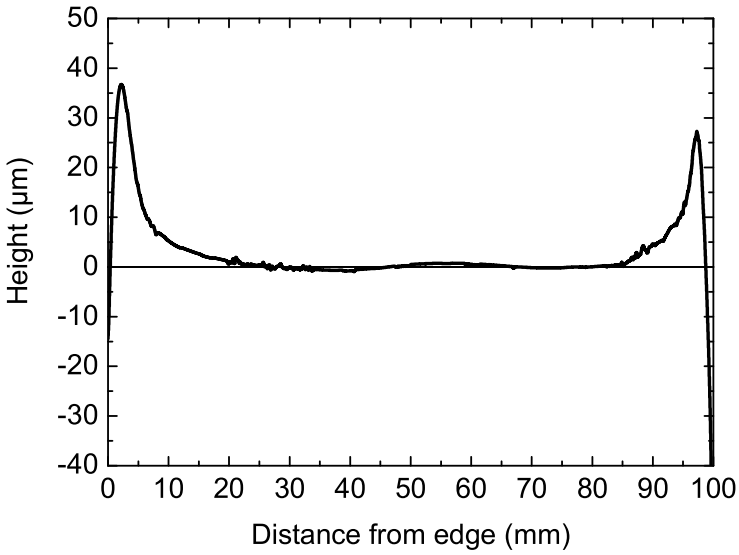

Figure 2.3: Profilometer line scan of the surface of a 41 μm thick SU-8 25 coating. The scan has been corrected for wafer bow. The height of the edge bead is seen to be on the order of 30 μm.

parameters showed an average edge bead height of 26 μm. The presence of an edge bead introduces a gap between the central part of the wafer and the photolithographic mask in the exposure procedure. This gap leads to proximity effect in the exposure, which causes the lithographic resolution to deteriorate (see section 2.4). The presence of the edge bead is the single most important limitation on the lithographic precision.

The edge bead problem may be solved using one of two different approaches. In some cases it is possible to minimize the height of the edge bead through clever design of the spin coating process, in others the edge bead must be removed in a separate step following the spin coat. The latter involves application of a solvent to the edge of the wafer, and this is generally a more cumbersome and less reliable process. The first attempts to deal with the problem thus focussed on the the spin coating step. Additional spin cycles after the thickness definition cycle (consisting of series of short low and high speed spins) did not yield reproducible results. A thorough investigation of the effect of the thickness definition parameters (presented below) showed the edge bead height to be correlated to the coating thickness, and did not provide a simple solution to the problem.

2.2.1 Investigation of the spin coating step

In an attempt to solve the edge bead problem, three series of five wafers were coated, and characterized in order to determine the edge bead height

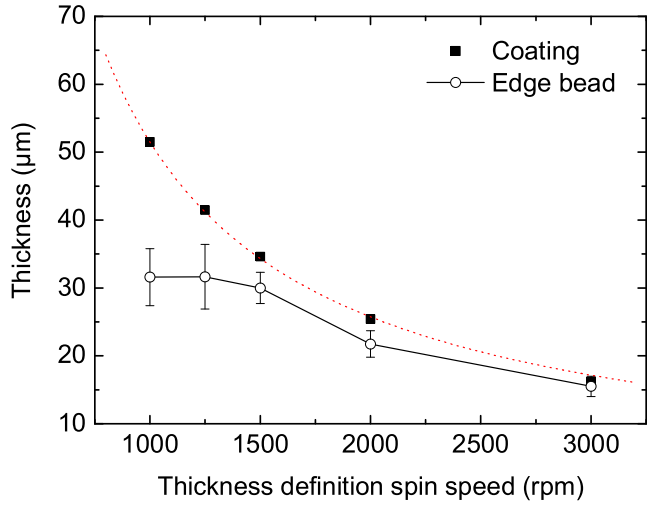

Figure 2.4: Coating thickness and edge bead height as a function of the thickness definition speed for spin coating of SU-8 25. The ramping rate is 300 rpm/s, and the thickness definition time is 30 s. The error bars on the edge bead height correspond to the range of the measured edge bead heights. The dotted line shows a fit of the coating thickness according to equation (2.1).

and the coating thickness. The three series have the spin process described above as starting point, and each varies one of the three variables in the thickness definition step: the ramping rate, the rotational speed, and the spinning time. The ramping rate was varied in five steps between 100 rpm/s and 5000 rpm/s, but the result showed no effect on the edge bead. The thickness definition speed was varied between 1000 rpm and 3000 rpm, while the thickness definition time was varied between 10 s and 120 s.

The result of the investigation of the thickness definition speed is presented in Figure 2.4. The coating thickness is seen to decrease monotonically with increasing spin speed. The edge bead height is initially constant at approximately 30 μm. As the coating thickness decreases, however, so does the edge bead height. The edge bead height seems to be fixed at a value slightly below the coating thickness, however with a maximum value of 36 μm.

Figure 2.5 shows coating thickness and edge bead height as a function of thickness definition time. The coating thickness is seen to decrease monotonically with increasing spin time. As in the case of the thickness definition speed, the edge bead height observed to be slightly lower than the coating thickness, with a maximum height of 36 μm.

The coating thickness data may be fitted in order to provide a spin curve for future reference. Empirically the coating thickness as a function of the

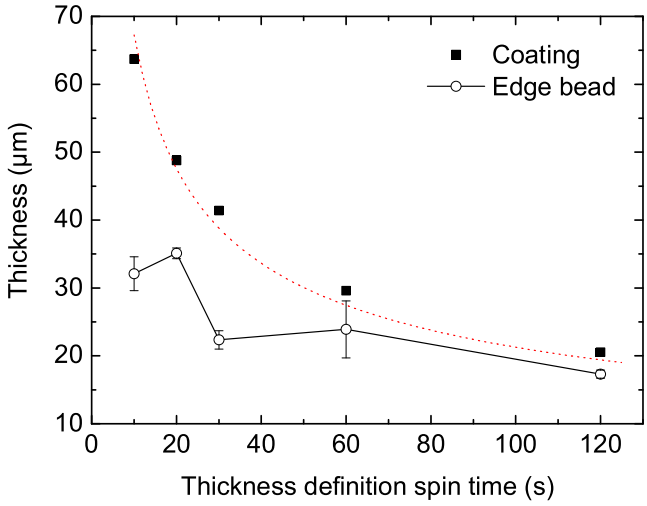

Figure 2.5: Coating thickness and edge bead height as a function of the thickness definition time for spin coating of SU-8 25. The ramping rate is 300 rpm/s, and the thickness definition speed is 1250 rpm. The error bars on the edge bead height correspond to the range of the measured edge bead heights. The dotted line shows a fit of the coating thickness according to equation (2.2).

spin speed can be expressed as [33]

$$t(\omega) = k_1 \frac{1}{\omega^\alpha} = (51500\ \mu\text{m} \cdot \text{rpm}) \frac{1}{\omega} \tag{2.1}$$

where ω is the spin speed in rpm. The constant k_1 depends on the specific spin coater used, the concentration and kinematic viscosity of the resist, and the amount of resist deposited, as well as the ramping rate and the spin time. Fitting the coating thickness data presented in Figure 2.4 according to equation 2.1 yields a very good fit. The exponent α is 1 within the error of the fit, i.e. the coating thickness is inversely proportional to the spin speed. For the constant of proportionality, the fit yields $k_1 = 51500 \pm 350\ \mu\text{m} \cdot \text{rpm}$. The coating thickness as a function of the spin time is expressed as [33]

$$t(t_{\text{spin}}) = k_2 \frac{1}{{t_{\text{spin}}}^\beta} = (213\ \mu\text{m}\sqrt{\text{s}}) \frac{1}{\sqrt{t_{\text{spin}}}} \tag{2.2}$$

where t_{spin} is the spin time in seconds. Again, the constant k_2 depends on the specific spin coater used, the concentration and kinematic viscosity of the resist, and the amount of resist deposited, as well as the ramping rate and the spin speed. Fitting the coating thickness data of the spin time investigation reveals that the coating thickness is inversely proportional to the square root of the spin time. The constant of proportionality is $213 \pm 6\ \mu\text{m}\sqrt{\text{s}}$.

2.3 Soft Bake

When the substrate has been coated in the spin coating step, the wet resist must be baked in order to evaporate the solvent. The wafer is baked on a contact hotplate in two steps, first at 65 °C, then at 95 °C. The two-step procedure is adopted from the process recommendations [14], but the hotplate is ramped between the steps, rather than moving the wafer from one pre-heated hotplate to another, in order to minimize the effects of thermal shocking. In the first step, the hotplate is ramped from room temperature to 65 °C in three minutes and baked for ten minutes. The second step ramps the temperature to 95 °C and bakes the wafer for 30 minutes. Finally, the heating is switched off, and the wafer is allowed to cool down with the hotplate. The characteristic time constant of this exponential decay was measured to be approximately 37 minutes for the hotplates used. It takes around one and a half hours for the hotplate to cool to below 30 °C, at which point the soft bake is considered concluded. Up to five wafers are baked simultaneously on the same hotplate.

2.4 Exposure

The soft bake completes the resist coating process, and makes the substrate ready for the first step in the actual pattern transfer process. In the exposure step, the resist is exposed to near-UV light, which initiates the cross-linking process. The resist is patterned by exposure through a mask which has the desired pattern etched through an opaque material. Such a mask is usually made in the form of a thin chrome layer on a glass substrate. Since SU-8 is a negative tone resist, the areas where the resist is to be left on the wafer must be open on the mask. The wafer is exposed in the so-called hard contact mode, where the wafer is pressed into contact with the mask. The wafer is then exposed to light with a wavelength of 365 nm using the i-line from a mercury lamp. The mask aligner used in the exposure step has been fitted with an i-line filter (365 nm, 20 nm FWHM) as the increased SU-8 absorption at shorter wavelengths would otherwise jeopardize the resolution [10], [13].

According to the manufacturer, a 40 μm thick film of SU-8 requires an exposure dose of $200 - 330$ mJ/cm^2 [14]. Initially, the dose was administered in a series of small doses with a relaxation time of $10 - 20$ s in between exposures. This multiple exposure strategy was used in order to limit photo-acid diffusion induced by heating of the resist due to absorption of the exposure light. However, as the optimal dose was observed to be in the low end of the range, practice was changed to single exposure. The dose is thus administered in a single exposure, usually $20 - 30$ s at 9.0 mW/cm^2, corresponding to a dose of $180 - 270$ mJ/cm^2.

In contact printing the resist is, by definition, in perfect contact with the mask. This may however not be true in real life printing. The presence of an edge bead prevents contact between the central part of the wafer and the

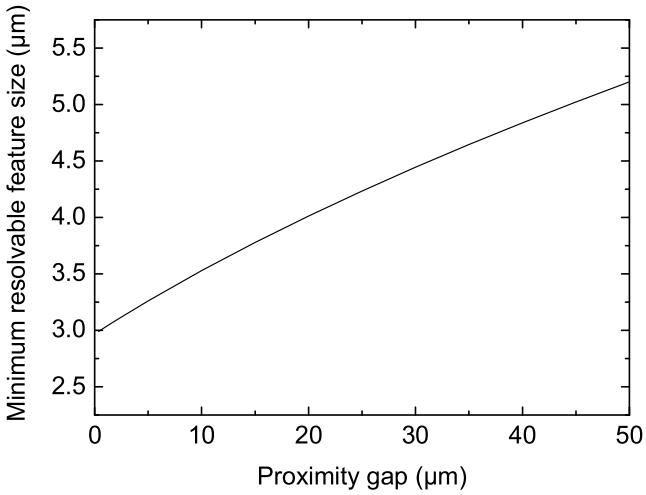

Figure 2.6: Minimum resolvable feature size as a function of the proximity gap (i.e. the size of the gap between mask and resist) as predicted by equation (2.3) for a 40 μm thick layer of SU-8 exposed at 365 nm. The minimum resolvable feature size increases from 3 μm at contact printing to 4.3 μm when the edge bead introduces a gap of 26 μm.

mask. The minimum resolvable feature size w_{min} can be expressed as [34]

$$w_{min} = c\sqrt{(g + \frac{t}{n})\lambda} \tag{2.3}$$

where g is the size of the gap between mask and resist, t and n is the thickness and the refractive index of the resist, respectively, and λ is the wavelength of the exposure light. The constant c is usually assumed to be unity. The minimum feature size is seen to increase with increasing gap size. In the case of 40 μm thick SU-8, the presence of the edge bead (see Figure 2.3) increases the minimum resolvable trench width from an optimal value of 3 μm at $g = 0$ to 4.3 μm at an edge bead height of 26 μm. This corresponds to a decrease in the obtainable trench aspect ratio from 13.4 to 9.4.

2.5 Post-Exposure Bake

Once the cross-linking process has been initiated by the exposure, it is assisted by thermal energy in the post-exposure bake (PEB). As in the soft bake, the wafer is baked on a contact hotplate, but in the post-exposure bake a long ramp is chosen in favor of the two-step process. The hotplate is ramped from room temperature to 95 °C in 6 minutes and baked for 4 minutes. The heating is switched off, and the hotplate is allowed to cool to below 30 °C.

In order to limit photo-acid diffusion, the post-exposure bake is initiated shortly after exposure. As several substrates are exposed in the exposure step, this usually means within 15 to 30 minutes. The choice of post-exposure bake time is a trade-off between a long bake in order to allow for the cross-linking process to proceed as far as possible, and a short bake in order to minimize line broadening due to cross-linking continuing outside the exposed area.

2.6 Development

The pattern transfer from mask to SU-8 structures is finished in the development step. The areas which were irradiated in the exposure have cross-linked in the post-exposure bake. Now, the non-cross-linked areas must be dissolved in an organic solvent similar to the one used to dilute the resist for spin coating. The developer supplied by the manufacturer is propylene glycol monomethyl ether acetate (PGMEA). First, the substrate is submerged in a bath of agitated PGMEA. Within 2-3 minutes, large areas of unexposed SU-8 are observed to be removed. After five minutes, the substrate is transferred to a second, cleaner bath, and further developed for five minutes. Finally, the developed wafer is rinsed with fresh 2-propanol (IPA) from a wash bottle, and dried.

The first developer bath, the coarse developer, is designed to remove the bulk of the unexposed SU-8. This bath usually has a relatively high content of SU-8. The second bath, the fine developer, is cleaner, and thus more aggressive. It is designed to develop fine structures, such as narrow trenches, a process which might be limited by the transport of dissolved SU-8. The post-development rinse serves a double purpose. Primarily, it replaces the slow drying PGMEA with fast drying IPA, reducing the drying time from several hours to 15 minutes. However, the properties of the rinse solvent also affects the structures on the wafer. In a study by Tanaka *et al.*, resist pattern collapse is attributed to forces exerted on the patterns by the surface tension of the evaporating solvent after development [35]. Their conclusion is to use a low surface tension rinse solvent, or a rinse solvent with a contact angle of approximately 90°. The contact angles between SU-8 and the two solvents in the development were measured to be $2.6 \pm 0.9°$ and $5.4 \pm 0.9°$ for PGMEA and IPA, respectively, on a contact angle meter. With such low and comparable contact angels, the lower surface tension of IPA (20.9 mN/m compared to 27.5 mN/m for PGMEA) reduces collapse of high aspect ratio structures.

The formation of cracks in the fabricated structures is a recurrent problem in SU-8 processing. The cracks form due to tensile stress in the SU-8, which builds up during processing, and are observed to be initiated during the development. Some SU-8 users recommend a period of relaxation between post-exposure bake and development in order to release the residual stress (e.g. [16]). The effects of pre-development relaxation and development

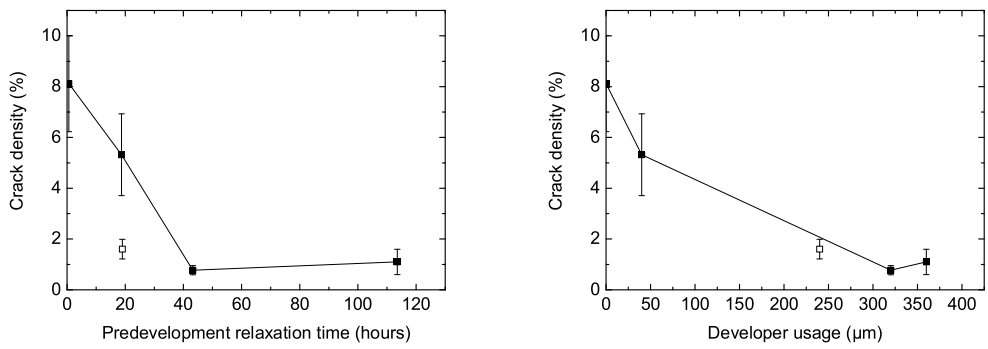

Figure 2.7: Crack density plotted as a function of pre-development relaxation time and developer usage, respectively. The development time is fixed at 10 minutes. Developer usage is measured as the accumulated thickness developed in the bath (regardless of active area). The 10 minute sample from the development time investigation has been included in the graphs for comparison (open symbols). The crack density is calculated by image analysis of monitor structures such as the one showed in Figure 2.10. The error bars represent the range of measurements.

time were investigated in two series of four wafers each. The details of the investigations are presented in the sections below.

The investigation of the development process proved that pre-development relaxation results in line broadening. Development should thus be performed immediately after conclusion of the post-exposure bake. It cannot be ruled out that pre-development relaxation affects the cracking of SU-8, but the effect is on a shorter time scale than the one studied here. The longer the SU-8 is subjected to the developer, the more cracks are initiated. A fresh developer will also initiate more cracks, but the effect wears off fast. A total development time of five minutes for a 40 μm thick film ensures the development is not a limiting factor on the lithographic resolution, while cracking is kept at a minimum. The results of the investigation reassured the need for logging of pre-development relaxation time and developer usage in further investigations.

The two investigations of the development process were conducted at a point where an edge bead removal process had already been established. This was a deliberate choice, as the increased resolution at this point would allow small effects to be seen more clearly. The details of the inspection methods used to characterize the lithographic performance of the processing are presented in section 2.7.

2.6.1 Pre-development relaxation time

The first wafer in the investigation of the pre-development relaxation time was transferred from the hotplate to the developer immediately after the post-exposure bake was concluded. The second was allowed to relax until

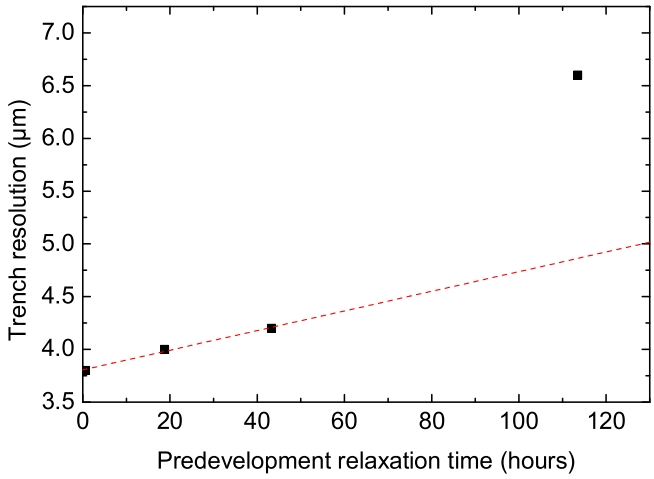

Figure 2.8: The width of the narrowest, fully resolved trench as a function of pre-development relaxation time at a fixed development time of 10 minutes. The trench resolution is determined by optical microscope inspection of monitor structures. The point at 114 hours is considered an outlier. The dashed line represents a fit to the first three data points.

the next day, the third yet another day, and the last wafer was allowed to relax for 5 days prior to development. The wafers were stored at 22 °C shielded from exposure to UV light. All four wafers were developed for a total of ten minutes. The inspection of the crack density shows a substantial decrease with increasing relaxation time. However, the crack density of the sample relaxed overnight does not agree with the corresponding sample from the development time investigation. While the sample relaxed over night has a crack density of 5.3 %, the 10 minute sample from the development time investigation, which was also relaxed overnight, has 1.6 % cracks. It was realized that the developer bath had been changed to fresh PGMEA just before the development of the first wafer in the series. Suspecting the condition of the developer to influence the initiation of cracks, the crack density was plotted as a function of the total thickness of SU-8 developed in the bath prior to each sample (the values were recovered from process notes and the equipment log). Figure 2.7 shows the crack density plotted as a function of pre-development time and developer usage, respectively. From these observations, it is concluded that the crack density is not decreased by relaxation times in excess of 19 hours. The developer usage plot confirms the suspicion of developer condition dependent cracking. However, the effect is seen to wear off after the first five or six wafers have been developed in a new developer bath.

Figure 2.8 shows a steady increase in the width of the narrowest, fully resolved trench with increasing relaxation time. From a value of 3.8 μm at

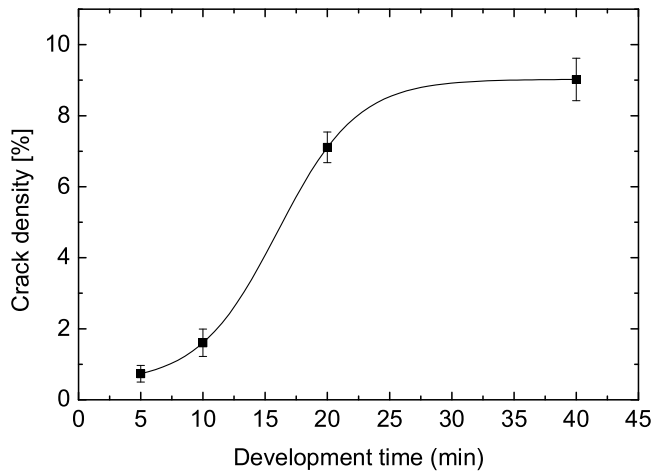

Figure 2.9: Crack density as a function of development time at a fixed pre-development relaxation time of 19 hours. The line is a guide to the eye. The crack density is calculated by image analysis of monitor structures such as the ones showed in Figure 2.10. The error bars represent the range of measurements.

immediate development, it deteriorates to 4.2 μm after 43 hours of relaxation. After 5 days of relaxation, the trench resolution is 6.6 μm wide. This value seems exaggerated compared to the trend shown in the first three points, and is considered an outlier. An estimate based on the first three points in the investigation, suggests the interface between cross-linked and non-cross-linked SU-8 moves into the non-cross-linked region at an approximate rate of 5 nm per hour.

2.6.2 Development time

The four wafers in the investigation of the development time were allowed to relax overnight and developed with total development times ranging from 5 to 40 minutes. The first wafer was developed three minutes in the coarse developer bath and two minutes in the fine, while the rest of the wafers were developed in the coarse developer for five minutes and the remainder of the development time in the fine developer bath. Inspection of the developed wafers showed no effect of the development time on the trench resolution. All four wafers had a trench resolution of 4.2 μm. However, the development time does have an effect. Figure 2.9 shows the crack density as a function of development time. The crack density is seen to increase with increasing development time. This phenomenon is caused by stress dependent polymer-solvent interaction, leading to cracks being initiated at points of increased stress. The longer time the structure is subjected to the solvent, the more cracks are initiated. The effect wears off as the stress is released by the cracks, but for excessive development the cracks grow in size as well as in

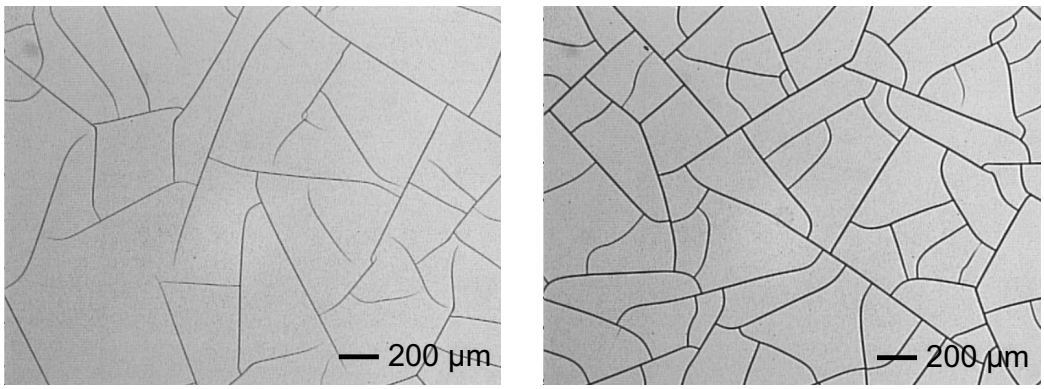

Figure 2.10: Optical micrographs of the crack density monitor structure of samples developed for 20 minutes and 40 minutes, respectively. The cracks are seen to grow in size as well as in numbers with increased development time. The left hand picture corresponds to a crack density of 6.7 %, while the right hand picture corresponds to a crack density of 9.6 %. For details on the crack density, see section 2.7.3.

numbers due to the attack of the solvent. This effect is shown in Figure 2.10.

2.7 Process Monitors

In order to be able to compare different process runs, a significant effort was made to establish inspection methods of the most important processing results. When the wafers have been developed, the performance of the lithographic process is assessed through inspection of various monitor structures. These structures are inspected in order to determine the lithographic resolution, the structural height, and the degree of cracking.

The monitor structures described in the following are included on a lithographic mask designed specifically for process development and optimization. The layout of the test mask can be seen in Figure 2.11. The design includes many more structures than the ones used for process optimization in this project. Most of the monitor structures are repeated at different positions on the mask. The position of the structures used for process characterization are indicated in Figure 2.11.

2.7.1 Lithographic resolution

The lithographic resolution is determined by inspection of two monitor structures using an optical microscope. The trench resolution monitor, which is shown in Figure 2.12 a), consists of three trenches 50 μm apart with a width which is varied in 0.2 μm steps. The ridge resolution monitor, see Figure 2.12 b), is a series of seven ridges anchored at one end. The ridges are separated by a space equal to the width, and the width is varied in steps of

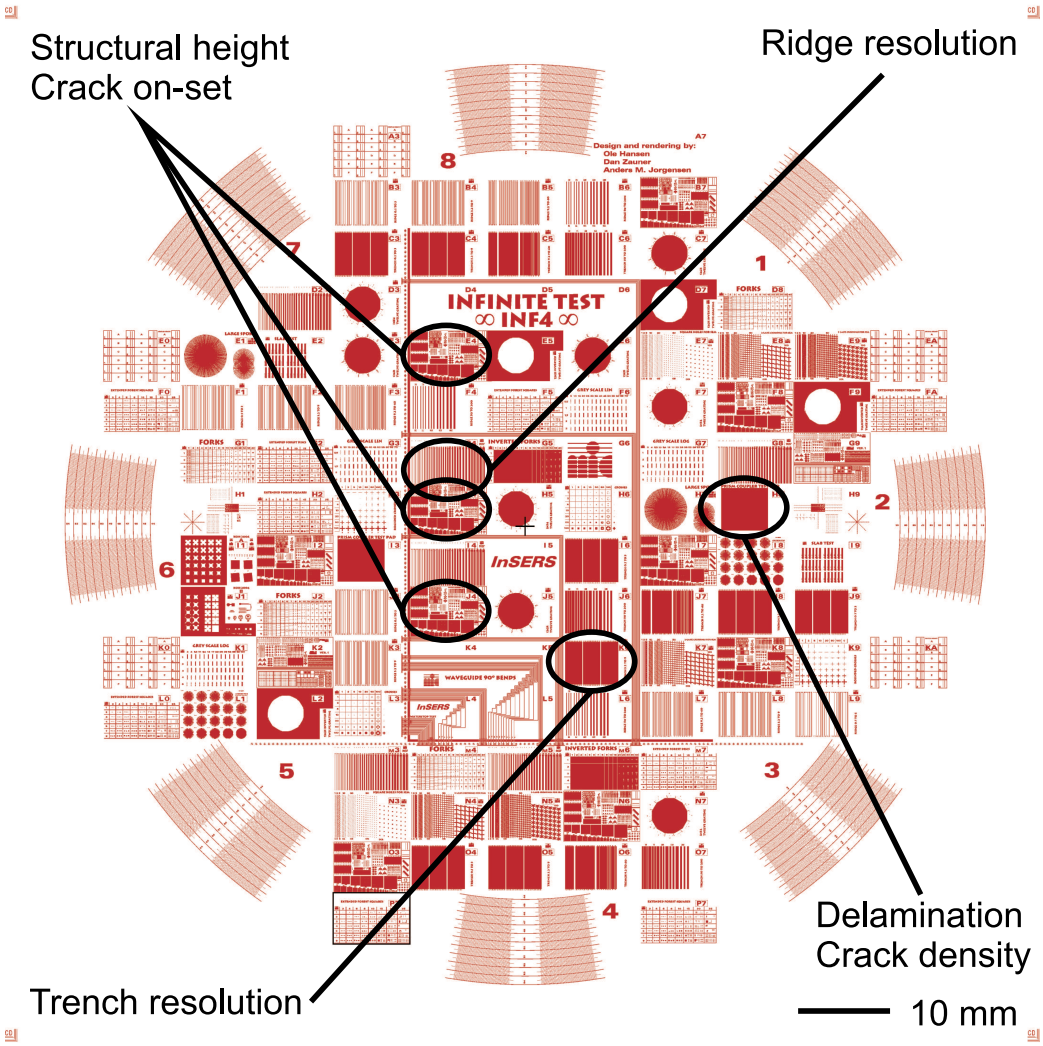

Figure 2.11: The layout of the test mask used in process development and optimization. The position of the monitor structures used in this project is indicated.

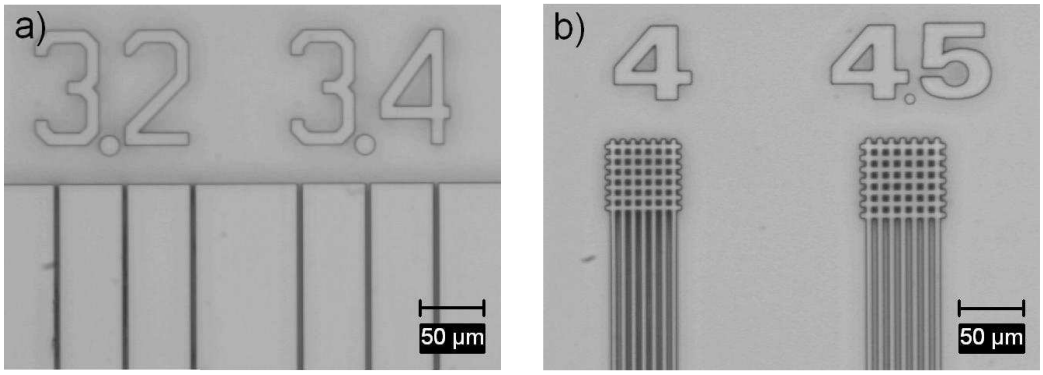

Figure 2.12: Optical micrographs of monitor structures used to assess the resolution of **a)** trenches and **b)** ridges. While the 4.5 μm ridge structure is seen to be fully resolved, the trench resolution is more unclear. However, microscope inspection reveals that the 3.4 μm trench structure is fully resolved.

0.5 μm. In both cases, the structures extend to a length of 5 mm. Figure 2.12 shows close-up pictures of one end of such trench and ridge monitors, respectively. A trench resolution of 3.4 μm signifies that the narrowest trench that is resolved all the way to the substrate is the 3.4 μm trench. A ridge resolution of 4.5 μm signifies that the 4.5 μm ridge structure is the smallest ridge structure that is fully resolved while maintaining structural stability.

2.7.2 Structural height

The structural height is measured across a 50 μm wide ridge using a stylus profilometer. The height is measured at three points for each wafer (see Figure 2.11). When the height of the structures is known, the values obtained from the resolution monitors may be transformed into the realized aspect ratios. The aspect ratios are obtained as the ratio of the average structural height to the resolution of the trench and ridge structures, respectively.

2.7.3 Cracking

During the bake processes, the difference in thermal expansion between the SU-8 and the substrate, and possibly shrinkage due to polymerization [36], causes tensile stress to build in the structures. Depending on the stress level, the material strength, and the strength of the bond between material and substrate, one of three scenarios may occur. The material may retain the stress and remain intact, it may release the stress by the formation of cracks, or it may release the stress by delaminating from the substrate.

Cracking is monitored using two different monitor structures. The crack on-set monitor consists of slabs of SU-8 with 10 μm by 10 μm square holes separated by a distance varying from 5 μm to 200 μm. The structure may be seen in Figure 2.14. The concave corners of the holes act as crack nu-

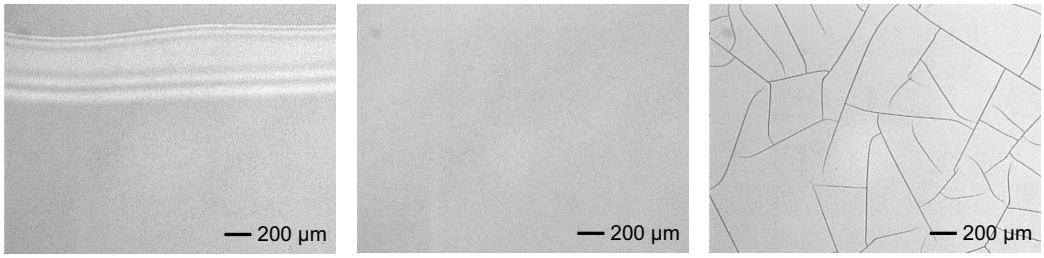

Figure 2.13: Optical micrographs of the crack density monitor structure. The pictures show a delaminated structure, a structure with no cracks, and a structure with a crack density of 6.7 %, respectively.

cleation points, and the structures thus monitor how much un-relieved SU-8 is necessary in order to build up the stress needed to form a crack in the material.

The second structure is a simple 5 mm by 5 mm slab designed to monitor the density of cracks in a continuous film. This structure is also used to monitor delamination. In the event of cracking, the crack density is determined by image analysis. A grayscale picture of the central 2.4 mm by 1.9 mm part part of the 25 mm^2 slab is obtained by optical microscopy, and cracks are colored using standard image editing software. The density of cracks is then computed as the ratio of the number of colored pixels to the total number of pixels. Figure 2.13 shows microscope pictures of such crack density monitor structures in the case of delamination, no cracking, and cracking. The crack density can never reach 100 % as cracking releases the stress in the surrounding material. The highest crack density seen during this project is 30.5 %.

2.7.4 The process monitor chip

The masks designed for fabrication of actual devices do not include all of the monitor structures mentioned above in the design. Instead a process monitor chip is included. This chip contains structures to monitor trench and ridge resolution (reduced in size and to a precision of 1 μm only), a structural height monitor structure, and the crack on-set monitor structure, among others. The layout of the process monitor chip is seen in Figure 2.14. Five to nine of these chips spread across the wafer are included in each mask design.

2.8 Lithographic Performance

The SU-8 process described in this chapter closely resembles the process recommended by the manufacturer [14]. SU-8 25 is spin coated onto oxidized silicon substrates which are soft baked in a two step procedure of ten minutes

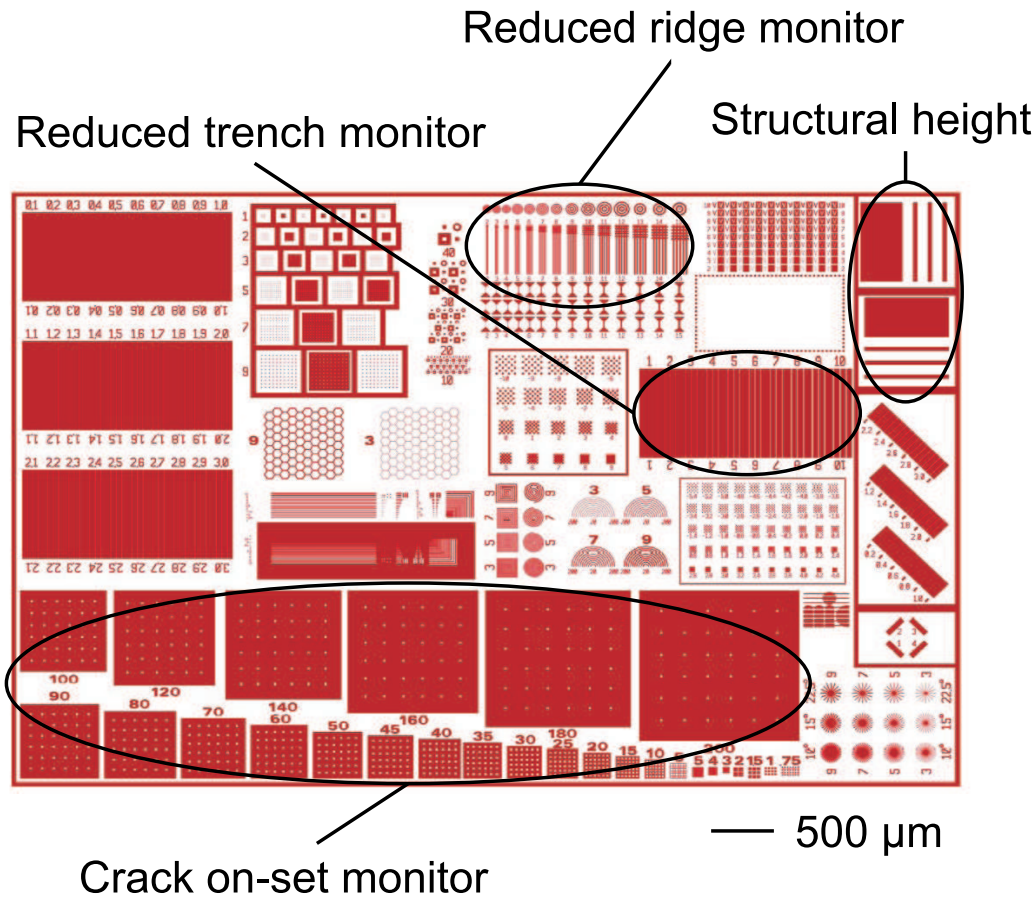

Figure 2.14: The layout of the monitor chip used for process monitoring on device masks. The position of the monitor structures used in this project is indicated.

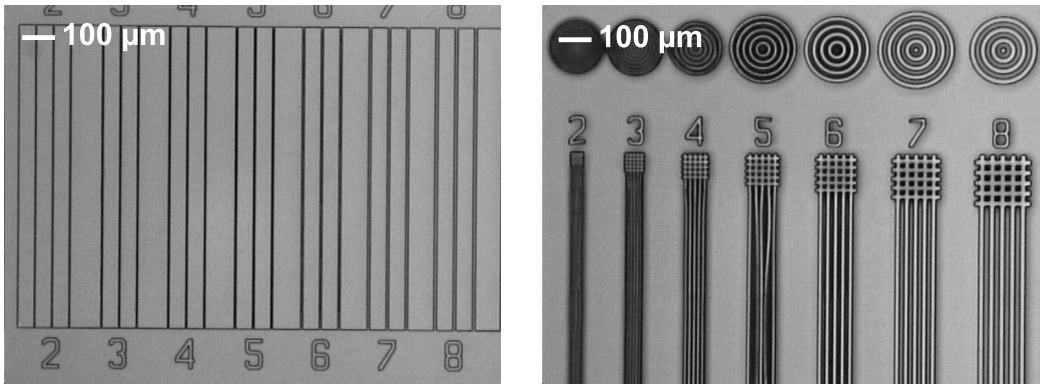

Figure 2.15: Optical micrographs of reduced monitor structures for lithographic resolution, processed using a process based on the manufacturer recommendations. The left hand side shows the 7 μm wide trench is open while the 6 μm trench is partially closed. The right hand side shows the ridge resolution monitor. Structural instability is clearly seen in the 5 μm structure.

at 65 °C and 30 minutes at 95 °C. After being exposed to 270 mJ/cm^2 of near-UV light at 365 nm through a photolithographic mask, the wafers are post-exposure baked at 95 °C for four minutes. Finally, the wafers are developed in agitated PGMEA for a total of ten minutes. Processing SU-8 according to this process results in 41 μm high structures which do not delaminate. Cracks are present at a density of $1 - 10$ %. The lithographic resolution is assessed through the monitor structures seen in Figure 2.15. The 7 μm trench is observed to be open, but the 6 μm is partially closed. With a pattern height of 41 μm, this corresponds to a realizable trench aspect ratio of 5.8. The ridge structures are observed to be limited by the lithographic resolution, rather than by structural instability.

The pattern transfer fidelity of the process at this point has not been characterized further. The subjects of line broadening and side wall angle for an optimized process are treated in chapter 4.

A reflection grating fabricated in SU-8 using this process is shown in Figure 2.2 on page 15. The fabricated grating is seen to be affected by line broadening and corner rounding. Integrated spectrometers based on such a grating shows transmission losses of at least 25 dB, corresponding to less than one in 300 photons making it through the spectrometer. In order to improve the performance, the SU-8 process was optimized through the introduction of an edge bead removal step, and through optimization of the process parameters.

Chapter 3

Edge Bead Removal

The edge bead resulting from the standard process as presented in the preceding chapter is shown in Figure 3.1. The edge bead protrudes more than 25 μm above the coating thickness. A 25 μm air gap between the mask and the resist reduces the theoretical resolution by 40 % (cf. section 2.4). The edge bead must thus be considered the single most limiting factor on the resolution of the lithographic process. It was therefore decided to develop a processing step with the purpose of minimizing the height of the edge bead.

The result of the optimized edge bead removal step is seen in Figure 3.1, which shows surface profiles of coatings processed with no edge bead removal, and using the optimized edge bead removal. Clearly the objective has been met; the edge bead is practically gone. The effect on the lithographic performance is equally substantial. The realizable trench resolution decreased from 7 μm for processing without edge bead removal to 4 μm for wafers processed using the optimized edge bead removal. This corresponds to an increase in the realizable trench aspect ratio from 6 to 10. No change was observed in the ridge resolution which remains at 7 μm.

Figure 3.2 shows the effect of the increased resolution on the spectrometer grating. Removing the edge bead drastically improves the pattern transfer fidelity, and the fabricated grating shows very little corner rounding. This is in sharp contrast to the result of processing without edge bead removal.

Before the details and optimization of edge bead removal process are presented, a short introduction to the concept of statistically designed experiments, or DOE, is given. The method of design of experiments is used both in the optimization of the edge bead removal process described in this chapter, and in the parameter investigation of the SU-8 lithographic process presented in chapter 4.

3.1 Design of Experiments (DOE)

Design of experiments, or DOE, is the concept of using statistics to plan a series of experiments that covers a specified portion of the parameter space without making any redundant experiments. The method is more efficient

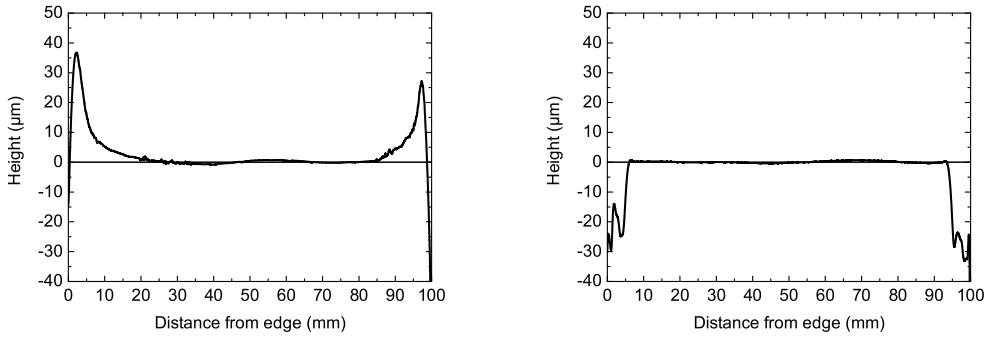

Figure 3.1: Profilometer line scans of the surface of 40 μm thick SU-8 25 coatings. The scans have been corrected for wafer bow. Left hand scan: No edge bead removal. The height of the edge bead is seen to be on the order of 30 μm. Right hand scan: The result of the optimized edge bead removal. The edge bead is on the same scale as the surface variations, and is thus practically non-existing.

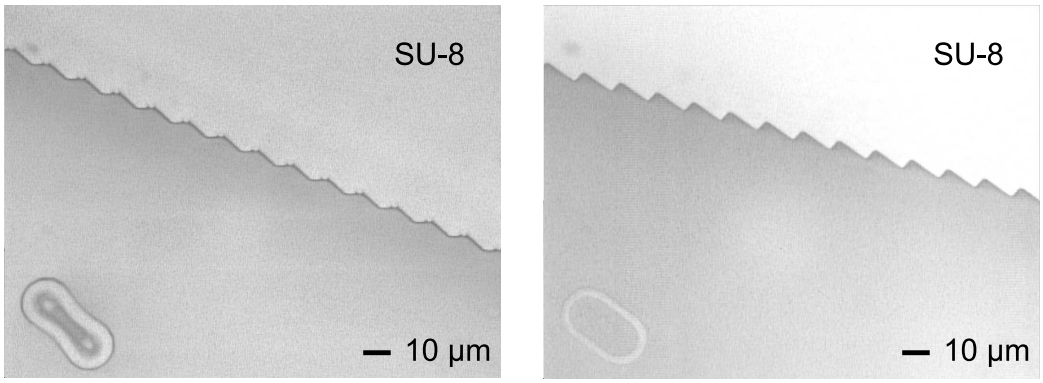

Figure 3.2: Optical micrographs of a 12th order grating fabricated in SU-8. The left hand side shows the result of processing with no edge bead removal, while the right hand side shows the effect of a successful edge bead removal. The pattern transfer fidelity of the lithographic process is seen to be dramatically improved by the edge bead removal.

than the one-factor-at-a-time approach used by many researchers (and indeed also in this project), both in terms of the number of experiments needed, and the amount of information gained from the experiments [37].

The purpose of this section is to introduce the procedures used. A more thorough introduction to the methods and statistics in design and analysis of experiments is given by Montgomery [38].

3.1.1 Designing experiments

As it is the case in any investigation, the first step in a design of experiments is to identify and describe the problem at hand. This enables the experimenter to identify the process responses of interest, to chose which process parameters should be included in the design (the so-called factors), and to chose the range over which each factor is to be varied in the design. These steps require process knowledge, in the form of practical experience and/or theoretical understanding of the process. The next step is the choice of the actual experimental design. Experimental designs have names such as *Box-Behnken*, and *Plackett-Burman* from the statisticians who developed them, or *A-optimal*, *D-optimal*, and *G-optimal* from the statistical criteria they are optimized according to. The choice of design is dependent on the number of factors and the level of information required from the experiments.

Once the details of the experiments have been planned, the time has come to perform the actual experiments. When the outcome of each experiment has been determined, statistical analysis of the result is performed. This usually involves establishing empirical models, i.e. equations that express the relationship between the responses and the factors in the design. If the goal of the design is to optimize the process, these models are used to perform numerical optimization. Models and optimization are validated through confirmation runs (extra experiments), where the performance of the process is compared to model predictions.

The two designs of experiments that were carried out during this Ph.D project were developed using the commercially available software MODDE 6.0 from Umetrics [39]. Modeling of the response surface, and the subsequent numerical optimization of the process based on the obtained models, was carried out using the same software. Once the pre-experimental planning (identification of the problem, choice of factors and ranges, and selection of responses) is carried out, the values are entered in the software, which subsequently produces a number of designs to choose from.

3.1.2 Modeling the result

Empirical models are obtained on the basis of the result of the designed experiments by means of response surface modeling. The response surface is modeled by multiple linear regression using MODDE. A model is characterized by two statistical coefficients of determination, the R^2-value and the

Q^2-value. The R^2-value is computed from the *explained sum of squares*, and is a measure of the portion of the variations of the response that is explained by the model. A large R^2-value does not necessarily signify a good model, as addition of extra variables always increases this value. The Q^2-value is based on the *prediction error sum of squares*, and expresses the model's capability of predicting the process outcome.

The starting point of the modeling is a model which includes every possible variable, typically each factor to first and second order, as well as first order interactions. A model of a response R in a design of experiments with three factors x, y, z can be expressed as

$$R = ax^2 + bx + cy^2 + dy + ez^2 + fz + gxy + hxz + iyz + j \tag{3.1}$$

The model is simplified through removal of insignificant variables, or terms. A term (e.g. the interaction term xz in equation (3.1)) is insignificant if the effect of the term (i.e. h) is smaller than the uncertainty associated with the effect. Insignificant terms are removed in order of least significance, until both R^2 and Q^2 decrease if the term is removed. In some cases, the result of an individual run may not represent the actual effect of the factors. These so-called outliers are identified through statistical testing. Outlying runs should be investigated for possible process errors. Runs that are classified as outliers are excluded from the model if the exclusion benefits the model (in terms of both R^2 and Q^2).

3.1.3 Optimizing the process

When empirical models for the individual responses have been established, an overall numerical optimization may be carried out to optimize the process. This optimization is also carried out using MODDE, in a process where the parameters are changed iteratively while the predicted outcome is compared to the optimization criteria. The outcome of such an optimization depends on the starting point of the iteration, so several starting points are usually processed in parallel.

The process parameter values returned by the optimization are adjusted to meet with the precision of the parameters used in the equipment, and are fed back into the models in order to predict the outcome of the optimized process. The optimization is validated by processing confirmation wafers according to the optimal recipe and subsequently comparing the responses to the outcome predicted by the models.

3.2 The Edge Bead Removal Process

As indicated in Figure 3.3, the edge bead removal is performed in three steps; a solvent reduction bake (SR), the actual edge bead removal (EBR), and a post-EBR spin cycle. Initial experiments had shown that edge bead

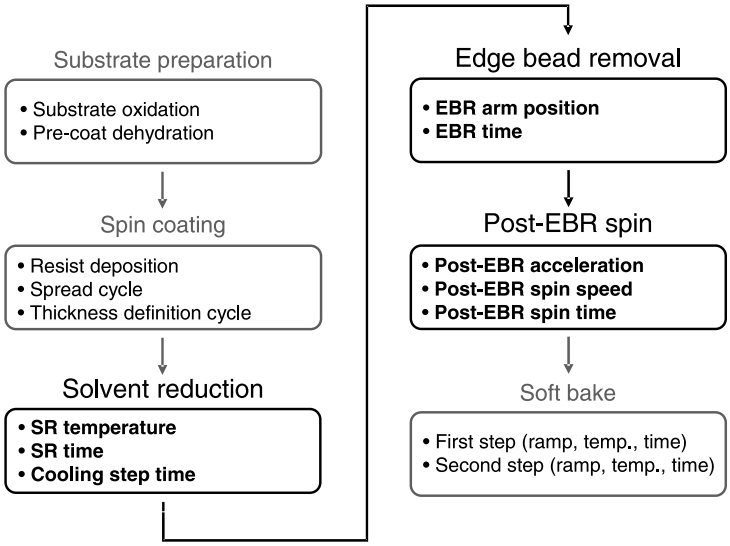

Figure 3.3: Process flow chart illustrating the steps and parameters involved in edge bead removal of SU-8.

removal was not reproducible when solvent was applied to a wet film, i.e. immediately after spin coating (see also [32]). An intermediate baking step was introduced with the purpose of reducing the amount of solvent in the coating, thus increasing the viscosity, making the film less prone to reflow. Solvent reduction is performed immediately upon spin coating, using the hotplate which is integrated in the spin coater. A robotic handler ensures reproducible timing of the baking start with respect to the spin coating. The wafer is transferred to the hotplate, which is preheated to the SR temperature, and held in contact by vacuum. After the duration of the SR time, the wafer is separated from the hotplate in three stages of increasing separation, before being transferred out. Each of these steps is separated by the cooling step time, which is thus a measure of how fast the film is cooled down at the end of the solvent reduction bake.

The actual removal of the edge bead is performed using the edge bead removal functionality of the spin coater. While the wafer spins at 500 rpm, solvent is applied at the edge of the wafer through a needle. The variables in the process are the position of arm that holds the needle, and the duration of the solvent application. The solvent used is the SU-8 developer PGMEA, which dissolves the SU-8 and removes the coating from the edge of the substrate. However, the resist close to the area where the solvent is applied will absorb some solvent and become more prone to reflow. The solvent thus removes the edge bead, but potentially creates a new, secondary edge bead from the reflowed SU-8. In order to minimize this effect, the wafer is subjected to a spin cycle immediately after the edge bead removal. The post-EBR spin cycle is intended to transfer the partly dissolved SU-8 onto the cleaned part of the substrate, thus minimizing the secondary edge bead.

It should be noted that the wafer rim does not necessarily have to be void of photoresist as long as the photoresist coating is thinner than the coating of the central area. After edge bead removal, the wafers are soft baked in a two-stage bake cycle consisting of 10 minutes at 65 °C and 30 minutes at 95 °C with 3 minute intermediate ramp times. As it is the condition of the coating that is of interest, no further processing is performed.

After the edge bead removal, the performance of the process must be characterized. The interesting features are how high the edge bead protrudes above the coating thickness, the distance between the protrusions at either edge of the wafer as this determines the maximum diameter of the potential quality area, and the roughness of the coating in the quality area. In order to determine the edge bead height, the edge bead distance, and the surface roughness, profilometer line scans of the surface of the coated wafers are used. Three profilometer scans, each over the full 100 mm width of the wafer, are performed on a Dektak 8 (Veeco, USA) stylus profilometer. The scans are oriented parallel to the wafer flat, perpendicular to the flat, and at an angle of 45° to the flat. The thickness of the SU-8 is measured across a pit formed in the centre of the wafer with a scalpel using a P1 Stylus Profilometer (KLA Tencor, USA).

The scanning data are analyzed using Excel (Microsoft, USA). First, the stress-induced wafer-bow is removed by subtracting a second order polynomial fitted to the central part of the profile. The resulting curve is then used to find the edge bead height as the average of the highest points on either side of the wafer. The edge bead distance is found as the distance between the highest points. The arithmetic roughness is calculated for the central 40 mm part of the curve. For each wafer representative values were selected for the responses based on the profilometer scans.

In recognition of the many factors potentially influencing the performance of the edge bead removal, it was decided to use the concept of design of experiment presented in the former section, in order to gain as much information from each experiment as possible.

3.3 The First Design of Experiments

Ideally, the edge bead height should be zero. The three other responses, the edge bead distance, the SU-8 thickness, and the surface roughness, are used as check responses, in order to ensure a useful result of the coating. A quality area of at least 80 mm in diameter is required, so the distance between the edge bead at either edge of the wafer must exceed 80 mm. Similarly, the SU-8 thickness can not be allowed to fall too far below the target of 40 μm, and the coating should not have excessive surface roughness.

Table 3.1 lists the eight factors in the edge bead removal investigation. The range of each factor is chosen to cover values expected to provide useful results. In an effort to reduce the number of factors, an initial screening experiment was carried out using a linear Plackett-Burman design with 15

Table 3.1: Factors in the design of experiment for edge bead removal. The range and optimized value of each factor as well as the unit are indicated. The optimized values are the result of a numerical optimization using the models extracted from the series of experiments. The unit apu (arm position unit) is an internal spinner unit, which corresponds roughly to the diameter (in mm) of the circle the needle describes above the spinning wafer.

Factor	Range	Optimized value	Unit
Solvent reduction temperature	$50 - 90$	50	°C
Solvent reduction time	$2 - 10$	9:23	min
Cooling step time	$10 - 50$	35	s
EBR arm position	$85 - 95$	90	apu
EBR time	$10 - 50$	40	s
Post-EBR spin acceleration	$100 - 3000$	2000	rpm/s
Post-EBR spin velocity	$500 - 3000$	1440	rpm
Post-EBR spin time	$10 - 50$	28	s

experiments. The screening proved the problem to be complex and prompted the design of a larger experiment. This series was based on the original screening experiment and used D-optimal design optimization to get the most information from each wafer. The final design consisted of 54 wafers. The design allows for response surface modeling with both second order and interaction terms. The response surface is modeled on the basis of the result of the experiment using multiple linear regression (MLR).

3.4 The Result of the First DOE

The range and median of the four responses in the edge bead removal experiment are listed in Table 3.2. The best run in terms of the edge bead height is one of the center runs, which has an edge bead height of only 1.5 μm. This result is however not confirmed by the other center runs (six in total since the screening also contained three center runs), which show an average edge bead height of 3.0 μm. The raw data of the experiment show no trends which could indicate a region in the parameter space of particular interest in terms of an optimized process.

The modeling of the edge bead height resulted in a statistically very sound model with an R^2-value of 0.999 and a Q^2-value of 0.972. Six of the 44 terms were removed from the model as they were insignificant at a 95 % confidence level. A total of five experiments were clasified as outliers, and excluded in the modeling. A plot of the values predicted by the model versus the observed values of the edge bead height is seen in Figure 3.4, which illustrates the high prediction capability of the model (cf. the high Q^2-value). Modeling of the check responses returned sound models with R^2-values in excess of

Table 3.2: Process response for various edge bead removals. The optimization is the predicted outcome of a process using the optimized values listed in Table 3.1. The confirmation is the actual result of the optimized process. The deviations give the 95 % confidence interval.

	Edge bead height (μm)	Edge bead distance (mm)	SU-8 thickness (μm)	Roughness (μm)
No EBR	26 ± 7	92.2 ± 0.3	41.3 ± 0.1	0.7 ± 0.7
Experiment range	$1.5 - 29.8$	$40.6 - 94.8$	$16.1 - 49.2$	$0.1 - 1.7$
Experiment median	6.2	77.2	40.4	0.4
Center prediction	3.7 ± 0.5	80.7 ± 1.0	40.7 ± 0.5	0.4 ± 0.1
Center runs	3.0 ± 1.1	79.6 ± 3.7	40.9 ± 0.6	0.5 ± 0.3
Optimization	0.67 ± 1.6	95.6 ± 2.0	42.5 ± 1.2	0.0 ± 0.1
Confirmation	0.64 ± 0.3	84.6 ± 2.2	38.7 ± 1.1	0.4 ± 0.5

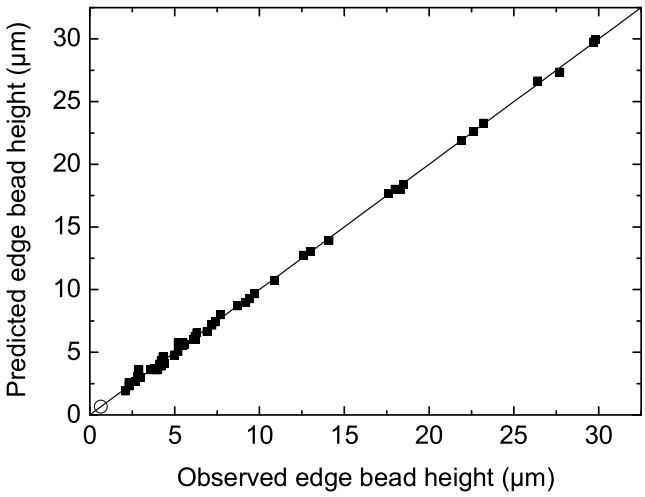

Figure 3.4: Comparison of the measured edge bead heights and the corresponding predictions from the model based on the data. The solid line indicates a perfect model. The spread of the points around the line is small, indicating that the model is good. The circle in the lower left hand corner represents the optimized process.

0.98 and Q^2-values above 0.9, except for the roughness model, which has a Q^2-value of 0.6. The prediction capability of all four models may be assessed in Table 3.2, which shows that the predictions of a recipe corresponding to the center values confirms the result of the center runs.

The EBR arm position and the EBR time are the most significant factors in the edge bead height model. The model shows the optimal arm position is 90 apu, and that the edge bead height decreases with increasing EBR time. The EBR arm position is the most significant term in all four models, followed by factors such as the EBR time, the post spin time, and the solvent reduction cool time. The effect of the arm position is dominated by the second order term, and the optimal position is 90 apu in all models.

3.5 Optimization

The edge bead removal process was optimized numerically on the basis of the obtained models. The optimization was carried out with an edge bead height target of 0.1 μm. The check responses were all given half the weight of the edge bead height in the optimization. Edge bead distance and SU-8 thickness were given a target of 95 mm and 41 μm, respectively, while the surface roughness was set to be minimized. A couple of optimization runs were necessary before the optimal recipe was determined. The optimized parameter values are listed in Table 3.1.

The numerical optimization was confirmed by processing a wafer using the optimized parameter values. The prediction and the result of the confirmation processing can be seen in Table 3.2. At 0.64 μm the edge bead height confirms the prediction, and represents a substantial improvement with respect to the starting point. The predictions of the check responses are not confirmed, but the result falls well within the acceptable range. As required, the diameter of the potential quality area is above 80 mm. At 38.7 μm the SU-8 thickness is below the target of 40 μm, but the thickness may eventually be fine-tuned through the spin coating parameters. The roughness is comparable to the starting point, indicating that no excessive roughness has been introduced by the edge bead removal process.

As presented in the preceding section, the most critical parameter in the process is the relative position of the applied solvent with respect to the wafer. This is a potential concern, as the needle that applies the solvent is a plastic needle, and thus subject to displacements if changed or accidentally pushed. However, the experience with the process following the optimization does not show this to be a problem. In all cases, it has been possible to counteract changes in the needle position by adjusting the arm position accordingly without any noticeable effect on the lithographic performance.

Chapter 4

Parameter Investigation

Following the successful development of the edge bead removal, the lithographic resolution had become sensitive enough to reveal the effect of changes in the process parameters (as it was seen in the case of the pre-development relaxation time in section 2.6). The removal of the edge bead had improved the trench resolution considerably, but the theoretical estimate of a 3 μm trench (cf. section 2.4) had not been reached. It was the notion that there was still something to be gained with respect to the performance of the lithographic process. The effect of the exposure dose had been investigated in order to determine the optimal exposure dose, but the influence of the soft bake and the post-exposure bake were still unknown. Suspecting the effect of each parameter in the lithographic process to be dependant on changes in the other parameters, a second design of experiments was planned. This effort would enable optimization of the process, and simultaneously provide information on the effect and significance of the parameters in the process.

The optimization of the lithographic process increased the realizable trench aspect ratio slightly, from 10.5 to 11.4. However, the optimal process parameters change the properties of the resist, which brings on significant changes in other responses. The realizable ridge aspect ratio increases from 5.1 to 8.8, which means that 4.5 μm wide ridges are stable. The increased resolution is accompanied by the total absence of cracks, a significant improvement to the normal crack density of around 5 %.

Scanning electron micrographs of gratings fabricated before and after the process optimization are seen in Figure 4.1. The effect of the process optimization is subtle and is not easily seen in the printed version of these scans. The diffraction effects from the corners of the grating, however, are observed to be reduced, and the pattern transfer to the bottom of the grating seems to be better.

4.1 The Second Design of Experiments

Figure 4.2 shows a flow chart of SU-8 processing. The spin coating, edge bead removal, and development steps had all been established prior to this

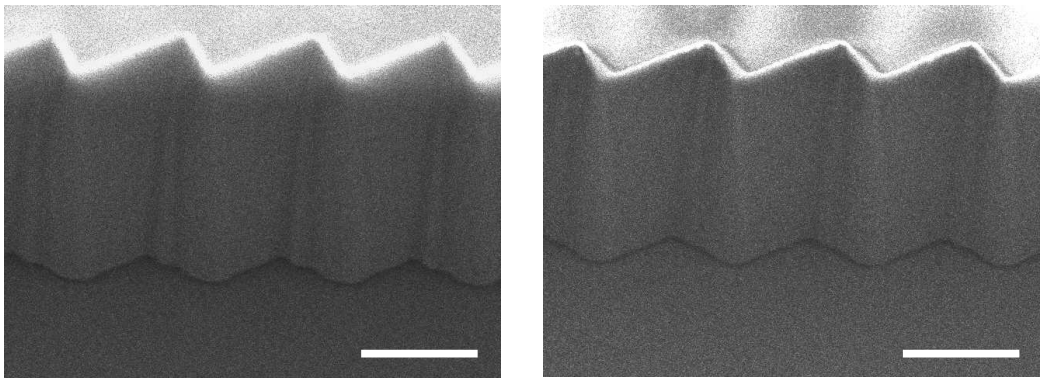

Figure 4.1: Scanning electron micrographs of a 12th order grating fabricated in SU-8. The left hand side shows the result of processing before the optimization of the process parameters. The right hand side shows the result of the optimized process. Both samples were tilted 30°. The poor quality of the scans is caused by charging effects as the the samples were not coated with gold in order to enable further processing. The scale bar represents 10 μm. Although this may be difficult to see in print, the the inspection shows that the protrusions in the concave corners of the grating are reduced in the optimized process, and that the definition of the grating at the substrate is improved.

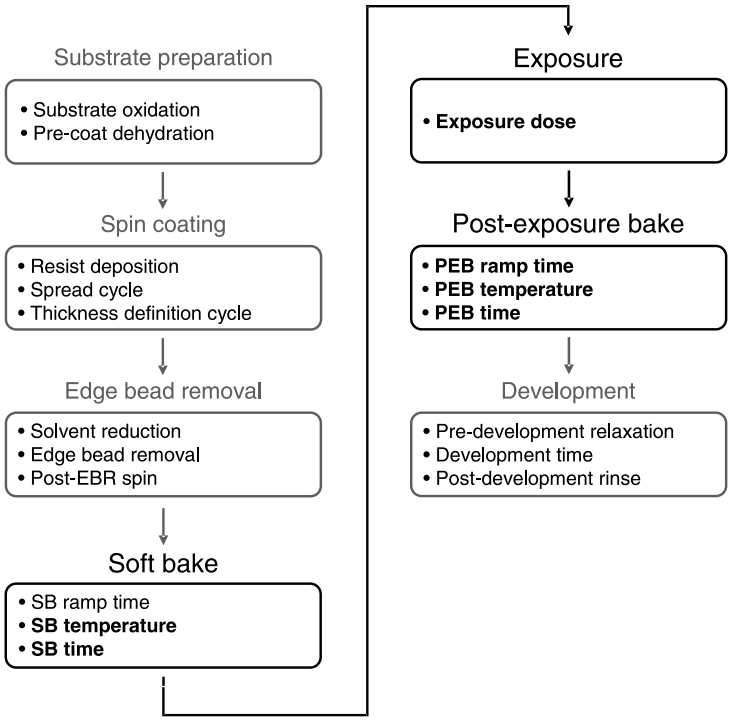

Figure 4.2: Process flow chart illustrating the steps and parameters involved in the processing of SU-8. The steps and parameters covered in the parameter investigation are highlighted.

Table 4.1: Factors in the designed experiment. The range and the center value of each factor as well as the unit are indicated.

Factor	Range	Center value	Unit
Soft bake temperature	65 – 110	95	°C
Soft bake time	5 – 55	30	min
Exposure dose	180 – 270	225	mJ/cm^2
Post-exposure bake ramp time	2 – 10	6	min
Post-exposure bake temperature	65 – 110	95	°C
Post-exposure bake time	2 – 30	4	min

investigation. The starting point for the investigation is a process very close to the one recommended by the manufacturer [14]. Apart from a few changes, the process is as it is presented in chapter 2. The addition of the edge bead removal step is the biggest change. Due to the fact that the coated substrates have already been baked in the solvent reduction step, the two-step soft bake is abandoned in favor of a single, ramped bake cycle with a fixed ramp time of six minutes. In accordance with the results of the investigation of the development procedure, a five minute total development time is used (cf. section 2.6). This leaves the soft bake temperature and time, the exposure dose, and the post-exposure bake ramp, temperature, and time as variable process parameters. Suspecting all of these factors to have significant influence on the performance, it was decided to use the design of experiments approach for the optimization of the process.

Table 4.1 lists the factors involved in the design of experiment. In the choice of the range of the factors, there was a desire to probe the extremes in order to ensure a good spread of the outcome. The lower limit of the baking temperature was set according to a desire to probe the low temperature region of parameter space without traversing the glass transition of non-cross-linked SU-8 around 50 °C [40]. The higher limit is set to avoid thermally initiated cross-linking which has been reported to start at temperatures above 130 °C [40]. In the cases where the range is not chosen symmetrically around the starting point, the factors are transformed in the design in order to give central values corresponding to the starting point of the optimization.

With the fabrication of reflection gratings in mind, the most important aspect of the processing is the reproduction fidelity of the mask pattern, i.e. the accuracy with which the mask design is reproduced in the resist. The pattern transfer is disturbed by line broadening, which in the the case of a negative resist affects the minimum obtainable trench width. Thus, trench resolution is regarded as the primary response. The ridge resolution is a secondary response, as the ability to fabricate stable ridges does not directly affect the fabrication of reflection gratings. During the execution of the design it became apparent that some of the runs resulted in delaminating structures. This is an unacceptable process outcome, and thus a binary

delamination response, i.e. delaminated or not delaminated, was included. Cracking does not necessarily lead to failure of the fabricated devices, but crack-free structures is a desirable outcome. Modeling the crack density proved to be difficult due to an overweight of samples with zero crack density. It was therefore decided to use a binary cracking response (cracked or not cracked) in the modeling. Both the cracking monitors have to be crack-free in order for the cracking response to be zero (not cracked). Binary responses are measured in logic units (1 or 0), but a model of the response will return predictions in the range from somewhere below zero to somewhere above one. These predictions can be interpreted as a measure for the risk of delamination or cracking, respectively. Thus, the figure of interest for these models is whether a prediction falls above or below 0.5. The height of the fabricated structures is used as a check response, primarily in order to assess over-development in the case of insufficient cross-linking. In the end the structural height may be fine-tuned through the spin coating parameters.

The experiments were planned using a central composite face (CCF) design, which yielded a design consisting of 47 runs. Executing this design as single runs in completely random order would have consumed approximately three months of work in the cleanroom. The practical execution of the experiment was thus done in batches of eight runs, each batch involving two different soft bake settings and two different post-exposure bake settings. Eight such batches were needed to cover the 47 runs in the design, which meant that a total of 64 runs were possible. It was decided to use the extra slots for additional runs. One of these additional runs was used to supplement the design with a fourth center point. The remaining runs were chosen randomly from points in the parameter space not represented in the CCF design. The final design was executed over a period of one month.

The additional runs allowed for a number of so-called uncontrollable factors to be included in the modeling. These factors are process parameters which are monitored, but not easily controlled, during processing, such as the waiting time between subsequent steps, the number of prior prints with the mask, and the developer condition. The design allows for response surface modeling (RSM) covering the important design factors to first and second order as well as interaction terms. The uncontrollable factors are included to first order only. The response surface is modeled on the basis of the result of the experiment using multiple linear regression (MLR).

4.2 The Result of the Second DOE

Following the execution of the designed experiments the wafers are characterized. Range and median of the process responses in the investigation are listed in Table 4.2. The two overall best processing results in the investigation are found to result from processing with low baking temperature in both soft bake and post-exposure bake. These show trench and ridge resolution of 3.4 μm and 5.0 μm, respectively. Contrary to the standard process, which

Table 4.2: Responses in the parameter investigation. The range and median of the responses are listed.

Response	Experiment range	Experiment median
Trench resolution	$3.2 - 11$ μm	4.6 μm
Ridge resolution	$5 - 20$ μm	8.0 μm
Delamination	0; 1	0
Cracking	0; 1	1
Crack density	$0 - 27.6$ %	0.0 %
Pattern height	$32.7 - 40.2$ μm	37.6 μm

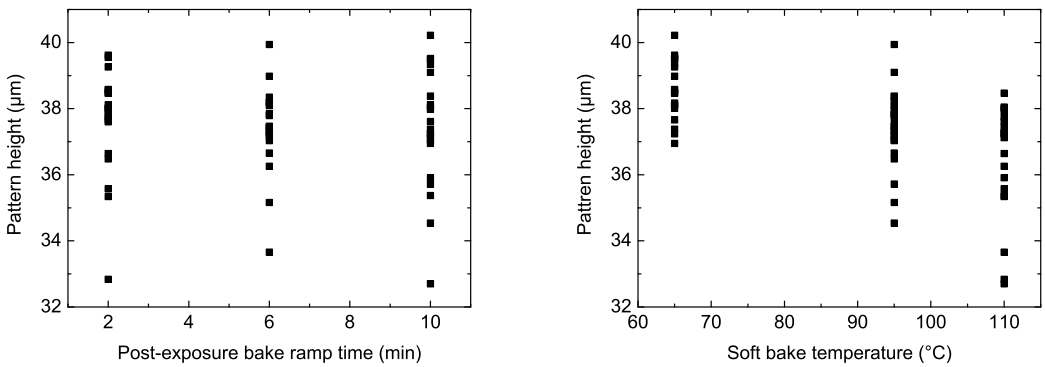

Figure 4.3: Examples of scatter plots of the raw data from the second DOE. The plots show the pattern height as a function of the PEB ramp time and the soft bake temperature, respectively. While the results are scattered randomly as a function PEB ramp time, there seems to be a trend towards a lower pattern height with increasing soft bake temperature.

usually results in a crack density around 5 %, these samples show absolutely no cracking.

Analysis of the raw data may provide information about the effect of the different factors. The experiment result is represented as scatter plots of responses versus design factors. In most cases the data points are spread in a random manner, showing no obvious trend. Figure 4.3 shows examples of such scatter plots in the case of no visible trend as well as in the case of a clear trend. The result of the second DOE, however, contains much more information than what can be learned from raw data analysis. In order to unlock this information, and enable optimization of the process, the result is used to obtain empirical models of the process responses. The actual optimization of the process came to pass in three steps involving two different sets of models.

Table 4.3: Process parameter values for different recipes. The first optimization is based on the trends observed in the raw data. The second optimization and the third optimization are the result of numerical optimizations of the empirical models.

Factor	First optimization	Second optimization	Third optimization	Unit
SB temperature	**65**	65	65	°C
SB time	**5**	5	8	min
Exposure dose	**180**	252	180	mJ/cm^2
PEB ramp time	**6**	6	6	min
PEB temperature	**65**	84	68	°C
PEB time	**30**	5	15	min

4.3 Optimization

The optimization of the lithographic process based on the designed experiments was performed in three steps. The first optimization was an educated guess, based on the most successful runs in the investigation, as presented in section 4.2. The second optimization is the result of a numerical optimization, based on the models that were obtained on the basis of the experiment. This optimization, and thus the models, failed to perform in the confirmation, proving the second optimization a failure. As a consequence, the original design was supplemented with a series of runs, and a second set of models were obtained. The third optimization was performed on the basis of these models. This numerical optimization mimics the result of the first optimization in both parameter values and predicted process result.

The process parameter values suggested by the three optimizations are listed in Table 4.3. The optimal process is the recipe suggested in the first optimization. The performance of this process is described further in section 4.5.

4.3.1 First optimization

Based on the raw data observations an informed guess of an optimized process was made. The process parameter values of this first optimization may be seen in Table 4.3. A soft bake of 5 minutes at 65 °C, a low exposure dose, and a post-exposure bake temperature of 65 °C was chosen. The post-exposure bake time was set to 30 minutes in order to exploit the full cross-linking potential.

The result of processing according to the first optimization may be seen in Table 4.4. With a trench resolution of 3.5 μm, a ridge resolution of 4.8 μm, and no cracks, the result confirms the expectations based on the best results of the designed experiment (cf. section 4.2).

Table 4.4: Comparison between the predictions of the models based on the original design and actual processing results. The deviations give the 95 % confidence interval.

First models	Trench resolution (μm)	Ridge resolution (μm)	Delamination	Cracking	Pattern height (μm)
Center prediction	2.8 ± 0.7	6.7 ± 0.9	-0.04 ± 0.06	1.01 ± 0.06	37.4 ± 0.2
Center runs	3.8 ± 0.3	7.1 ± 0.4	0	1	37.6 ± 0.6
1st optimization	1.9 ± 1.4	4.6 ± 1.8	-0.06 ± 0.13	0.16 ± 0.20	38.5 ± 0.5
Confirmation	3.5 ± 0.6	4.8 ± 1.4	0	0	39.3 ± 0.5
2nd optimization	1.0 ± 1.1	0.0 ± 1.8	0.18 ± 0.12	-0.01 ± 0.18	39.6 ± 0.4
Confirmation	4.5 ± 0.3	5.0	0	0	38.8 ± 0.7

4.3.2 Second optimization

In the next step of the analysis, the result of the experiment was used to build empirical models of the responses. With some effort, reasonably sound models were obtained, with R^2-values and Q^2-values around 0.9 and 0.8, respectively.

The obtained models were used to optimize the process on the basis of the experiment. The numerical optimization was set to minimize trench resolution, ridge resolution and delamination. Ridge resolution was given a weight of 0.5 with respect to trench resolution and delamination. The check responses were given weight 0.25, and were optimized towards no cracking and a target of 40 μm in the case of the pattern height. The values of the processing factors suggested by the second optimization are listed in Table 4.3. The numerical optimization mimics the short low temperature soft bake chosen in the first optimization, but suggests a higher post-exposure bake temperature and a quite high exposure dose. The models predict an optimum trench resolution of 1 ± 1 μm and a ridge resolution of 0 ± 2 μm. While a trench resolution of 1 μm would be a nice result indeed, the ridge resolution is dubious as the lower limit of the ridge resolution is set by the trench resolution. The validity of the models was assessed through a series of confirmation runs. Wafers were processed using the process parameter values suggested in the first optimization and the second optimization, respectively. In both cases three wafers were processed. The process outcome is given by the mean of the measured responses. The standard deviation of the responses is corrected to a 95 % confidence level using Students t-distribution. The result of the confirmation runs are listed in Table 4.4 along with the results predicted by the models. Also included in the table is the predicted result of the center process and the average result of the four center points in the design. As Table 4.4 shows, the models struggle to predict the trench resolution satisfactorily. This is especially so in the case of the second optimization where the result is a trench resolution of 4.5 μm. The other responses are confirmed within the confidence interval, except for the ridge resolution in the

Table 4.5: The range and median of the responses in the augmented design. The R^2 and Q^2-values (see section 3.1 for definitions) of the empirical models obtained on the basis of the experiment are also listed.

Response	Experiment range	Experiment median	Model R^2-value	Model Q^2-value
Trench resolution	$3.2 - 11$ μm	4.4 μm	0.88	0.78
Ridge resolution	$4.5 - 20$ μm	8.0 μm	0.80	0.63
Delamination	0; 1	0	0.88	0.71
Cracking	0; 1	1	0.89	0.77
Crack density	$0 - 30.5$ %	0.0 %	-	-
Pattern height	$32.7 - 40.2$ μm	37.8 μm	0.93	0.89

case of the second optimization which, as expected, is limited by the trench resolution.

4.3.3 Third optimization

Following the failure of the first models to optimize the process, it was decided to supplement the design with the wafers processed as confirmation of the models. The series of wafers processed for the investigation of the polymerization temperature presented in section 4.6 was also included. A total of twelve extra experiments were included in the augmented design. With the new information, a set of revised models were obtained. The range and median of the augmented design, and the R^2 and Q^2-values of the models are listed in Table 4.3.3. The models are described in the next section.

The revised models were used for numerical optimization of the process. As trench resolution is viewed as the primary response, it was decided to omit ridge resolution and cracking in the third optimization. Pattern height was given a weight of 0.25 with respect to trench resolution and delamination, and optimized towards a target of 40 μm. In order to allow for the optimization to focus on the controllable factors, the uncontrolled factors were fixed at values typical for a standard process run. The result of the second optimization is shown in Table 4.3. The suggested process is very close to the first optimization. Soft bake temperature and exposure dose are equal, the soft bake is a few minutes longer, while the post-exposure bake is at a slightly higher temperature for a shorter time.

The predictions of the revised models are compared to the confirmation of the original design in Table 4.6. The predictions are in good agreement with the process results. It seems the revised models have a much better chance of predicting a correct process outcome, than the first set of models. As the included runs were chosen in a far from random manner, the augmented design is biased towards low baking temperatures, and may thus not be able to successfully predict the outcome of high temperature processing. However,

Table 4.6: Comparison between the predictions of the models based on the supplemented design and actual processing results. The confirmation values are from the confirmation of the original design. The deviations give the 95 % confidence interval.

Revised models	Trench resolution (μm)	Ridge resolution (μm)	Delamination	Cracking	Pattern height (μm)
Center prediction	4.0 ± 0.4	7.8 ± 1.5	0.02 ± 0.08	0.94 ± 0.09	38.2 ± 0.3
Center runs	3.8 ± 0.3	7.1 ± 0.4	0	1	37.6 ± 0.6
1st optimization	3.1 ± 0.6	5.6 ± 2.0	-0.13 ± 0.10	0.14 ± 0.18	39.3 ± 0.4
Confirmation	3.5 ± 0.6	4.8 ± 1.4	0	0	39.3 ± 0.5
2nd optimization	3.7 ± 0.5	3.7 ± 1.6	0.06 ± 0.10	0.07 ± 0.16	39.1 ± 0.4
Confirmation	4.5 ± 0.3	5.0	0	0	38.8 ± 0.7
3rd optimization	3.1 ± 0.6	6.0 ± 1.9	-0.14 ± 0.10	0.16 ± 0.17	39.1 ± 0.4

even the raw data show the low temperature region of the parameter space to be the region of interest. Also included in Table 4.6 is the prediction of the third optimization. Within the confidence interval the prediction is equal to the prediction of the first optimization. With such little difference in predicted outcome between the two recipes, there is no need for confirmation runs. In practice the two are equal, and the first optimization, made on the basis of the raw data trends, is the optimal process.

4.4 The Models

Describing the obtained models is no easy task. Without exception, the models contain second order terms and interaction terms, and the first order term is seldom the most significant. It is thus not possible to identify any single most significant factor in the system. The effect and significance of each factor in the individual models may be assessed by evaluating the predicted process outcome around a fixed point in the parameter space. Prediction plots of the trench resolution model around the center point and the optimal process point are shown in Figure 4.4 and Figure 4.5, respectively.

4.4.1 Trench resolution

Figure 4.4 shows prediction plots of the trench resolution model around the center point. The post-exposure bake temperature is the most significant factor; the prediction ranges from a value of 4.0 μm for a PEB temperature of 95 °C to 5.7 μm at 110 °C. For comparison, the prediction changes only 0.6 μm over the soft bake temperature range. In the case of the soft bake time, the prediction falls within the 95 % confidence interval over the entire range. The soft bake time is thus insignificant at this confidence level. The same is true for the exposure dose. The model shows optimum result, i.e.

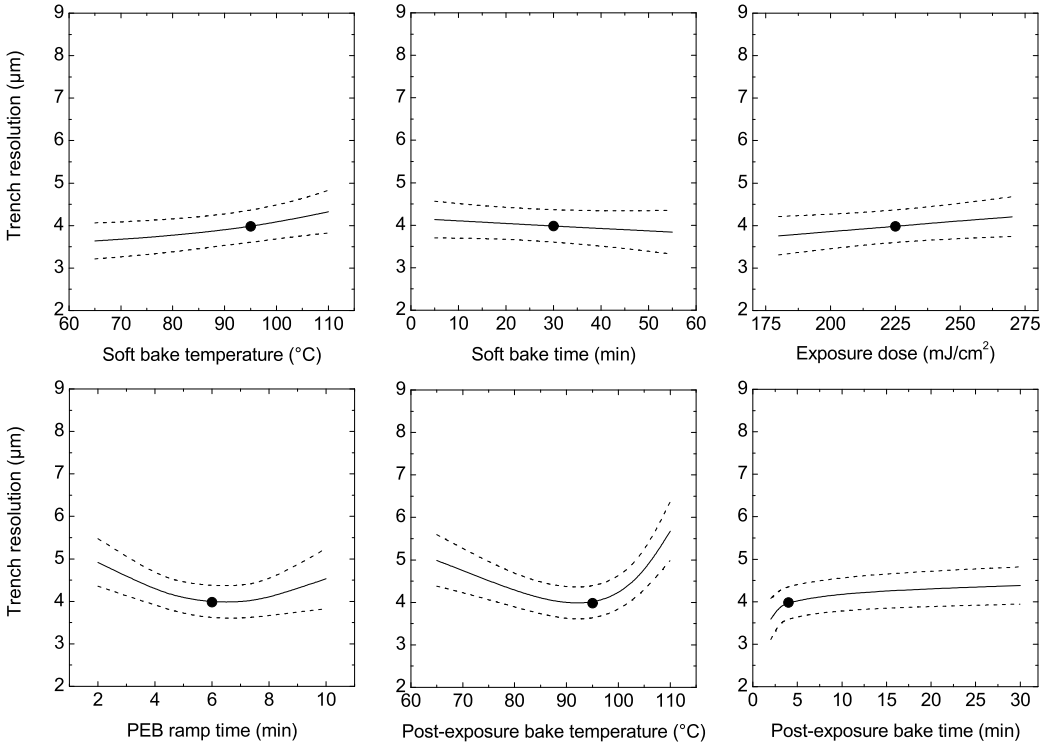

Figure 4.4: Prediction plots of the trench resolution model at the center point (see Table 4.1). The dashed lines indicate the 95 % confidence interval.

lowest trench resolution, for a PEB temperature slightly below 95 °C and low PEB time. A low soft bake temperature is optimal, and the optimum post-exposure bake ramp time is 6 minutes.

Prediction plots around the optimal process point (the first optimization in Table 4.3) are shown in Figure 4.5. When the model is evaluated around the optimal process point, there are many similarities to the predictions around the center point. The PEB temperature is the most significant factor, and soft bake time and exposure dose are both insignificant. However, here the PEB time is insignificant, and the model shows optimum result at low PEB temperature. As at the center point, a low soft bake temperature is optimal, and the optimum post-exposure bake ramp time is 6 minutes.

4.4.2 Delamination

Evaluation of the delamination model around the center point and the optimal process point shows the PEB temperature to be the most significant factor. Around the center point, the model shows no sign of delamination. The safest seems to be high SB temperature and low PEB temperature. In the case of low temperature processing, as for the optimal process, the risk of delamination becomes significant for PEB temperatures above 95 °C.

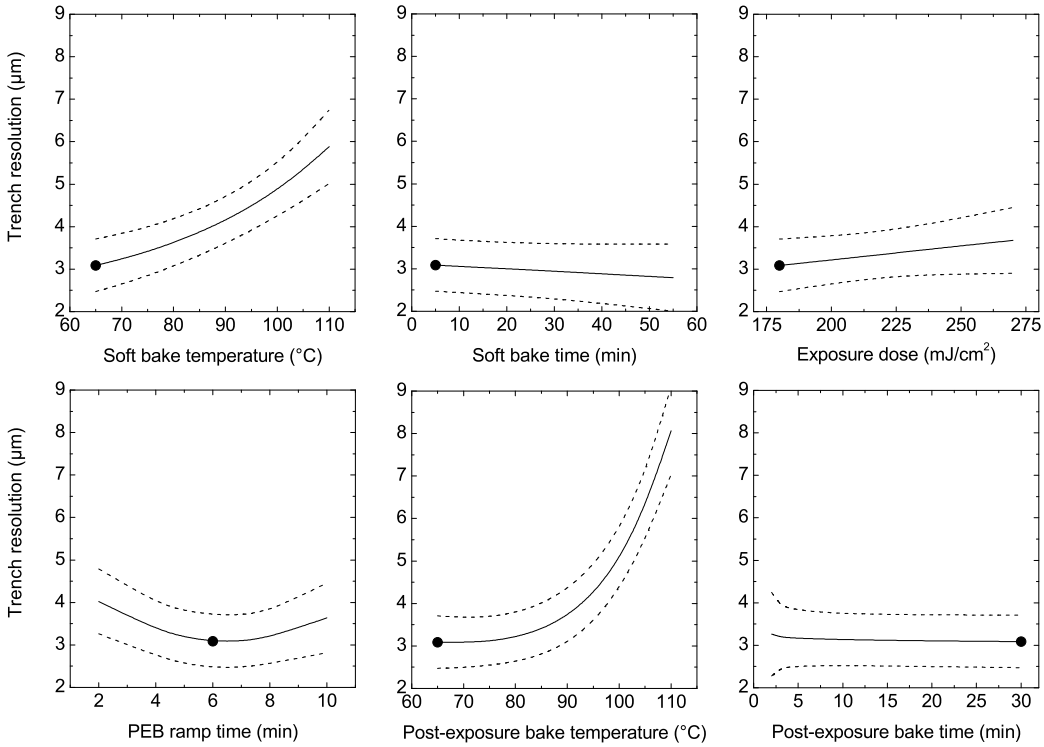

Figure 4.5: Prediction plots of the trench resolution model at the optimal process point (the first optimization in Table 4.3). The dashed lines indicate the 95 % confidence interval.

4.4.3 Cracking

In the case of the cracking model, the most significant factor is the SB temperature. Exposure dose, PEB temperature, and PEB time are all insignificant. Evaluated around the center point the model shows that the outcome will always be cracked structures, except maybe for at the very lowest SB temperature. Around the optimal process the SB temperature and the SB time have almost equal significance. A short soft bake at a low temperature ensures crack-free structures, but baking either at a higher temperature or for too long will result in cracking.

4.4.4 The effect of uncontrollable factors in the models

A number of the uncontrollable factors appear in the obtained models. These are the waiting time between spin coating and edge bead removal (EBR wait time), the waiting time between edge bead removal and soft bake (SB wait time), the waiting time between exposure and post-exposure bake (PEB wait time), and the developer usage. None of these appear in all models, in fact most are only present in a single model. Identifying the one of these factors which is most significant in the processing of SU-8 is thus difficult. A period of relaxation prior to the soft bake appears to be beneficial as the risk of cracking is decreased significantly at a SB wait time of two hours. The PEB wait time, on the other hand, should be as short as possible, as the risk of cracking is increased with increased wait time. Finally, a used developer reduces the risk of delamination compared to a fresh developer.

4.5 The Optimal Process

The optimization of the lithographic process resulted in a choice of process parameters which is quite far from the manufacturers recommendations [14]. The optimal process (cf. the first optimization in Table 4.3) prescribes baking temperatures 30 °C below the recommended temperature, and an exposure dose below the recommended exposure dose range ($200 - 330$ mJ/cm^2). It is therefore interesting to compare the performance of the optimal process to the performance of a process similar to the recommended process. Also, the optimal exposure dose is not necessarily within the range investigated in the design of experiment.

At the point in the parameter space corresponding to the optimal process, the pattern height model predicts a dose independent pattern height over the entire exposure dose range (180 mJ/cm^2 to 270 mJ/cm^2). This raises the question whether the optimal exposure dose at this point is somewhere below 180 mJ/cm^2. In order to investigate this, a series of wafers were processed using exposure doses between 45 mJ/cm^2 and 270 mJ/cm^2 in steps of 45 mJ/cm^2. A dose of 45 mJ/cm^2 is below the critical dose, as all but the smallest structures are lifted off in the development. At higher doses the

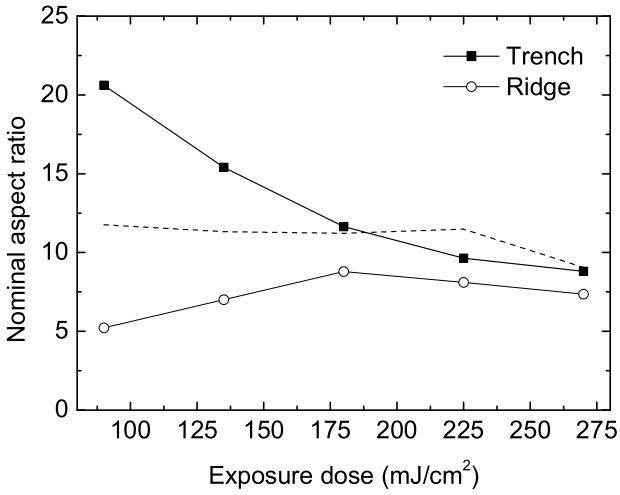

Figure 4.6: Nominal trench and ridge aspect ratio as a function of exposure dose for the optimal process (the first optimization in Table 4.3). The aspect ratios are based on the trench and ridge resolution, and do not necessarily represent the size of the developed structure (cf. Figure 4.7). The dashed line indicates the actual obtainable trench aspect ratio, estimated from SEM inspection.

process is successful, yielding stable structures with a height around 39.5 μm. There is no clear trend in the pattern height as a function of exposure dose. All samples have zero crack density, but the samples with exposure doses below 180 mJ/cm^2 show cracks in the crack on-set monitor structures. Using the pattern height, the trench and ridge resolutions are transformed into a nominal aspect ratio. This aspect ratio corresponds to the obtainable aspect ratio if the pattern transfer fidelity is 100 %. The result is seen in Figure 4.6.

In order to assess the pattern transfer fidelity, the actual widths of the narrowest, fully resolved trenches were measured using scanning electron microscopy. In order to preserve the samples for further processing, they were not cleaved, and not covered with gold (usually applied in order to prevent charging of the sample). The wafers were loaded into the SEM, and one end of the trench monitor structures was inspected at an angle of 30°. The inspection revealed an almost constant minimum trench width of 3.4 ± 0.1 μm, regardless of the mask feature responsible for it. Only for the largest exposure dose does the minimum trench width increase to 4.5 μm. This corresponds to a maximum obtainable trench aspect ratio of 11.4. The actual widths of the trenches with a nominal width of 6.0 μm were also measured. The width at the top of the trench reveals a dose dependent trench broadening. The width at the bottom is used to determine the sidewall angle. The trench broadening is seen in Figure 4.7.

The sidewall angle increases with increasing exposure dose, but is below

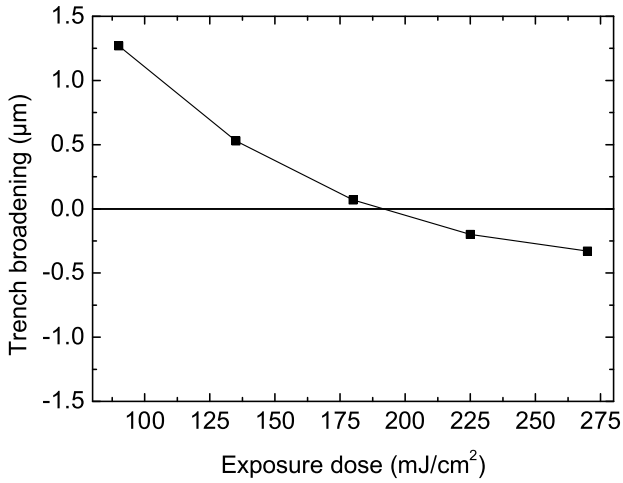

Figure 4.7: Trench broadening as a function of exposure dose for the optimal process (the first optimization in Table 4.3). The trench broadening is determined from SEM inspection of trenches with a nominal width of 6.0 μm.

1° for the whole series. At 90 mJ/cm^2 the trench is actually broadest at the bottom, revealing that this dose is close to the critical dose.

The optimal exposure dose is the dose for which the dimensions of the fabricated structures are equal to the designed mask pattern, i.e. the pattern transfer fidelity is 100 %. By comparing the nominal trench aspect ratio to the actual aspect ratio, as in Figure 4.6, the optimal dose is seen to be approximately 190 mJ/cm^2. Figure 4.7 confirms zero trench broadening at this dose. At 180 mJ/cm^2 there is no cracking, even at concave corners, and the sidewall angle is 0.5°. The ridges are stable up to an aspect ratio of 8.8. Analysis of similar inspections of the process corresponding to the starting point for this investigation (i.e. baking at the standard temperature of 95 °C), see Figure 4.8, reveals an optimal dose of 225 mJ/cm^2. At this point, the maximum obtainable trench aspect ratio is 10.5 while the ridges are stable up to an aspect ratio of 5.1.

4.6 Investigation of the Effect of the Soft Bake Temperature

During the post-exposure bake, the exposed resist polymerizes by cross-linking of the SU-8 monomers. The rate at which polymerization occurs and the resulting cross-link density depends on the processing conditions. In some of the first runs in the execution of the second DOE it was observed that the image of the mask was visible on wafers soft baked at 65 °C already

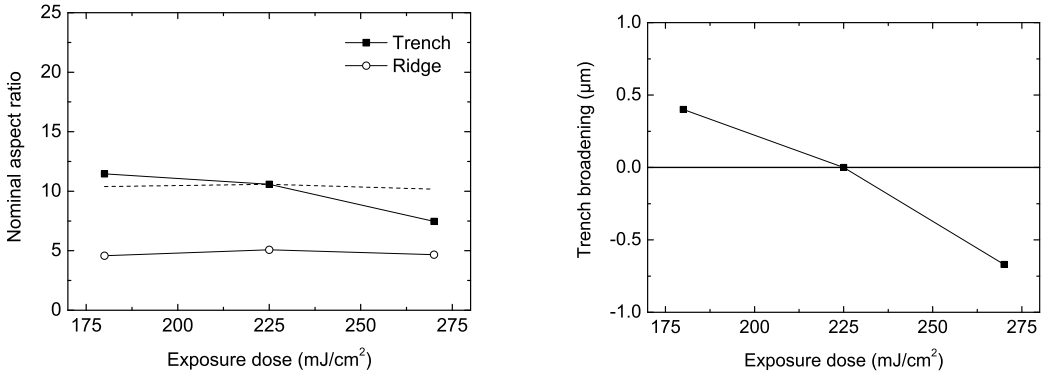

Figure 4.8: Nominal aspect ratio and trench broadening as a function of exposure dose for the center point of the investigation (see Table 4.1). The dashed line indicates the actual obtainable trench aspect ratio, estimated from SEM inspection. The trench broadening is determined from SEM inspection of trenches with a nominal width of 6.0 μm.

before the post-exposure bake was initiated, while the image only developed well into the PEB for wafers soft baked at higher temperatures. As a consequence, it was decided to log the point at which the image appears in subsequent runs. This *polymerization temperature* is based on an observation of the temperature in the post-exposure bake at which the image of the mask first becomes visible on the substrates. The polymerization temperature is recorded from the hotplate controller. As the polymerization is a kinetic process, the observed polymerization temperature will depend on the time between exposure and PEB initiation, as well as on the temperature ramping rate during the PEB.

After the execution of the second DOE, a model of the polymerization temperature was established. As would be expected, the model only contains factors from the processes preceding the PEB. In fact, the only three factors that appear in the model are the soft bake temperature, the soft bake time, and the PEB ramp time. The soft bake temperature is by far the most significant factor. The raw data show that soft baking at 65 °C results in a polymerization at a temperature close to room temperature, while soft baking at 95 °C or 110 °C results in a polymerization temperature around 40 °C. It is evident that there is a significant change in the polymerization process with increasing temperature, and that the interesting range is the range from 65 °C to 95 °C. Thus it was decided to investigate the effect of the soft bake temperature on the polymerization temperature and the lithographic performance in a separate *single factor investigation.* A series of six wafers were processed with soft baking temperatures changing from 65 °C to 115 °C in steps of 10 °C. The other process parameters were fixed at a soft bake time of 5 minutes, an exposure dose of 225 mJ/cm^2, and a PEB at 65 °C for 30 minutes with a ramp time of six minutes.

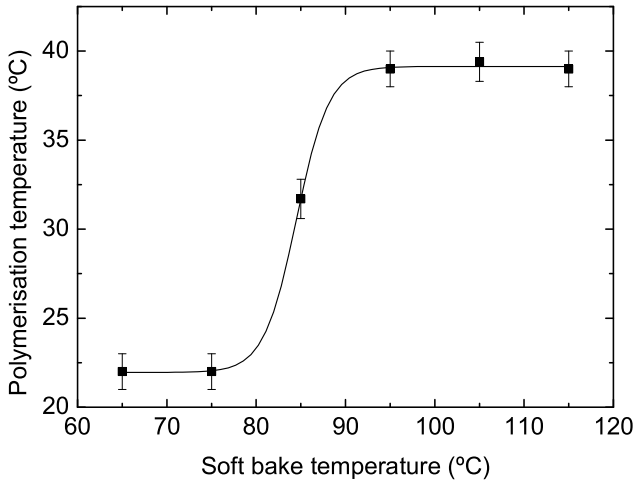

Figure 4.9: Observed polymerization temperature as a function of the soft bake temperature. The error bars represent the readout precision. At low soft bake temperatures, the polymerization temperature is disturbed by the fact that the ambient temperature sets the lower limit (i.e. the plateau at low temperature is most likely artificial). The line is a guide to the eye.

4.6.1 Polymerization temperature

The observed polymerization temperature as a function of soft bake temperature is presented in Figure 4.9. At the lowest soft bake temperatures, cross-linking was already evident when the PEB was initiated. The polymerization temperature is thus set to the temperature of the processing ambient (22 °C). However, while the image on the sample soft baked at 75 °C took approximately 15 minutes to develop, faint traces were visible directly upon exposure of the wafer baked at 65 °C, indicating that polymerization would have been initiated even at a lower temperature. The apparent plateau at low soft baking temperatures is thus an artifact due to the temperature of the processing ambient. At higher soft bake temperatures, the polymerization temperature rises, saturating at 39 °C for soft bake temperatures of 95 °C and above.

The increase in polymerization temperature with increasing soft bake temperature suggests solvent level dependent polymerization kinetics. As the soft bake temperature increases, the solvent concentration in the soft baked SU-8 decreases, reaching an apparently constant level at temperatures of 95 °C and above. The faster kinetics at low soft bake temperature could be explained by higher mobility in the SU-8 matrix, due to the higher solvent concentration. However, the solvent concentration may also affect the photoacid generation process. During exposure, the organic cation of the onium salt is destroyed and the salt decomposes [11]. The anionic part reacts with

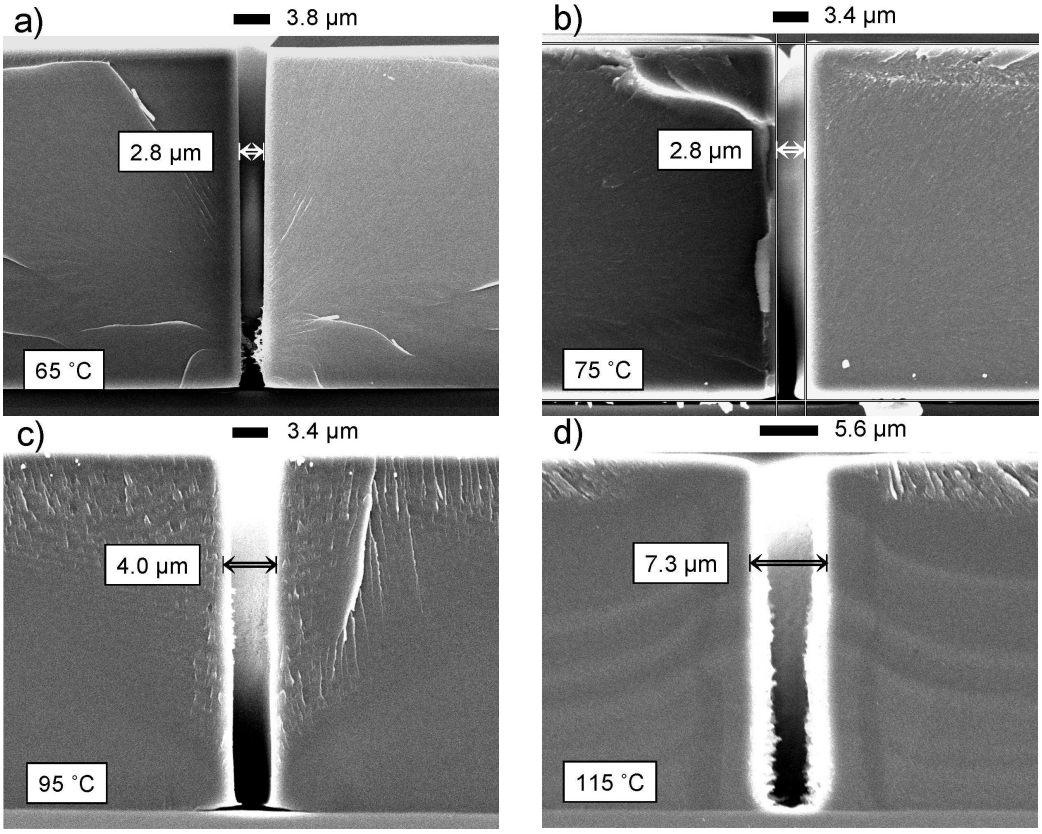

Figure 4.10: Cross-sectional scanning electron micrographs of the smallest fully resolved trench structure for the sample soft baked **a)** at 65 °C, **b)** at 75 °C, **c)** at 95 °C, and **d)** at 115 °C. The samples were cleaved from the trench monitor structure, and have been coated with gold in order to prevent charging. The size of the mask feature responsible for the trench is indicated by a black bar at the top of the trench. The actual width of the trench is indicated by the arrows.

solvent, monomer, or impurity molecules in the resist and forms a strong acid [41]. An increased solvent content may facilitate this process, thus increasing the effective concentration of the actual polymerization catalyst, in essence increasing the sensitivity of the resist. Both effects of the increased solvent concentration, in particular the latter, would result in a higher cross-link density and thus a stronger material.

4.6.2 Lithographic resolution

Figure 4.10 shows scanning electron micrographs of the narrowest, fully resolved trenches. The inspection confirms optical microscope inspection, showing the narrower trenches to be partially obstructed. Similar inspection of the ridge structures also confirms optical inspection, showing the narrower ridge structures to be failed, either by collapsed or wriggly ridges.

The sample soft baked at 65 °C, see Figure 4.10 a), shows smooth, near

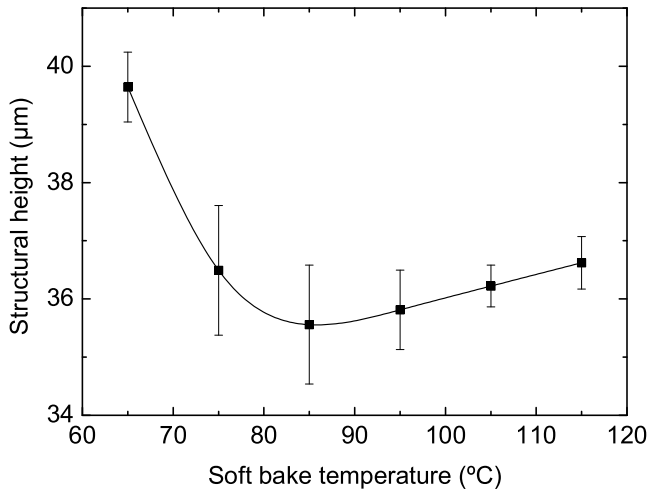

Figure 4.11: Structural height as a function of soft bake temperature. The error bars correspond to one standard deviation.

vertical sidewalls. The sample soft baked at 95 °C, Figure 4.10 c), shows slightly more sloped and rough sidewalls. It is seen in Figure 4.10 that the smallest resolved trench in the case of soft baking at 65 °C is narrower than in the case of a 95 °C soft bake. This is in contrast to the trench resolution established from optical inspection, i.e. the size of the mask feature responsible for the trench, which shows a resolution of 3.8 μm and 3.4 μm for soft baking at 65 °C and 95 °C, respectively. The samples soft baked at 65 °C and 75 °C are overexposed while the samples soft baked at 95 °C, 105 °C, and 115 °C are underexposed, confirming an increased sensitivity at low soft baking temperatures.

Figure 4.11 shows the measured height as a function of the soft bake temperature. The structural height initially decreases from a value of almost 40 μm at a soft bake temperature of 65 °C to slightly below 36 μm at 85 °C. At higher soft bake temperatures there is a slight increase in the structural height. Figure 4.12 shows the nominal aspect ratio of the narrowest, fully resolved trench and ridge structures, respectively. The nominal trench aspect ratio is initially constant at 10.5, but decreases at temperatures above 95 °C. The ridge aspect ratio is initially 8, then decreases towards a value of 4 at 105 °C, and finally increases slightly at 115 °C. Also included in Figure 4.12 is the actual trench aspect ratio, obtained from the actual width of the narrowest, fully resolved trenches, as measured in the SEM inspection. This shows an unambiguous decrease in trench aspect ratio with increasing soft bake temperature. At 85 °C the nominal and actual trench aspect ratio are equal. At this temperature the pattern transfer fidelity is 100 % for a dose of 225 mJ/cm^2.

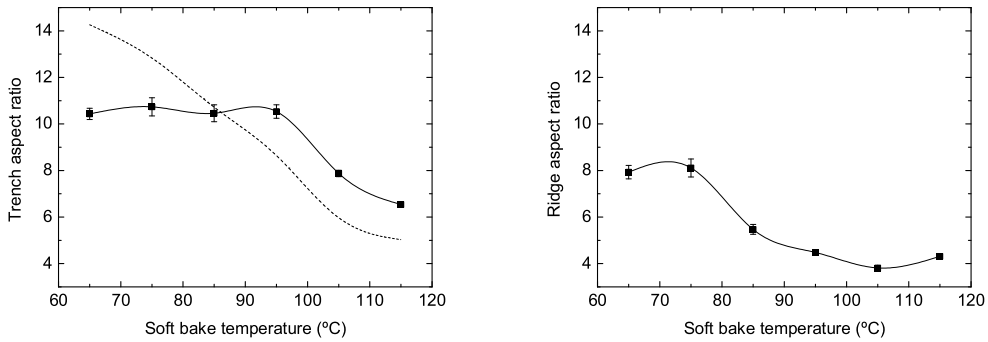

Figure 4.12: Nominal aspect ratio as a function of soft bake temperature for trench and ridge, respectively. The error bars correspond to one standard deviation. The actual trench aspect ratio, assessed through SEM inspection, is indicated by the dashed line.

While ridge resolution is affected by both line width and structural stability, as the surface tension of the evaporating solvent following development will tend to collapse the ridges [35], the trench resolution is equal to the minimum obtainable line width. The decrease in the nominal trench aspect ratio at elevated soft bake temperatures is best explained by a decrease in resist contrast at these temperatures. A decrease in contrast may be explained by thermal activation of the photo-acid generator during soft bake. The amount of released polymerization catalyst is not enough to fully polymerize the SU-8, but the resulting background cross-link density lowers the effective dose contrast between exposed and unexposed areas of the resist, and causes line broadening. The initial decrease in ridge aspect ratio suggests a decrease in the structural strength of the resist, possibly due to a decrease in the cross-link density as a result of decreasing sensitivity. The rate at which the cross-linked SU-8 deteriorates in the developer must be expected to increase with a decrease in cross-link density. This may explain the initial decrease in structural height. The increase in height at higher soft bake temperatures is consistent with an increase of cross-link density due to thermal PAG activation.

4.6.3 Cracking and hardness

In addition to the standard inspections, the strength of the cross-linked SU-8 was probed using an FM-700 micro-hardness tester (Future-Tech, Japan). The micro-hardness tester was operated in Vickers hardness mode, using a test load of 10 g and a load keeping time of five seconds. In order to avoid any influence from the substrate, the test load was selected to give a permanent indentation depth of approximately one tenth of the SU-8 thickness. The hardness of the SU-8 was tested in five different locations, separated by at

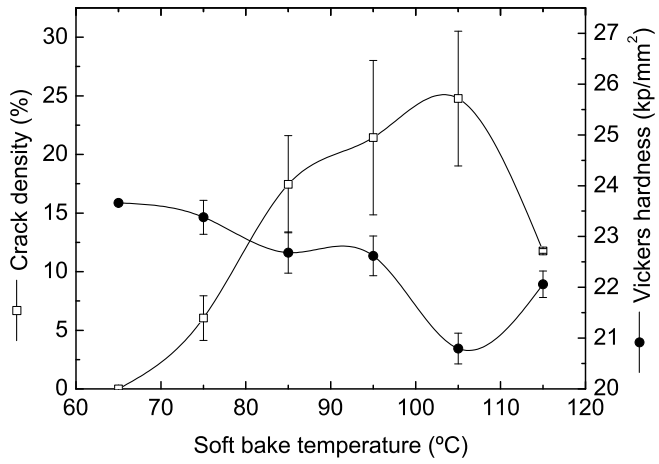

Figure 4.13: Crack density and Vickers hardness as a function of soft bake temperature. The error bars on the crack density represent the range of measurements, while those on the hardness correspond to one standard deviation.

least 100 μm while avoiding cracks, within the same five by five mm square structure as used in the cracking inspection.

In Figure 4.13 the result of the crack inspection and hardness measurements is presented. No cracks are observed in any of the structures on the sample soft baked at 65 °C. The crack density is thus set at 0 %. The crack density increases with increasing soft bake temperature up to 105 °C, then drops significantly. The hardness of the SU-8 decreases with increasing soft bake temperature, from a Vickers hardness number of almost 24 at 65 °C to below 21 at 105 °C. At a soft bake temperature of 115 °C the hardness increases to 22. A Vickers hardness number of 25 has previously been reported to be sufficient for SU-8 to be used as a master mould for PDMS soft lithography [16]. It is important to keep in mind that the Vickers method is only really suitable for quantitative characterization of samples with similar ductility, which is not necessarily true for these films. The method is thus not well suited for polymeric samples, and the measurements presented here only serve as a qualitative comparison of the samples.

As observed in Figure 4.13, the crack density increases with increasing soft bake temperature while the hardness decreases. The decrease in hardness suggests a decrease in cross-link density, again as a result of the degrading resist sensitivity. In the case of the crack density, a decreasing material strength would make the resist more prone to cracking. However, the driving force behind cracking is the residual stress in the polymerized structures. As all the samples were post-exposure baked at 65 °C, the stress induced during PEB due to thermal mismatch must be expected to be similar for all samples. The residual stress changes as a function of the stress in the

film at the point of polymerization, i.e. the level of stress induced during soft baking. For samples soft baked at low temperature, part of the induced stress can relax, owing to the high solvent content. The low crack density at low soft bake temperature can thus be explained by the combined effect of an intrinsically stronger material and a lower residual stress. At 115 °C the hardness increases, probably due to thermal PAG activation, causing the crack density to decrease. While this effect may continue to decrease the crack density at higher soft bake temperatures, the lithographic resolution would suffer, as indicated in Figure 4.12.

4.6.4 Conclusion

All of the observations made in the investigation of the effect of the soft bake temperature point towards degrading lithographic performance and material properties with increasing soft bake temperature. One must, however, keep in mind that while the optimal post-soft bake processing conditions must be expected to change with soft bake temperature, they were kept constant in this investigation.

The post-exposure bake temperature of 65 °C is best suited for samples soft baked at low temperature, for which a large part of the polymerization occurs at low temperature. Increasing the temperature in the post-exposure bake of samples soft baked at higher temperatures would cause the polymerization to progress further, increasing the cross-link density. The result would be an increase of the material strength, and thus an increase of the hardness and a decrease in the crack density. This would also increase the realizable ridge aspect ratio, while the realizable trench aspect ratio probably would decrease due to line broadening. The decrease in cracks and the increase in ridge aspect ratio is confirmed by the center runs in the second DOE, which show a maximum crack density of 10 %, and a ridge aspect ratio of 5.4. The trench aspect ratio, however, is at a slightly lower 10.2.

Increasing the PEB temperature in the case of a low soft bake temperature would lead to a higher level of residual stress and consequently to increased delamination risk, which is confirmed in the second DOE models.

Finally, the exposure dose was optimized for soft baking at 95 °C. At lower soft bake temperatures the higher sensitivity leads to overexposure, which may cause the trench resolution to degrade. Thus, a lower exposure dose at the low soft bake temperatures would be expected to improve the minimum line width. This was not confirmed by the investigation of the optimal process in section 4.5, most likely due to the fact that the SEM inspection was performed at the end of the trenches, rather than on a cross section.

Chapter 5

Device Fabrication

The fully developed and optimized process of SU-8 lithography is quite different from the process suggested by the manufacturer [14], in process parameters as well as in performance. This chapter presents the full fabrication process, from bare silicon substrate to individual chip ready for characterization. Figure 5.1 shows a flow chart of the fabrication process. The SU-8 process section is a short summary of the preceding chapters. The back-end processing section presents the packaging of the structures fabricated in the lithographic process. Finally some considerations concerning process turnround along with an investigation of the fabrication yield are presented.

5.1 SU-8 Processing

SU-8 processing consists of the steps of coating the resist onto the substrate, exposure and cure of the resist, and development of the structures. The process starts with a clean, dry substrate and results in structures of 40 μm high cross-linked SU-8 resolved on the substrate according to the pattern on the photolithographic mask.

The oxidized silicon substrates are transferred directly from the dehydration oven to the spin coater, where approximately 5 mL of SU-8 25 is deposited on the substrate. The thickness of the coating is defined in a spin at 1250 rpm for 30 seconds. The wafer is transferred onto a hotplate and baked at 50 °C for ten minutes in order to reduce the solvent level in the resist. This enables edge bead removal, which is carried out on the spin coater. A flow of PGMEA is applied through a needle positioned approximately five millimeters from the edge of the wafer. The solvent is applied for 40 seconds while the wafer spins at 500 rpm. After the edge bead is dissolved, the wafer is spun at 1440 rpm for 28 seconds. The final step of the resist coating procedure is the soft bake. The wafer is placed on a hotplate, ramped to 65 °C in six minutes, and baked for five minutes. The soft bake is concluded by cooling to room temperature over a period of an hour and a half.

The soft baked substrate is exposed to near-UV light (365 nm) through a photolithographic mask. The mask aligner is operated in hard contact

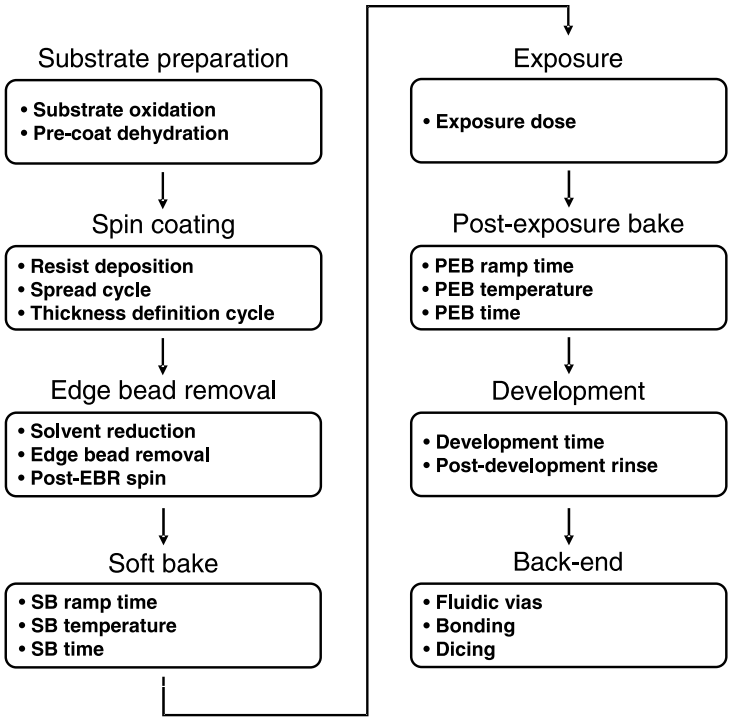

Figure 5.1: Process flow chart illustrating the steps and parameters involved in the fabrication of SU-8 devices.

mode, and the exposure dose is applied in a single exposure of 180 mJ/cm^2 (20 s at 9 mW/cm^2). The exposure generates an acid in the exposed areas, which initiates cross-linking of the SU-8 molecules. The cross-linking process is assisted by thermal energy in the post-exposure bake. The exposed wafer is transferred to a cold hotplate and ramped to 65 °C in six minutes. The wafer is baked for 30 minutes, and cooled to room temperature over a period of an hour and a half.

In the development the un-exposed areas of SU-8 are dissolved in PGMEA. The post-exposure baked wafer is immersed in agitated PGMEA in two steps. A three minute dip in a coarse developer bath is followed by a two minute dip in a cleaner, so-called final developer bath. The development is finished by a rinse in fresh IPA, whereafter the wafer is dried.

This procedure produces crack-free structures of 40 μm high SU-8 on the substrate. The pattern transfer fidelity is close to 100 % and process is capable of resolving trenches with aspect ratios in excess of 11. Grating-like ridges are stable up to an aspect ratio of almost 9.

5.2 Back-end Processing

When the design has been transferred to the SU-8 in the photolithographic process, the device must be packaged before the performance of the device can be tested outside the cleanroom. The waveguides and other optical struc-

tures are fully functional without the packaging, but the structures must be protected from the environment outside the cleanroom. Particles, as well as water or other chemicals, may cause the performance of the optical structures to deteriorate. Furthermore, if the device comprises a fluidic system, the channels must be sealed with a lid. Also, access to the optical system as well as the fluidic system must be enabled. Once sealed, the individual chips on the wafer must be separated from each other.

Packaging of the chips is realized through waferscale bonding of a glass lid on top of the SU-8 structures. The bond between the SU-8 and the lid is mediated by a layer of polymetamethylacrylate (PMMA) in an adhesive bonding process developed by Bilenberg *et al.* [6]. The PMMA layer simultaneously becomes the top cladding of the waveguiding structures (the refractive index of PMMA is 1.49 at 633 nm compared to 1.60 for SU-8 at the same wavelength). The connection from the macroscopic world to the chip is made through the optical and fluidic interconnections. Optical interconnection is realized through butt-coupling of optical fibers to waveguides which end in a facet on the side of the chip. These facets are made in the same dicing procedure that separates the individual chip from the rest of the wafer. Fluidic interconnection is made possible through the fluidic vias which connect the fluidic system made up by the SU-8 structures to the backside of the chip. The fluidic vias are made by powder blasting a hole through the silicon substrate, and they must be made before the chips are sealed in the bonding process. The method of realizing fluidic interconnection is described below. The chips are diced out using a saw with a diamond blade. In a last step, the chips are evacuated in order to remove the possible traces of water which was used a coolant in the dicing process.

5.2.1 Fluidic vias

Though the powder blasting process itself is a very simple process, which takes only ten seconds per hole, there is a lot of preparation and subsequent cleaning involved in the process. In fact, the process is so labor intensive that it consumes approximately 40 % of the man-hours involved in the fabrication process. The powder blasting method was identified and developed by Peter M. Moselund, who was a Master's student in the InSERS group in 2005, on the basis of a procedure developed by Asger Vig Larsen at MIC.

Powder blasting is the process by which a high speed stream of particles of e.g. glass or corundum (Al_2O_3) propelled by compressed air is used to polish or shape a surface. A hard and brittle material such as silicon is eroded so fast the technique can be used to blast holes through the substrate. A layer of Nitto STW 20 blue tape (usually used for back side protection during wet etching, and in mounting for dicing) is used to mask the wafer from the attack of the blast. The particles have little or no effect on the soft tape and simply bounce off. This tape, however, can not be applied directly onto the SU-8 structures, as the adhesive force of the tape will lift small structures

when it is removed. A protective coating must therefore be applied in the form of a 25 μm layer of AZ 4562 photoresist, which is spin coated onto the substrates prior to the blue tape masking. This coating has the added effect of protecting the structures from contamination from the blasting process. The blue tape is applied to the front as well as to the back of the wafer.

The apertures in the masking layer are made using a CO_2 laser system. As the focussed laser beam moves over the wafer (in a pattern predefined in the control software) the blue tape and the AZ resist absorb the energy and burn. As silicon is transparent to the infrared radiation of the CO_2 laser (10.6 μm), the blue tape on the backside also burns. Circular, 1.2 mm holes are defined in the masking layer using a beam power of approximately 6 W and a writing speed of 300 mm/s. The holes are blasted through the substrate from the backside using 110 μm corundum particles. This results in holes with an approximate diameter of 0.8 mm.

The powder blasting is a messy process, which leaves the wafers covered in particles. They must be cleaned before any further processing can take place. The masking tape is rinsed in deionized water and removed, and the wafer is rinsed in deionized water. Transferred to the cleanroom lock, the wafer is rinsed in a sonicated bath of deionized water for ten minutes. A drop of Triton X-100 soap is added for the last two minutes. After a final rinse in deionized water, the wafer is dried using cleanroom tissue and a nitrogen-gun. The wafer is now free from any particles from the blasting process, but the structures are still covered in the protective AZ coating. The resist is stripped using PGMEA. The wafer is immersed in PGMEA for two minutes, which dissolves most of the resist. A second dip in fresh PGMEA for 45 seconds ensures even the burnt resist is removed. The strip is finished by a rinse with IPA from a wash bottle, whereafter the wafer is dried.

5.2.2 Bonding

The adhesive PMMA bonding process used to bond the lid on top of the SU-8 structures was developed by Bilenberg *et al.* as an alternative to bonding with SU-8 as the intermediate layer [6]. A bond strength of 16 MPa is reported, which is slightly higher than the bond strength observed for bonding with SU-8 as the intermediate layer. The propagation loss of waveguides with PMMA top-cladding is reduced by more than 5 dB/cm compared to waveguides with SU-8 top-cladding. Some parameters in the bonding procedure have been changed during this projet, but the procedure is in essence the same as the original process.

Before the actual bonding, the lids must be coated with PMMA. Borofloat glass wafers are used as lids. The glass wafers are cleaned (depending on the supplier, this may not be necessary) and dehydrated in a convection oven at 250 °C for 18 hours. The PMMA is coated onto the lid using a spin coater. The PMMA used is 13 % by weight of 950 kDa PMMA dissolved in anisole. A volume of approximately 4 ml is deposited in the center of the

wafer, which is spun at 1000 rpm for 60 seconds. The wafer is subsequently baked on a preheated hotplate at 150 °C for ten minutes. This produces an approximately 6 μm coating of PMMA on the lid.

The lid is bonded onto the substrate with the SU-8 structures using an anodic bonder with nano-imprint capabilities. The machine is in essence two hotplates which can be pressed together with a specified force. The bonding stack is loaded into the machine upside down, such that the borofloat lid is closest to the bottom hotplate. The bonding chamber is pumped and purged with nitrogen in order to remove oxygen from the bonding ambient. Both hotplates are ramped to 140 °C in 15 minutes. When the setpoint is reached, the chamber is evacuated, and the temperature is stabilized for five minutes. The two hotplates are then pressed together with a force of 2200 N and the stack is bonded for 20 minutes. At this point the chamber pressure is raised to approximately 50 mBar and the hotplates are cooled to 100 °C at a rate of 3 °C/min, still with the bonding pressure applied. Now that the temperature is below the glass transition temperature of the PMMA (105 °C [6]), the chamber pressure is raised further to approximately 250 mBar, and the hotplates are cooled (unfortunately still only at approximately 3 °C/min due to machine limitations) to a temperature below 70 °C where the bonding pressure is removed and the hotplates are separated. The stack is removed from the machine and allowed to cool to room temperature, and the bonding procedure is complete.

5.2.3 Dicing

The last step in the fabrication procedure is the separation of the individual chips on the wafer. The dicing procedure is performed on a dicing saw developed for the semiconductor manufacturing industry. The wafer is mounted silicon side down on a frame using blue tape, placed on the vacuum chuck, and aligned. A blade containing diamond particles (or another abrasive) spinning at high speed cuts through the lid, the PMMA bonding layer, the SU-8 structures, and the silicon substrate in a single pass. The blade is cooled with in a stream of deionized water, and cutting debris is removed by a jet of deionized water.

The parameters used in the dicing procedure are a spindle rotation of 30000 rpm and a feed rate of 0.5 mm/s. The cut depth is adjusted to leave $100 - 150$ μm of the silicon substrate uncut. The low feed rate is used because the input and output facets of the optical system are made in the same cut that separates the chip from the wafer. A high quality of these facets is crucial in the characterization of the device. A low feed rate at a high rotational speed ensures a low surface roughness of the face due to a high number of passes of the blade during the cut of the waveguide. A high feed rate could also increase blade wear, which may influence the quality of the facets made in the next cut, and thus the reproducibility of the process. No investigation of the effect of the cutting parameters has been conducted,

as the result of using the above mentioned settings is satisfactory. When the dicing procedure is concluded the mounting frame is removed from the dicing saw, and the wafer is cut from the frame leaving the blue tape on the backside.

In the dicing procedure the chip is exposed to a substantial amount of water. If some of this water enters the chip and remains there, it would cause the performance of the optical system to deteriorate. The presence of water alters the condition of total internal reflection in the waveguiding material in the plane parallel to the substrate, which would cause the spectrometer loss to increase. In order to prevent water from entering, the chips are designed with a dike, in the form of a 20 μm wide wall, enclosing the entire chip. Any water present in the chip is removed by evacuating the diced wafer for 10 hours in a standard laboratory desiccator (at a pressure of $100 - 200$ mBar).

As an added bonus, the evacuation step provides an easy way of checking the fluidic system for leaks. Since the blue tape is left on the backside of the chip after the dicing procedure, the fluidic vias are covered during the evacuation. This means there initially is a higher pressure in the fluidic channel than in the desiccator. This pressure difference is partially equalized by diffusion through the blue tape during the evacuation. When the vacuum is removed at the end of the evacuation, there will be a low vacuum in the channel, provided the channel has been properly sealed by the bond. For the first few hours after the evacuation, it is thus possible to identify leaky channels by the absence of a depression of the blue tape over the fluidic vias.

5.2.4 Optical and fluidic interconnections

The optical system on the chip is accessed through optical fibers which are butt-coupled to the waveguides on the chip. The fibers used are multimode, step index fibers with a core diameter of 50 μm and 0.22 numerical aperture. In one end the fiber is cleaved to provide a clean, smooth facet, fixed in a custom-made holder on an xyz stage, and coupled to the waveguide facet on the chip by micromanipulation under a microscope. The other end of the fiber is coupled to other equipment using standard SMA connectors. Coupling efficiency can be increased using an index-matching medium, in the form of a gel with a refractive index similar to waveguide and fiber placed between the two facets. However, this gel was observed to creep into the chip along the waveguide surfaces, and the use of index-matching gel was abandoned.

In the cases where a fluidic system forms part of the device, fluidic interconnection is mediated through a custom-made chuck. A recess fitting the chip is milled in a block of a material such as aluminum, PMMA, or polycarbonate. At the positions of each fluidic via, a recess is made to accommodate an o-ring. The chip is held in place by one or two clamps, which press the chip against the o-rings as the clamps are fastened to the chuck by screws. Channels machined in the bulk of the chuck connect the fluidic vias to the side of the chuck, where the connection to other equipment is made using

Table 5.1: Turnround for the fabrication of a batch consisting of eight wafers. The turnround for the sub-processes are given as percentages of the total time.

	Process	Staff	Cleanroom	
Total	58.7	26.0	21.8	hours
Front-end	26	36	43	%
Fluidic vias	21	42	35	%
Bonding	23	19	22	%
Dicing	30	4	0	%

standard HPLC connectors and tubing [42].

5.3 Turnround and Yield

The batch size of choice for the final fabrication process is eight wafers. This size makes front-end processing, i.e. the SU-8 lithography, possible in one, slightly long day (excluding preparations and inspection). The total process time is almost 60 hours, and the fabrication can be finished in eight full working days. Less than half of the total process time requires the attention of the operator. Table 5.1 gives the process, staff, and cleanroom hours required for an eight wafer batch. Cleanroom hours are the number of staffed hours in the cleanroom, which is of interest since the user is billed not only for equipment use, but also for the number of hours spent inside the cleanroom. The process time of the sub-processes are also listed. The total process time is seen to be approximately equally divided between the four sub-processes. The process of making the fluidic vias takes up the biggest part of the staff hours, while the dicing process requires the least staff hours. Not surprisingly, the front-end processes consume the largest part of the cleanroom hours.

If a device was to be fabricated in a more production-like manner, the batch size should be larger. Due to maximum batch size limitations in the fabrication process (imposed by equipment or operator limitations), the optimum batch size is 20. A batch of this size would require four hotplates and two masks. The fabrication time is 100 hours. An estimate of the fabrication cost of such a batch was made. Assuming 16 devices per wafer, and one in five wafers subjected to inspection, the price comes to approximately 170 DKKR (30 US$) per device. This does not include consumables, such as substrates, masks, and resist. If production is based on six inch wafers, 44 devices may be fabricated per wafer, and the price drops to 63 DKKR (11 US$) per device.

In conjunction with a stay at the Division of Solid State Physics at Lund University in 2006, a series of at least 100 chips were needed for use in the laboratory in Lund. This presented an opportunity to investigate the yield of the fabrication of chips comprising of a simple fluidic system with an

integrated optical system. Twelve wafers with 16 chips each were processed in three batches, using the lithographic process described in section 5.1 with an exposure dose of 135 mJ/cm^2. Of these twelve wafers, eight were back-end processed to finish the fabrication process. All eight wafers survived the processing, so the wafer yield is 100 %. The process step most likely to cause failure to an entire wafer is the laser marking of the mask apertures for the powder blasting of fluidic vias. This process lacks proper alignment between the chuck and the laser control software, and successful alignment requires a steady hand and a fair portion of luck.

The fabricated wafers were inspected for water in the chips immediately after the dice, and for leaking channels after the desiccation. Water in a chip indicates a partially failed bond, but as the water is removed in the evacuation process, this is not considered catastrophic failure. A leaking channel, on the other hand is a catastrophic failure. Of the 128 chips fabricated, water was present in 26 after the dice. However, only nine chips showed clear signs of leaking channels after evacuation. The most likely cause of these bond failures is the influence of the PGMEA used in the edge bead removal process. It has been observed that irregularities are produced in the coating due to droplets of solvent which end up in the central part of the wafer. This local addition of solvent creates a crater-like disturbance of macroscopic size in the resist surface. The profile of such "EBR spatter" has not been characterized, but the phenomenon is observed to disturb the bonding procedure. The presence of particles, be it dust or lifted structures from the substrate, also disturb bonding, typically creating an area with no bond around the particle.

In addition to the nine leaking chips, three were destroyed in the dicing procedure due to blade failure. In one case, the optical system was observed to be damaged, most likely due to the presence of a particle during exposure. No attempts were made to systematically check the optical system for failure, but none of the 18 chips eventually used in the laboratory showed any signs of failure in the optical system. This brings the number of failed chips to 13 out of the total 128 chips, corresponding to a chip yield of 90 %. The chip yield of the individual wafers range between 63 % and 100 %.

Chapter 6

Device Performance

Optical components fabricated using the procedures outlined in the preceding chapter are only partially characterized by the performance of the photolithographic process. A fabricated device must be characterized in order to compare the performance to expectations based on design parameters, theoretical considerations, or application specific demands. Since the process optimization was based on the lithographic performance, it is necessary to characterize the performance of the fabricated spectrometers in order to verify the improved grating definition predicted by the increased lithographic resolution.

This chapter presents the performance of optical components fabricated in SU-8. The main emphasis is on the propagation loss of waveguides, and the transmission loss of spectrometers based on concave reflection gratings. The propagation loss of the waveguides has been measured to be as low as 0.3 dB/cm in the $785 - 885$ nm wavelength range, which is an improvement compared to the value of 0.8 dB/cm at 850 nm reported for SU-8 waveguides in the literature [4]. The characterization of the fabricated spectrometers show that a transmission loss of 13.1 dB is obtainable. Of the 13.1 dB transmission loss, only 3.3 dB can be attributed to the fabrication process. The effect of the process optimization on the spectrometer loss is estimated to be 7.5 dB.

6.1 The Optical Characterization Set-up

Figure 6.1 shows a sketch of the optical characterization set-up. The light source (a broadband HL-6000-S halogen lamp source from Avantes) is connected to the input fiber through a beam splitter. The beam splitter makes it possible to couple a HeNe-laser into the input fiber without changing any connections in the set-up. The intense visible laser light facilitates alignment of the device. Neutral density filters may be inserted in the optical path at the beam splitter before the source light is coupled into the the input fiber. The optical connection to the device under test is mediated through the input and output fibers, which are butt-coupled to waveguide end-facets. The

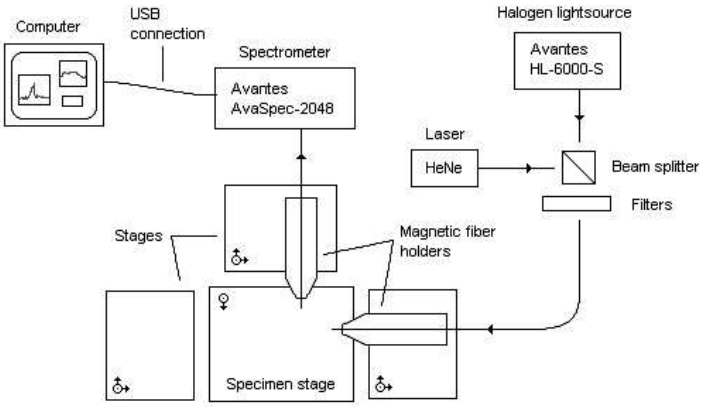

Figure 6.1: A sketch of the set-up used in the optical characterization of the devices.

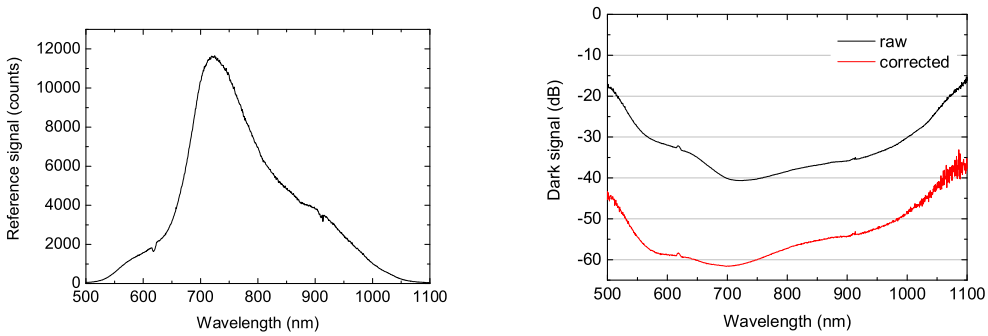

Figure 6.2: Reference spectra used in the device characterization. The left hand graph shows a raw reference signal in counts. The right hand graph shows the dark response with the left hand signal used as reference, and an example of a dark response corrected for filter and acquisition time.

fibers are step-index, multimode glass fibers (type ASF50 supplied by Thorlabs) with a core diameter of 50 μm and a numerical aperture of 0.22 which are fitted with standard SMA connectors for connection to the optical equipment. The output fiber is connected directly to the read-out spectrometer (AvaSpec-2048, Avantes).

The data recorded by the read-out spectrometer are processed and logged in a LabWIEW virtual instrument, which was developed as a part of this Ph.D. project. The virtual instrument enables on-line monitoring of insertion loss, as well as correction for spectrometer acquisition time and filters. The recorded data are converted into transmission data using a reference signal which must be recorded prior to the insertion of the device under test. This facilitates subsequent data analysis. Being able to adjust the acquisition time, and change the filters in the set-up results in better signal-to-noise ratio, and provides a larger dynamic range. Figure 6.2 shows a reference

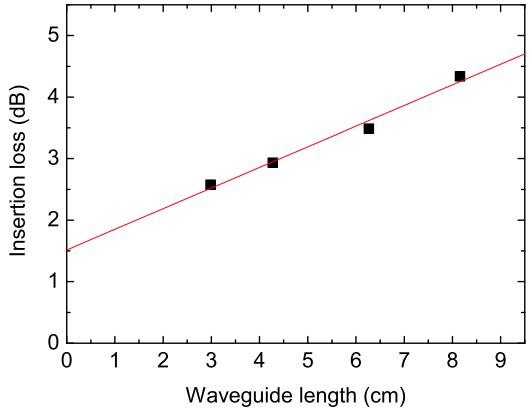

Figure 6.3: Insertion loss as a function of waveguide length. The line is a linear fit to the data points. The propagation loss is given by the slope of the line, which is 0.34 ± 0.03 dB/cm. The coupling loss is equal to the intercept, which is 1.51 ± 0.17 dB.

spectrum recorded with the input fiber coupled directly to the output fiber. The figure also shows how the dynamic range is wavelength dependent due to the wavelength dependent intensity of the source, and how the limited dynamic range of the read-out spectrometer is expanded by changing the filters in the set-up.

6.2 Waveguides

An important waveguide property is how much the intensity of light propagating in the waveguide is attenuated. The propagation loss is the amount of light lost (be it due to scattering or absorption) per unit length of waveguide. Propagation loss is determined by measuring the insertion loss of different lengths of waveguide. The test mask made for process optimization also contains waveguides designed for propagation loss measurements. The layout consists of a series of waveguides in groups of five, with lengths around 1.5 cm, 2.6 cm, 3.0 cm, 4.2 cm, 6.3 cm, and 8.1 cm. The propagation loss is determined by measuring the insertion loss of these waveguides. Such measurements can never underestimate the insertion loss, so a easy way of omitting the errors imposed by variations in the quality of the waveguide input and output facets is by selecting the best measurement in each group. If a group shows excessive loss compared to the other groups, it is also omitted in the analysis. A linear regression of the insertion loss as a function of waveguide length yields the propagation loss as the slope, and the coupling loss as the offset, as shown in Figure 6.3.

The propagation loss of 40 μm by 40 μm SU-8 waveguides fabricated using the standard baking temperature of 95 °C in the lithographic process is presented in Figure 6.4. The propagation loss is 1.2 dB/cm at 633 nm and 0.3 dB/cm at 850 nm. For comparison Mogensen *et al.* report a propagation

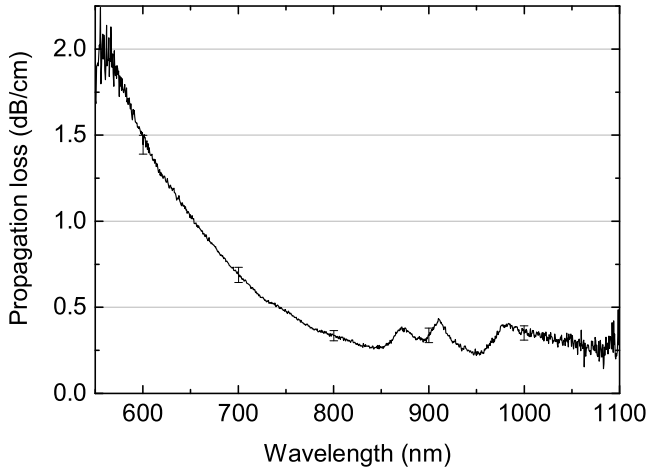

Figure 6.4: Propagation loss for waveguides fabricated using the standard baking temperature of 95 °C. The exposure dose is 225 mJ/cm^2.

loss of 1.4 dB/cm at 633 nm and 0.8 dB/cm at 850 nm for 100 μm high, 30 μm wide SU-8 waveguides with PDMS top cladding [4].

6.2.1 The influence of processing conditions

After the process optimization, the performance of the waveguides was measured in order to determine the effect of the process optimization. As an increase in propagation loss was observed, a series of waveguides fabricated using different exposure doses were measured in an effort to find an explanation to the change brought on by the process optimization.

Figure 6.5 shows the propagation loss before and after the second design of experiment. The propagation loss is observed to be increased to a value approximately twice as large after the process optimization. The observed increase in coupling loss is due to the fact that no index-matching gel was used in the post-DOE2 measurements. This gel was observed to creep into the chip along the waveguide surfaces making remeasurements impossible, so the use of index-matching gel was abandoned.

Figure 6.6 shows the propagation loss of waveguides fabricated after the second DOE using varying exposure dose. While the propagation loss is approximately equal for waveguides processed using 270 mJ/cm^2 and 180 mJ/cm^2 exposure doses, the propagation loss increases significantly at 90 mJ/cm^2. The variations in the coupling loss are ascribed to variations in the quality of the waveguide facets.

It has not been possible to find a conclusive explanation to the observed changes in propagation loss. The effect of the process optimization on the propagation loss is not detrimental to the use of such waveguides in lab-

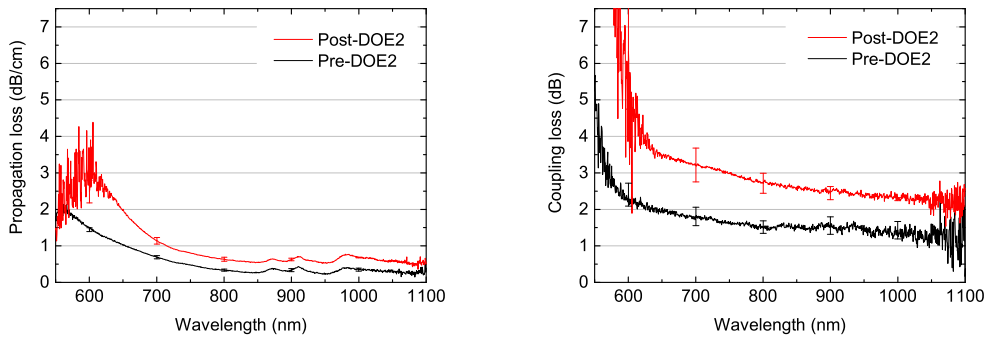

Figure 6.5: Propagation loss and coupling loss for waveguides fabricated before and after the second DOE. In each case, the exposure dose is the optimal dose (225 mJ/cm^2 pre-DOE2 and 180 mJ/cm^2 post-DOE2). The propagation loss is observed to increase as a result of the process optimization. The increase in coupling loss is due to the fact that no index-matching gel was used in the post-DOE2 measurements.

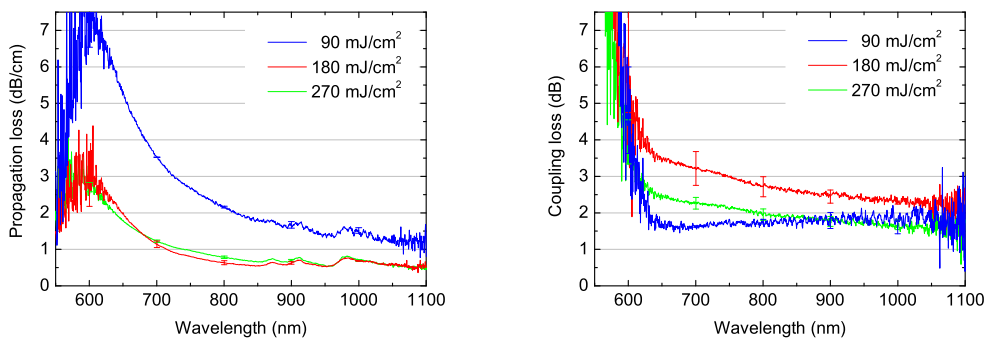

Figure 6.6: Propagation loss and coupling loss for waveguides fabricated according to the optimized process (post-DOE2) using different exposure doses. The propagation loss increases significantly at low exposure dose. The variations in the coupling loss is be ascribed to variations in the quality of the waveguide facets.

on-a-chip systems, and the increased propagation loss is counteracted by the positive effect of the increased lithographic precision on the performance of the integrated spectrometers (presented in section 6.3). Two possible explanations to the changes in propagation loss have been investigated:

- Non-activated photoinitiator.
- Sidewall roughness and/or material inhomogeneity.

Since the exposure dose in the optimized process recipe is lower than the dose used in the non-optimized process, the increase in propagation loss could be due to increased absorption at lower wavelengths, brought on by photoinitiator which has not been activated in the exposure process. If this were the case a decrease in propagation loss should be observed when the exposure dose in increased in the optimized process. As this is not the case (cf. Figure 6.6), this effect can not explain the increased propagation loss induced by the process optimization. It may, however, explain the increase at low exposure dose in the optimized process.

The increased sensitivity of SU-8 in the optimized process is partly caused by faster polymerization kinetics due to the increased solvent content at low temperature soft baking. If the polymerization is very fast and effective, the catalytic acid from the photoinitiator may be trapped inside a highly cross-linked area, in effect terminated by the sudden increase of diffusion rate in the cross-linked SU-8. If this were the case, the cross-link density could vary throughout the SU-8, which would introduce inhomogeneities in the refractive index of the waveguide. This effect would also lead to increased surface roughness, due to local variations in the rate of deterioration in the development process. According to Ladouceur, the main effect of both surface roughness and bulk inhomogeneity is to induce scattering loss [43].

In an attempt to quantify the scattering loss of the fabricated waveguides, the 90 mJ/cm^2 and the 180 mJ/cm^2 samples from the investigation of the effect of the exposure dose were characterized using HeNe-laser light at 633 nm. An increase in propagation loss of 4 dB/cm should be clearly visible if the increase is due to scattering, even to the naked eye. These observations are somewhat disturbed by the glass lid bonded on top of the waveguides, but there seemed to be no significant difference in the intensity of the light emitted from the waveguides. Measurements of the crosstalk to neighboring waveguides showed a crosstalk suppression of more than 25 dB, but no difference in crosstalk suppression between the first and the second neighboring waveguide was observed.

6.3 Spectrometers

From the point of view of process optimization, the primary characteristic of the fabricated spectrometers is the transmission loss (cf. section 1.1). When the fabricated spectrometers are characterized, the transmission through the

spectrometer is measured as a function of wavelength. The read-out spectrometer connected to the output of the spectrometer under test records the transmission in terms of free space wavelength. The wavelength of light propagating in a waveguide λ^* is given by the free space wavelength λ as

$$\lambda^* = \frac{\lambda}{n_{eff}(\lambda)} \tag{6.1}$$

where n_{eff} is the effective refractive index of the waveguide. The effective refractive index of a waveguide depends on the difference in refractive index between the core material and the cladding material, and has a value somewhere in between the refractive index of the two. Since the index contrast in the waveguiding system in question is at least 0.1, the effective index of the waveguide may be approximated by the refractive index of the core material, i.e. $n_{\mathrm{SU-8}}$ (given by equation (1.5) in section 1.2).

If the position of a diffraction peak associated with diffraction order m is denoted λ_m, equation (1.2) relates the peak positions of two adjacent diffraction orders by

$$m\lambda_m^* = (m-1)\lambda_{m-1}^* \tag{6.2}$$

It is seen that a lower order diffracts at a higher wavelength. The free spectral range of diffraction order m is given by equation (1.3) as

$$FSR_m = \lambda_{m-1} - \lambda_m \tag{6.3}$$

In order to be able to compare the theoretical free spectral range given in equation (1.4) to the one observed in the transmission spectrum, the order of the different diffraction peaks must be identified. Equation (6.2) may be rearranged to give

$$m = \frac{\lambda_{m-1}^*}{\lambda_{m-1}^* - \lambda_m^*} \tag{6.4}$$

The diffraction order of a peak is thus identified by the position of the peak and the position of its neighboring, lower order peak. It is also possible to identify the order by the position of the neighboring, higher order peak, in which case one gets

$$m = \frac{\lambda_{m+1}^*}{\lambda_m^* - \lambda_{m+1}^*} \tag{6.5}$$

Figure 6.7 shows an example of a transmission measurement. The measured spectrometer has design order $m_0 = 9$, design wavelength $\lambda_0 = 730$ nm, a focal length of 9.5 mm, and a linear dispersion of 7.5 μm/nm. The spectrum is obtained by coupling the broad band light source ($500 - 1100$ nm) to the central input waveguide, and recording the transmission to the central output waveguide using the read-out spectrometer. Using equation (6.4) it is verified that the diffraction peak at 726 nm corresponds to the design order. From the position of the neighboring, lower order peak at 815 nm, a free spectral range of 89.2 nm is obtained using equation (6.3). This compares very well with the design value of 91.3 nm given by equation (1.4).

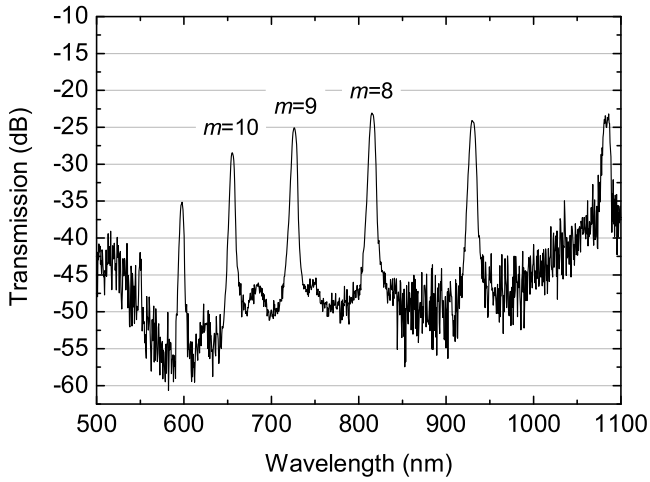

Figure 6.7: Transmission spectrum of a spectrometer with design order 9, design wavelength 730 nm, and a linear dispersion of 7.5 μm/nm. The spectrometer is fabricated prior to the process optimization using an exposure dose of 270 mJ/cm^2. The spectrum shows the transmission of a broad band signal from the central input to the central output. The peak at 726 nm corresponds to the design order.

The shift in the design order peak between different outputs gives a linear dispersion of 7.5 ± 0.2 μm/nm. The spectrometer characteristics correspond almost perfectly to the design parameters, a feature which is also observed in spectrometers with different design parameters [9].

6.3.1 Contributions to the transmission loss

The transmission loss of a spectrometer has contributions from different sources:

- *Intrinsic grating loss.*
  Calculated to approximately 2.5 dB.

- *Loss due to power distribution among several orders.*
  Measured to approximately 4.4 dB

- *Coupling and propagation loss.*
  Typically amounts to approximately 3 dB.

- *Loss due to tapering of the input waveguide.*
  Measurements show that narrowing the width of the input slit from 30 μm to 11 μm introduces a loss penalty of approximately 2.3 dB at 880 nm.

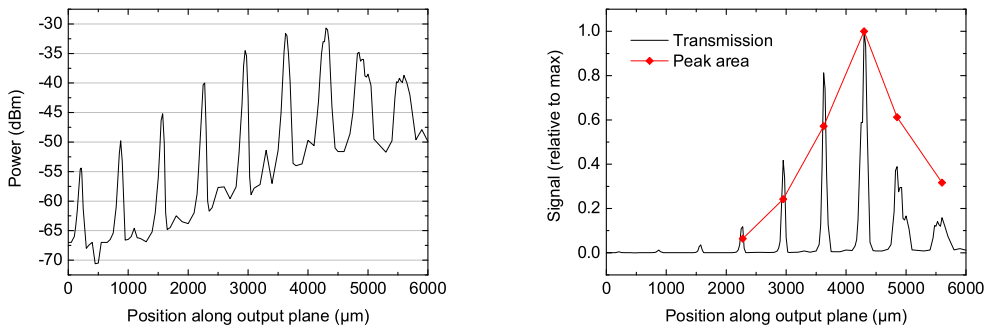

Figure 6.8: The output power along the output plane of a spectrometer with design order 9 and design wavelength 730 nm. The measurement is obtained by launching light with a wavelength of 633 nm into the input and measuring the output power with the output fiber coupled directly to the output facet (i.e. no output waveguides). The graph on the left shows the raw data as recorded by the powermeter. The graph on the right shows the output signal and the peak area relative to the peak with the highest transmission. From the peak areas of the different diffraction orders, the effect of power distribution among several orders is estimated to 4.4 dB.

The remaining loss must be attributed to non-perfect grating fabrication, i.e. the limited performance of the photolithographic process. The details behind the estimates of each contribution are given below.

Even a perfectly fabricated grating will give rise to loss due to the fact that one grating facet shadows part of the neighboring facet. The contribution to the transmission loss from the grating itself has been estimated by assuming the shadowing effect of a neighboring grating facet simply decreases the effective facet area. Calculations using scalar diffraction theory yield a grating loss of approximately 2.5 dB [9].

Since the grating is not blazed, part of the transmission loss stems from the distribution of the input power over several orders. The effect of power distribution among different diffraction orders is assessed through a measurement of one of the fabricated spectrometers. The transmission of a spectrometer was measured using quasi-monochromatic HeNe-laser light at 633 nm as the input signal. The spectrometer was designed with no output waveguide array, so the output fiber was coupled directly to the output facet at the output focal plane. The output power was recorded as a function of position along the output facet using a powermeter. The result of the measurement is seen in Figure 6.8. The power coupled into each diffraction order is estimated from the area under each diffraction peak. Using the relative peak area of the two neighboring orders on either side of the order with lowest transmission loss (also indicated in Figure 6.8), the contribution to the spectrometer transmission loss from the distribution of input power among different diffraction orders is estimated to be 4.4 dB.

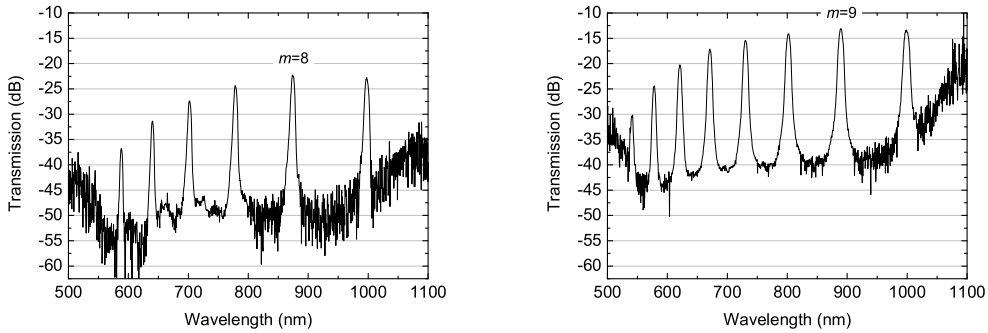

Figure 6.9: Transmission spectra of spectrometers with design order 9 and design wavelength 730 nm. The spectrometer measured in the left hand graph was fabricated before the process optimization, while the right hand graph was obtained for a spectrometer fabricated using the optimized fabrication process. The measurements differ not only in the fabrication process, but also in the width of the input slit used in the characterization. The decrease in transmission loss due to the process optimization is estimated to 7.5 dB.

Part of the transmission loss can be explained by the coupling loss between the fibers and the input and output waveguides, and the propagation loss through waveguides and the spectrometer slab. This contribution is a function of wavelength, but also varies with the fabrication process parameters, as presented in the preceding section. The optical path through a spectrometer is measured from the input facet though the input waveguide, through the spectrometer slab via the grating to the output, and finally through the output waveguide to the output facet. The spectrometers presented here are all designed using a focal length of 9.5 mm, and have an optical path length from input facet to output facet of 2.35 cm.

The resolving power of a spectrometer is affected by the width of the input slit. The input waveguides are tapered in order to narrow the width of the input slit below 40 μm. The contribution to the transmission loss due to tapering of the input waveguide depends heavily on the tapering angle. Since the taper length is fixed at 3 mm in the spectrometer design, this translates into the width of the input slit. The narrower the slit, the greater the loss penalty. As for the coupling and propagation loss, this contribution is a function of wavelength. Measurements of a spectrometer using two different inputs and the same output show a increase in transmission when the input slit is changed from 11 μm to 30 μm. The increase varies from 4 dB at 675 nm to 2 dB at 950 nm. At 880 nm the increase is estimated to 2.3 dB, a value which will come in handy in the analysis of the effect of the process optimization on the spectrometer performance.

6.3.2 Spectrometer performance

The transmission spectra of spectrometers fabricated before and after the process optimization are presented in Figure 6.9. The left hand side of Figure 6.9 shows the spectrometer performance before the process optimization. The measurement shows a transmission loss of 22.3 dB at 874 nm for the diffraction peak corresponding to $m = 8$. The region between the diffraction peaks show signs of secondary peaks, probably originating from secondary structures in the grating produced in the photolithographic definition. Nevertheless, the design order peak rises approximately 20 dB above the noise floor. Measured at $\Delta\lambda = 10$ nm the crosstalk suppression is 19.2 dB.

Spectrometer performance after the process optimization is shown in the right hand side of Figure 6.9. The transmission loss is 13.1 dB at 889 nm for the diffraction peak corresponding to the design order $m = 9$. The signal-to-noise ratio is 25 dB. Measured over four different outputs, the transmission loss varies from 14.2 dB to 13.1 dB in the wavelength range $784 - 889$ nm. Some of this variation in the transmission loss is due to variations in the SU-8 absorption in this wavelength range. The variation in transmission loss drops from 1.1 dB to 0.7 dB when the transmission is corrected for SU-8 absorption using the transmission spectrum of an adjacent waveguide. Measured at $\Delta\lambda = 10$ nm the crosstalk suppression is 17.4 dB.

The measured spectrometers were both designed using design order 9 and design wavelength 730 nm. The characterization, however, was performed using two different input slit widths. The spectrometer fabricated before the optimization was measured using the central input, which is tapered to a width of 11 μm. On the other hand, the spectrometer fabricated after the optimization was measured using an input positioned 400 μm from the position of the central input. This input is only tapered to 30 μm. Thus, part of the observed decrease in transmission loss must be attributed to a decrease in taper loss. The observed decrease in crosstalk suppression is most likely due to the increase in the width of the input slit.

6.3.3 The effect of the process optimization

Figure 6.9 shows a decrease in transmission loss of 9.2 dB. Aside from the effect of the increased lithographic precision of the optimal process, this difference in transmission has contributions from two other sources. Firstly, there is a difference in propagation loss, due to the different processing conditions (cf. section 6.2). Secondly, there is a difference in taper loss, as different input widths were used in the measurements.

The results presented in section 6.2 show an increase in propagation loss after the optimization. From Figure 6.5, the propagation loss at 880 nm is estimated to be 0.35 dB/cm before the process optimization, and 0.60 dB/cm after. This amounts to an increase in propagation loss due to the optimization of $(0.6 \text{ dB/cm} - 0.35 \text{ dB/cm}) \times 2.35 \text{ cm} = 0.6$ dB. The decrease in taper loss between the two measurements is 2.3 dB, as presented in the beginning of

this section. The decrease in transmission loss contributed to the increased lithographic precision of the optimal process is thus $9.2 + 0.6 - 2.3 = 7.5$ dB.

Another interesting question to answer is how much of the 13.1 dB transmission loss measured for the spectrometer fabricated using the optimal process may be attributed to the fabrication process itself. As presented in the beginning of this section, several contributions to the spectrometer transmission loss are already accounted for. The grating loss is 2.5 dB, and the loss penalty due to power distribution among the different diffraction orders is 4.4 dB. The coupling loss is estimated from Figure 6.5 to be 1.5 dB at 890 nm. The propagation loss is 0.6 dB/cm at 880 nm, so the loss due to propagation through the spectrometer is 0.6 dB/cm $\times$ 2.35 cm = 1.4 dB. Expecting the loss penalty for tapering the input waveguide from 40 μm to 30 μm to be negligible, the total transmission loss accounted for is 9.8 dB. The maximum decrease in transmission loss which can be expected from further process optimization is thus 3.3 dB.

6.4 Auto-fluorescence in SU-8

In the spring of 2006, I visited the Division of Solid State Physics at Lund University, in order to investigate the possibility of synthesizing a SERS-active surface inside a micro-fluidic channel. The method used was laser-induced growth of silver particles [44] with HeNe-laser light at 633 nm. The growth is monitored using the enhanced Raman-signal from the reducing reagent. Eventhough the method worked perfectly in a simple glass cell under a microscope, the efforts to replicate the synthesis on-chip were not successful. Two observations were made: Firstly, the growth was much slower in the channel, probably due to the difference in surface chemistry compared to the reference cell. Secondly, and most importantly, no Raman-signal could be detected to confirm successful growth. This was most likely due to heavy background noise caused by SU-8 auto-fluorescence.

In the literature, SU-8 has been observed to fluoresce when exposed to light of wavelengths used to excite fluorescent markers. This is observed for excitation in the Cy3 channel (green light around 550 nm) [29, 30, 31], but also in the Cy5 channel (red light around 650 nm) [29]. In fluorescence detection systems fabricated in SU-8, this auto-fluorescence decreases the signal-to-noise ratio, and thus reduces the sensitivity of the system [30]. At the end of the visit in Lund, the SU-8 auto-fluorescence was measured at several points of excitation in the $458 - 647$ nm wavelength range in order to characterize the phenomenon further. The details of the characterization will be presented at the end of this section.

The result of the characterization of the SU-8 auto-fluorescence is presented in Figure 6.10. Several observations can be made from the data. Firstly, significant fluorescence is generated in the SU-8 by the excitation light, even for excitation at 647 nm. The generated auto-fluorescence reaches well into the near-infrared for all excitation wavelengths used in the investi-

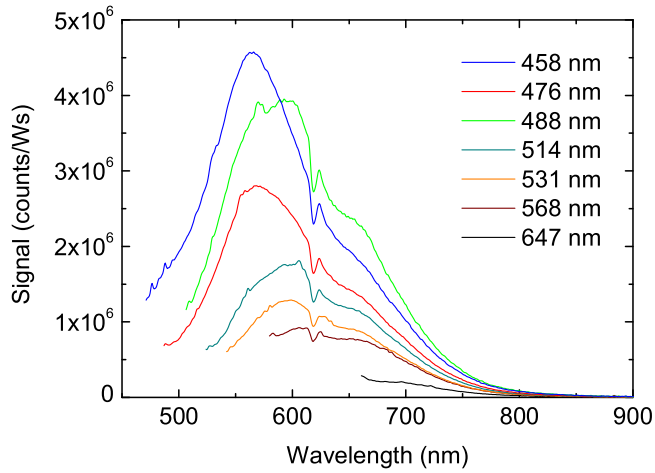

Figure 6.10: Detected SU-8 auto-fluorescence (in counts/Ws) versus wavelength at different excitation wavelengths. The excitation peaks have been removed from each measurement, and the data have been smoothed. These measurements were obtained by exciting the same SU-8 waveguide in order of decreasing excitation wavelength. The feature around 625 nm is an artifact of the detecting spectrometer.

gation. Secondly, the fluorescence signal is observed to increase in intensity with decreasing excitation wavelength. An exception to this trend is seen in the decrease at 476.5 nm excitation when compared to the signal at 488 nm excitation. Since the auto-fluorescence was measured in order of decreasing excitation wavelength on the same SU-8 waveguide, this suggests the fluorescence was bleached at 488 nm. The bleaching is more clear in Figure 6.11, where the fluorescence yield is plotted as a function of excitation wavelength.

It is not within the scope of this dissertation to explain the origin of the SU-8 auto-fluorescence. The conclusion is that a significant auto-fluorescence signal is generated at the excitation wavelength where detection of a Raman signal was attempted. If Raman spectroscopy on a chip is to be realized using the SU-8 based fabrication platform, an excitation wavelength in the near-infrared part of the spectrum, probably above 900 nm, must be used in order for the auto-fluorescent signal to be negligible.

Figure 6.12 shows a sketch of the set-up used to measure the SU-8 auto-fluorescence. The excitation source used was a mixed Krypton-Argon laser. In order to select a particular line, filters placed outside the laser cavity were used. The filters all had 40 dB suppression, and a full width at half maximum (FWHM) of 10 nm except for the filter for the 476.5 nm Ar line which had a FWHM of 20 nm. Before the measurement, the glass lid, which was bonded on top of the structures in the fabrication process, was removed from the

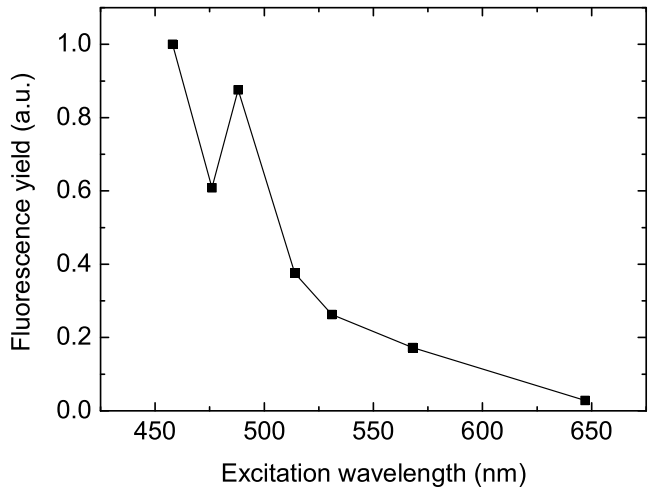

Figure 6.11: Fluorescence yield of SU-8 (relative to the yield at 458 nm excitation) as a function of excitation wavelength, obtained from the same SU-8 waveguide in order of decreasing excitation wavelength. The yield at each excitation wavelength is calculated as the area below the corresponding curve in Figure 6.10. The dip at 476 nm is due to bleaching during the 488 nm measurement.

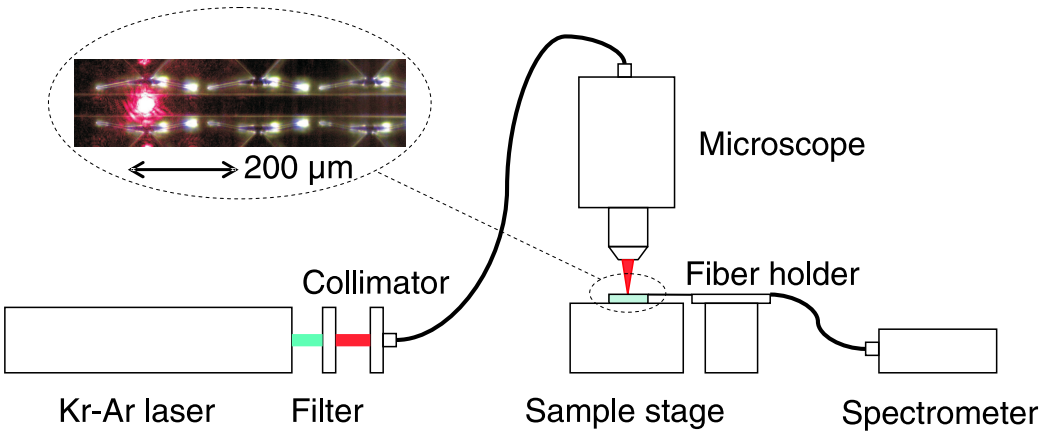

Figure 6.12: A sketch of the set-up used in the measurements of SU-8 autofluorescence. The insert shows a picture of the excitation spot focussed at the top of the waveguide.

sample. The excitation light was focused onto the top of the 40 μm by 40 μm waveguide through a microscope. The focused spot had a diameter of approximately 30 μm. The auto-fluorescence generated in the SU-8 by the excitation light was detected through the output fiber coupled to the waveguide facet approximately 2.5 mm from the excitation spot. Following each measurement, a background signal was established by a measurement with blocked laser, and the excitation power was determined by focusing the microscope on a broadband, thermopile power meter.

The auto-fluorescence of the SU-8 waveguide was characterized at excitation wavelengths of 457.9 nm, 476.5 nm, 488.0 nm, 514.5 nm, 530.9 nm, 568.2 nm, and 647.1 nm. The measurements were carried out on the same waveguide in order of descending excitation wavelength. Due to the varying strength of the different laser lines, the excitation power ranges between 1.35 mW (at 457.9 nm) and 5.60 mW (at 488.0 nm). In order to be able to compare measurements, the raw data are corrected using the spectrometer integration time and the power measured using the power meter. For each measurement, the waveguide was excited for a total of a couple of minutes. Between subsequent measurements the excitation power was measured and the laser filter was changed. The period of no radiation varied between different measurements, ranging from 5 minutes to 23 minutes.

It should be noted that the dip and peak at 620 nm and 625 nm seen in the measurements in Figure 6.10 is an effect of a filter coating in the spectrometer, designed to remove disturbance from second order reflections from the grating [45].

Chapter 7

Summary

A standard SU-8 lithographic process as recommended by the manufacturer [14] does not provide the lithographic precision needed to successfully fabricate an integrated spectrometer based on a concave reflection grating. In order to realize such spectrometers in SU-8, optimization of the lithographic process was performed in two steps. The first step was the development of the edge bead removal. The second step was the optimization of the process parameters.

The developed edge bead removal process reduces the height of the edge bead to below 1 μm. The removal of the edge bead brought about a significant improvement of the resolution of the lithographic process. The aspect ratio of the smallest resolvable trench increased from approximately six to above ten.

The optimization of the process parameters shifted the temperature used in the baking steps in the lithographic process significantly, from the standard 95 °C to a low 65 °C without increasing the baking time accordingly. This optimization further increased the lithographic resolution, increasing the realizable trench aspect ratio to 11.4. The increased resolution is probably caused by an increase in the resist sensitivity, which decreased the optimal exposure dose from 225 mJ/cm^2 to 180 mJ/cm^2. The optimized process completely eliminates cracking of the fabricated structures. This is partly brought on by an increase in the material strength of the cured resist, which also causes the realizable aspect ratio of grating-like ridges to increase from six to almost nine.

The improved resolution resulting from the process optimization has decreased the transmission loss of integrated spectrometers fabricated in SU-8 by an estimated 7.5 dB. This corresponds to a sixfold increase in the spectrometer throughput. The spectrometer loss is 13.1 dB, corresponding to approximately one in every 20 photons being transmitted through the spectrometer. The decrease in transmission loss means that the contribution to the spectrometer loss that can be attributed to the fabrication process is down to 3.3 dB. Thus, the spectrometer loss can only be improved by a factor of two by further optimization of the fabrication process. One drawback

of the optimization is increased propagation loss through waveguides fabricated using the optimized processing parameters. If resolution and cracking is considered second to propagation loss, standard processing should thus be used.

The success of the process optimization is evaluated on the basis of the goals defined in section 1.3:

- *Inter-structural resolution down to 4 μm.*
  At 1:1 pattern transfer the inter-structural resolution is 3.4 μm, corresponding to an aspect ratio of 11.4. The sidewall angle is 0.5°. The best resolution observed is 2.8 μm, corresponding to an aspect ratio above 14.

- *Stable structures with aspect ratios exceeding 7.*
  Grating-like ridges are stable to an aspect ratio of 8.8.

- *Reproducible, uniform SU-8 layer thickness. Standard deviation of the layer thickness in the quality area below 0.7 %. Edge bead below 10 % of the thickness, if possible down to 2 %.*
  The surface roughness of the SU-8 layer after coating and edge bead removal is 0.4 μm, corresponding to 1 % of the layer thickness. The standard deviation of the layer thickness measured at eight points across the quality area after development is slightly higher, typically around 2 %. At 0.64 μm the height of the edge bead corresponds to 1.7 % of the layer thickness.

- *A yield of 95 % (including packaging and dicing).*
  The fabrication yield of 128 chips with integrated optical and fluidic system was 90 %, including a simple leakage test of the fluidic system.

- *Spectrometer loss in the* $785 - 885$ *nm band of no more than 15 dB, preferably lower, with a channel-to-channel variation below 1 dB.*
  The spectrometer with the best transmission has a loss of 13.1 dB at 890 nm, with a variation of 0.7 dB over the whole $785 - 890$ nm band.

- *Crosstalk suppression at* $\Delta\lambda = 10$ *nm in the* $785 - 885$ *nm band of at least 20 dB.*
  The crosstalk suppression for the spectrometer with the best transmission is 17.4 dB. The signal-to-noise ratio, however, is 25 dB.

The results fall short on three accounts; SU-8 layer thickness variation, fabrication yield, and crosstalk suppression. The elevated layer thickness variation is most likely caused by the so-called EBR-spatter from the edge bead removal process. This effect produces local disturbances in the SU-8 coating, which effects the bonding procedure. The degraded fabrication yield is thus attributed to the same effect. The crosstalk suppression is related to the spectrometer design. A higher crosstalk suppression may be achieved by decreasing the width of the input slit, but this would also introduce a loss penalty.

7.1 Conclusion

As presented above, the optimization of the SU-8 fabrication process has been very successful, both in terms of the lithographic performance and the performance of the fabricated spectrometers. An important question to ask is whether the effort of design of experiments was worth the while, or whether the same success could have been accomplished using intuition and a bit of trial and error? In my view, two things would have been different without design of experiments. Firstly, the optimization would not have reached the result of low baking temperature, as the soft bake would probably have been disregarded, or investigated in a much narrower range around the starting point. Secondly, as a consequence the one-factor-at-a-time nature of such investigations, our knowledge of the process would have been much more limited.

The results of the optimization have also proved to be of interest to other researchers. An article covering the investigation of the soft bake temperature presented in section 4.6 was published in Journal of Micromechanics and Microengineering in August 2006. This article was among the top ten most downloaded articles across all Institute of Physics Publishing journals in the third quarter of 2006. I have had several enquiries regarding this article, both from researchers at MIC and from international researchers.

7.2 Outlook

The analysis of the spectrometer transmission loss in section 6.3 reveals that the largest contributions to the loss is due to the distribution of the input power among several diffraction orders. The next step in the development of the spectrometer would thus be to incorporate blazing in the grating design. Up to 4.4 dB may be gained from a blazed grating design.

In terms of the relevance of the spectrometers in lab-on-a-chip systems, the next step would be a proof of the concept of on-chip detection and analysis using the integrated spectrometer. This could be accomplished by connecting the separate devices in the laboratory, but the proof would be more convincing if the individual parts were integrated in the same device. Such an integrated detection system has already been designed. The system consists of a fluidic system for sample introduction, waveguides for transport of the excitation light, detection of the signal, and transport of the detected signal, and a spectrometer for analysis of the detected signal, as seen in Figure 7.1.

The system in Figure 7.1 has micro cuvettes for detection based on absorbance, but the design also includes fluorescent detection. The actual detection of the analyzed signal is accomplished by projecting the output plane of the spectrometer onto a linear CCD array. The sensitivity and limit of detection of the system could be measured using standard fluorescent markers, dyes, or quantum dots. The fabrication of the designed system is all but finished, but the performance is yet to be characterized.

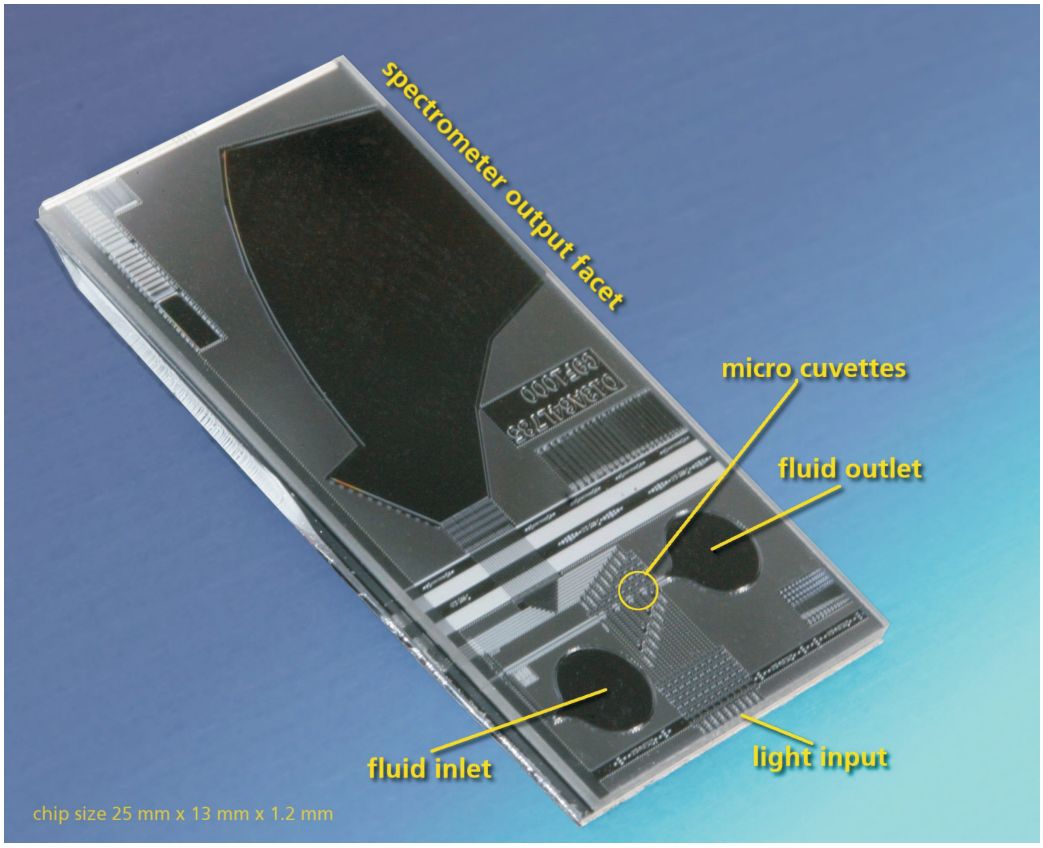

Figure 7.1: Picture of a system designed for on-chip detection and analysis.

Appendix A

List of Publications

A.1 Peer-reviewed Journal Papers

- Dan A Zauner, Anders M Jorgensen, Thomas A Anhoj and Jörg Hübner. High-density multimode integrated polymer optics. *Journal of Optics A: Pure and Applied Optics*, 7: 445-450, 2005.

- Dan A. Zauner, Anders M. Jorgensen, Thomas A. Anhoj and Jörg Hübner. Concave reflective SU-8 photoresist gratings for flat-field integrated spectrometers. *Applied Optics*, 45: 5877-5880, 2006.

- Thomas A Anhoj, Anders M Jorgensen, Dan A Zauner and Jörg Hübner. The effect of soft bake temperature on the polymerization of SU-8 photoresist. *Journal of Micromechanics and Microengineering*, 16: 1819-1824, 2006.

A.2 Conference Proceedings

- Jörg Hübner, Dan Zauner, Thomas A. Anhøj, Anders M. Jorgensen. Multimode Integrated Optical Components for μTAS -A Rigorous Approach. *Proceedings of μTAS 2004*, Vol. I: 357-359, 2004.

- Jorg Hubner, Anders M. Jorgensen, Thomas A. Anhoj, and Dan A. Zauner. Integrated optical systems for lab-on-a-chip applications. *Proceedings of SPIE*, 5728: 269-277, 2005.

- Thomas A. Anhoj, Anders M. Jorgensen, Dan A. Zauner, Jörg Hübner. Optimization of SU-8 processing for integrated optics. *Proceedings of SPIE*, 6110: 611009, 2006.

- Anders M. Jorgensen, Dan A. Zauner, Thomas A. Anhoj, Peter M. Moselund, Jörg Hübner. On-chip integrated spectrometer and microfluidic fluorescence set-up. *Proceedings of SPIE*, 6112: 611209, 2006.

A.3 Patents

- Jörg Hübner, Anders M. Jørgensen, Thomas A. Anhøj, Dan A. Zauner. *On chip spectrometer*. PCT Dk/2005/000494.

Bibliography

[1] A. Manz, N. Graber, and H.M. Widmer. Miniaturized total chemical analysis systems: a novel concept for chemical sensing. *Sensors and Actuators B (Chemical)*, B1(1-6):244–8, 1990.

[2] Alan Campion and Patanjali Kambhampati. Surface-enhanced raman scattering. *Chemical Society Reviews*, 27(4):241–250, 1998.

[3] Mesophotonics Ltd, Southampton, United Kingdom (www.mesophotonics.com/products/klarite.html).

[4] Klaus B. Mogensen, Jamil El-Ali, Anders Wolff, and Jorg P. Kutter. Integration of polymer waveguides for optical detection in microfabricated chemical analysis systems. *Applied Optics*, 42(19):4072–4079, 2003.

[5] S. Balslev, A. M. Jorgensen, B. Bilenberg, K. B. Mogensen, D. Snakenborg, O. Geschke, J. P. Kutter, and A. Kristensen. Lab-on-a-chip with integrated optical transducers. *Lab on a Chip*, 6(2):213–217, 2006.

[6] B. Bilenberg, T. Nielsen, B. Clausen, and A. Kristensen. Pmma to su-8 bonding for polymer based lab-on-a-chip systems with integrated optics. *Journal of Micromechanics and Microengineering*, 14(6):814–818, 2004.

[7] Jorg Hubner, Anders M. Jorgensen, Thomas A. Anhoj, and Dan A. Zauner. Integrated optical systems for lab-on-chip applications. *Integrated Optics: Devices, Materials, and Technologies IX and Progress in Biomedical Optics and Imaging - Proceedings of SPIE*, 5728:269–277, 2005.

[8] K.A. McGreer. Theory of concave gratings based on a recursive definition of facet positions. *Applied Optics*, 35(30):5904–5910, 1996.

[9] Dan A. Zauner, Anders M. Jorgensen, Thomas A. Anhoj, and Jorg Hubner. Concave reflective su-8 photoresist gratings for flat-field integrated spectrometers. *Applied Optics*, 45(23):5877–5880, 2006.

[10] Nancy C. LaBianca and Jeffrey D. Gelorme. High-aspect-ratio resist for thick-film applications. *Proceedings of SPIE - The International Society for Optical Engineering*, 2438:846–852, 1995.

[11] J. V. Crivello and J. H. W. Lam. Photoinitiated cationic polymerization with triarylsulfonium salts. *J Polym Sci Polym Chem Ed*, 17(4):977–999, 1979.

[12] J.M. Shaw, J.D. Gelorme, N.C. Labianca, W.E. Conley, and S.J. Holmes. Negative photoresists for optical lithography. *IBM Journal of Research and Development*, 41(1-2):81–94, 1997.

[13] K.Y. Lee, N. LaBianca, S.A. Rishton, S. Zolgharnain, J.D. Gelorme, J. Shaw, and T.H.-P. Chang. Micromachining applications of a high resolution ultrathick photoresist. *Journal of Vacuum Science & Technology B: Microelectronics Processing and Phenomena*, 13(6):3012–3016, 1995.

[14] MicroChem Corp. NANO^{TM} SU-8 Negative Tone Photoresist Formulations 2-25, Datasheet (www.microchem.com), Rev. 2/02.

[15] S. C. Jakeway, A. J. de Mello, and E. L. Russell. Miniaturized total analysis systems for biological analysis. *Fresenius' Journal of Analytical Chemistry*, 366(6-7):525–539, 2000.

[16] M.B. Chan-Park, J. Zhang, Y. Yan, and C.Y. Yue. Fabrication of large su-8 mold with high aspect ratio microchannels by uv exposure dose reduction. *Sensors and Actuators B: Chemical*, 101(1-2):175–182, 2004.

[17] H. Lorenz, M. Despont, N. Fahrni, J. Brugger, P. Vettiger, and P. Renaud. High-aspect-ratio, ultrathick, negative-tone near-uv photoresist and its applications for mems. *Sensors and Actuators A (Physical)*, A64(1):33–9, 1998.

[18] Zhong-geng Ling, Kun Lian, and Linke Jian. Improved patterning quality of su-8 microstructures by optimizing the exposure parameters. *Proceedings of SPIE - The International Society for Optical Engineering*, 3999 (II):1019–1027, 2000.

[19] John D. Williams and Wanjun Wang. Study on the postbaking process and the effects on uv lithography of high aspect ratio su-8 microstructures. *Journal of Microlithography, Microfabrication and Microsystems*, 3(4):563–568, 2004.

[20] Mirwais Aktary, Martin O. Jensen, Kenneth L. Westra, Michael J. Brett, and Mark R. Freeman. High-resolution pattern generation using the epoxy novolak su-8 2000 resist by electron beam lithography. *Journal of Vacuum Science and Technology B: Microelectronics and Nanometer Structures*, 21(4):L5–L7, 2003.

[21] Saulius Juodkazis, Vygantas Mizeikis, Kock Khuen Seet, Masafumi Miwa, and Hiroaki Misawa. Two-photon lithography of nanorods in su-8 photoresist. *Nanotechnology*, 16(6):846–849, 2005.

[22] B. Eyre, J. Blosiu, and D. Wiberg. Taguchi optimization for the processing of epon su-8 resist. *Micro Electro Mechanical Systems, 1998. MEMS 98. Proceedings., The Eleventh Annual International Workshop on*, pages 218–222, 1998.

[23] Deng-Huei Hwang, Yi-Chung Lo, and Kanping Chin. Development of a systematic recipe set for processing su8-5 photoresist. *Proceedings of SPIE - The International Society for Optical Engineering*, 4592:131–139, 2001.

[24] J. Zhang, K.L. Tan, G.D. Hong, L.J. Yang, and H.Q. Gong. Polymerization optimization of su-8 photoresist and its applications in microfluidic systems and mems. *Journal of Micromechanics and Microengineering*, 11(1):20–26, 2001.

[25] J. Liu, B. Cai, J. Zhu, G. Ding, X. Zhao, C. Yang, and D. Chen. Process research of high aspect ratio microstructure using su-8 resist. *Microsystem Technologies*, 10(4):265–268, 2004.

[26] Sang Jeen Hong, Seungkeun Choi, YoonSu Choi, M. Allen, and G.S. May. Characterization of low-temperature su-8 photoresist processing for mems applications. *Advanced Semiconductor Manufacturing, 2004. ASMC '04. IEEE Conference and Workshop*, pages 404–408, 2004.

[27] Che-Hsin Lin, Gwo-Bin Lee, Bao-Wen Chang, and Guan-Liang Chang. A new fabrication process for ultra-thick microfluidic microstructures utilizing su-8 photoresist. *Journal of Micromechanics and Microengineering*, 12(5):590–597, 2002.

[28] The refractive index data were supplied by MicroChem Corp., Newton, Massachusetts, USA (www.microchem.com).

[29] M. Nordstrom, M. Calleja, and A. Boisen. Polymeric micro-channel-based functionalisation system for micro-cantilevers. *Ultramicroscopy*, 105(1-4):281–286, 2005.

[30] Shih-Hao Huang and Fan-Gang Tseng. Development of a monolithic total internal reflection-based biochip utilizing a microprism array for fluorescence sensing. *Journal of Micromechanics and Microengineering*, 15(12):2235–2242, 2005.

[31] R. Marie, S. Schmid, A. Johansson, L. Ejsing, M. Nordstrom, D. Hafliger, C.B. Christensen, A. Boisen, and M. Dufva. Immobilisation of dna to polymerised su-8 photoresist. *Biosensors and Bioelectronics*, 21(7):1327–1332, 2006.

[32] M. Shaw, D. Nawrocki, R. Hurditch, and D. Johnson. Improving the process capability of su-8. *Microsystem Technologies*, 10(1):1–6, 2003.

[33] Marc Madou. *Fundamentals of microfabrication.* CRC Press LLC, 1997.

[34] Private conversation with Associate Professor Ole Hansen (MIC - Department of Micro and Nanotechnology, Technical University of Denmark). The subject is also treated in [33] and [46].

[35] Toshihiko Tanaka, Mitsuaki Morigami, and Nobufumi Atoda. Mechanism of resist pattern collapse during development process. *Japanese Journal of Applied Physics, Part 1: Regular Papers &; Short Notes &; Review Papers*, 32(12):6059–6064, 1993.

[36] L.J. Guerin, M. Bossel, M. Demierre, S. Calmes, and P. Renaud. Simple and low cost fabrication of embedded micro-channels by using a new thick-film photoplastic. *Solid State Sensors and Actuators, 1997. TRANSDUCERS '97 Chicago., 1997 International Conference on*, 2:1419–1422 vol.2, 1997.

[37] Veronica Czitrom. Teacher's corner - one-factor-at-a-time versus designed experiments. *American Statistician*, 53(2):126–131, 1999.

[38] Douglas C. Montgomery. *Design and Analysis of Experiments.* John Wiley & Sons, Inc., fifth edition, 2001.

[39] Umetrics AB, Umeå, Sweden (www.umetrics.com).

[40] Alexei L. Bogdanov. Use of su-8 negative photoresist for optical mask manufacturing. *Proceedings of SPIE - The International Society for Optical Engineering*, 3999 (II):1215–1225, 2000 (Also available online at www.maxlab.lu.se/beamlines/bld811).

[41] James V. Crivello. Discovery and development of onium salt cationic photoinitiators. *Journal of Polymer Science, Part A: Polymer Chemistry*, 37(23):4241–4254, 1999.

[42] Upchurch Scientific, Inc., Oak Harbor, Washington, USA (www.upchurch.com).

[43] F. Ladouceur. Roughness, inhomogeneity, and integrated optics. *Journal of Lightwave Technology*, 15(6):1020–1025, 1997.

[44] Erik J Bjerneld, K V G K Murty, Juris Prikulis, and Mikael Kall. Laser-induced growth of ag nanoparticles from aqueous solutions. *ChemPhysChem*, 3(1):116–118, 2002.

[45] Avantes BV, Eerbeek, The Netherlands (www.avantes.com).

[46] James D. Plummer, Michael D. Deal, and Peter B Griffin. *Silicon VLSI technology.* Prentice Hall, Inc., 2000.